PROSPECTIVE AND DEEP LEARNING BASED RETROSPECTIVE MOTION CORRECTION FOR BRAIN MAGNETIC RESONANCE IMAGING

Thesis

for the degree of

doctor rerum naturalium (Dr. rer. nat.)

approved by the Faculty of Natural Sciences of
Otto von Guericke University Magdeburg

by M.Sc. Alessandro Sciarra

born on April 24, 1982, in Guardiagrele (Italy)

Examiners: Prof. Dr. rer. nat. habil. Oliver Speck,
Prof. Dr. rer. nat. habil. Maxim Zaitsev

submitted on: April 30, 2024
defended on: December 16, 2024

ABSTRACT

Magnetic Resonance Imaging (MRI) is one of the most important medical imaging technique used every day world wide for clinical and research purposes, (1).

It's a non-invasive method and uses non ionising radiation. Compared with other imaging techniques, such as Computed Tomography, MRI requires a longer acquisition time. The long acquisition times can lead to have images degraded in term of quality, because, subjects tend to move. The motion during the scan is the cause of blurring and ghosting in the MR images. To avoid or to limit the presence of motion artefacts (blurring or ghosting), there are available several approaches, such as Prospective Motion Correction (PMC), (2), Retrospective Motion Correction (RMC) methods, etc..

The first part of this thesis work is aimed at assessing the impact of the prospective motion correction using an in-bore optical tracking system, in case of high-resolution structural imaging in regime of quasi-no motion. All the work was carried out at ultra high field MRI, 7T. The structural imaging is only about ultra high resolution imaging using several types of image weighting, specifically: T_1, T_2, T_2^* and PD, (sections 1 and 4).

Considering the tremendous amount of attention received by machine and deep learning over the last few years when applied to medical imaging, in this thesis work it is also presented a second part where several preliminary deep learning retrospective based motion artefacts detection and correction approaches were tested, once more only for structural brain imaging. There are two sections, one dedicated to the Image Quality Assessment (IQA) based on the Structural Similarity Index Measure (SSIM) prediction through a deployment of a neural network and one last section containing the application of several neural networks (i.e. Residual Network (ResNet) and U-Network (U-Net)) for the retrospective correction of motion artefacts.

ZUSAMMENFASSUNG

Die MRT ist eine der wichtigsten medizinischen Bildgebungsmethoden, die täglich weltweit weltweit zu klinischen und Forschungszwecken eingesetzt wird (1). Es handelt sich um eine nicht-invasive Methode, bei der keine ionisierende Strahlung verwendet wird. Verglichen mit anderen bildgebenden Verfahren, wie z. B. der Computertomografie, benötigt die MRT eine längere Aufnahmezeit. Die langen Aufnahmezeiten können zu einer Verschlechterung der Bildqualität führen Qualität der Bilder führen, da sich die Probanden oft bewegen. Die Bewegung während des Scans ist die Ursache für Unschärfe und Geisterbilder in den MR-Bildern. Um das Vorhandensein von Bewegungsartefakten zu vermeiden oder zu begrenzen Bewegungsartefakte (Unschärfe oder Geisterbilder) zu vermeiden oder zu begrenzen, gibt es verschiedene Ansätze, wie PMC, (2), RMC-Methoden, etc. Der erste Teil dieser Arbeit zielt darauf ab, die Auswirkung der prospektiven Bewegungskorrektur mit Hilfe eines optischen Verfolgungssystems in der Bohrung bei hochauflösender struktureller Bildgebung in einem Zustand, in dem quasi keine Bewegung stattfindet, zu bewerten. Die gesamte Arbeit wurde am Ultrahochfeld-MRT (7T) durchgeführt. Bei der strukturellen Bildgebung geht es ausschließlich um die ultrahochauflösende Bildgebung unter Verwendung verschiedener Arten der Bildgewichtung, insbesondere: T1, T2, T*2 und PD, (Abschnitte 1 und 4).

In Anbetracht der enormen Aufmerksamkeit, die maschinelles Lernen und Deep Learning in den letzten Jahren bei der Anwendung auf die medizinische Bildgebung erhalten hat, wird in dieser Arbeit auch ein zweiter Teil vorgestellt, in dem mehrere vorläufige, auf tDeep Learning basierende retrospektive Ansätze zur Erkennung und Korrektur von Bewegungsartefakten getestet wurden, wiederum nur für strukturelle Aufnahmen des Gehirns. Dieser Teil gliedert sich in zwei Abschnitte: Einerseits der automatischen Quantifizierung der Bildqualität durch ein Convolutional Neural Network auf Basis der Schätzung von Structural Similarity (SSIM) Indices und andererseits der Anwendung von neuralen Netzen wie Redidual Networks und U-Nets für die retrospektive Korrektur von Bewegungsartefakten.

CONTENTS

LIST OF FIGURES

LIST OF TABLES

LISTINGS

ACRONYMS

MRI Magnetic Resonance Imaging

NMR Nuclear Magnetic Resonance

PMC Prospective Motion Correction

RMC Retrospective Motion Correction

FT Fourier Transform

ROI Region-Of-Interest

IQA Image Quality Assessment

SSIM Structural Similarity Index Measure

ResNet Residual Network

ReconResNet Reconstruction Residual Network

U-Net U-Network

DL-RMC Deep Learning based RMC

OMTS Optical Motion Tracking System

MPT Moiré Phase Tracking

fMRI functional MRI

EPI Echo Planar Imaging

DWI Diffusion Weighted Imaging

RF Radio Frequency

FA Flip-angle

FID Free Induction Decay

TR Repetition Time

TE Echo Time

TI Inversion Time

FT Fourier Transform

SNR Signal-to-Noise Ratio

FoV Field of View

TSE Turbo Spin Echo

GE Gradient Echo

SE Spin Echo

FLASH Fast Low Angle Shot

MP-RAGE Magnetization Prepared Rapid Acquisition by Gradient Echo

TA Acquisition Time

ETL Echo Train Length

G_{SS} Slice Selection gradient

G_{FE} Frequency Encoding gradient

G_{PE} Phase Encoding gradient

GM Grey Matter

WM White Matter

CSF Cerebrospinal fluid

CNN Convolutional Neural Network

DNN Deep Neural Network

LSTM Long Short-Term Memory

FCN Fully Convolutional Network

GAN Generative Adversarial Network

AES Average Edge Strength

SD Standard Deviation

MSE Mean Squared Error

CNR Contrast-to-Noise Ratio

CJV Coefficient of Joint Variation

EFC Entropy Focus Criterion

QI Quality Index

SIQA Subjective Image Quality Assessment

MLP Multilayer Perceptron

PACE Prospective Acquisition CorrEction

SVR Slice-to-Volume Registration

IRS Iterative Reconstruction with Self-consistent phase correction

AI Artificial Intelligence

Part I

INTRODUCTION TO MRI

1 MAGNETIC RESONANCE IMAGING

1.1 INTRODUCTION

MRI is one of the most widely used clinical imaging techniques to obtain radiological images. MRI allows the users to have multi-contrast, qualitative, quantitative (relaxometry, spectroscopy, diffusion, etc.) and functional images.

Magnetic refers to the magnetic properties of the matter that makes up the human body. All matter exhibits magnetic properties when placed in an external magnetic field, and depending on the behaviour, the matter can be classified as paramagnetic (e.g. air or aluminium), diamagnetic (e.g. water) or ferromagnetic (e.g. iron, it has a strong attraction towards the static magnetic field). In the case of MRI, even if the human body contains iron atoms (iron in our blood is not ferromagnetic), the major part of it is diamagnetic (water molecules), and it is possible to observe paramagnetic properties, e.g. in the deoxygenated blood. Observing or measuring the variations of magnetic properties of tissues leads to having images and information regarding the structure and how, e.g., the brain or other organs are connected and work.

Resonance is the phenomenon that occurs when an object free to vibrate or to rotate at one specific natural frequency will vibrate or rotate strongly when it is stimulated by impulses with the same frequency or nearly close to its natural frequency. This phenomenon is the basis of the MRI.

Imaging is the simple process of creating visual representations of an object. Considering the term medical imaging refers to several techniques to obtain images of the interior of the body.

1.2 A BIT OF HISTORY

Nuclear Magnetic Resonance (*NMR*) has been discovered by Rabi [1], in 1937. For his studies, Rabi received the Nobel Prize in Physics in 1944. The experiments conducted by Rabi and his team has proven that it is possible to flip the principal magnetic orientation of nuclei by an oscillating magnetic field [2].
Following the discovery of the NMR phenomenon, there has been a continuous evolution up to the present day. The timeline of MRI can be divided into three parts: the discovery of the NMR phenomenon (non-imaging), initial applications of MRI in medical imaging (diagnostic, anatomic imaging) and the emergence of functional MRI (fMRI) and more advanced imaging techniques.

In 1946 Bloch et al. [3] published the first results on the phenomenon of nuclear induction, they carefully described the working principle and the details of their experimental setup. Another fundamental contribution arrived two years later, in 1948, "*Relaxation Effects in Nuclear Magnetic Resonance Absorption*" by Bloembergen et al. [4]. In practice, when an object is placed in a static magnetic field with a defined direction, e.g. z, the nuclear magnetic moments tend to orient themselves parallel to that field; this condition is called "*thermal equilibrium*". If an oscillating magnetic field is superimposed in the x direction, the thermal equilibrium is disrupted, and the polarisation vector deviates from the z direction. The deviation from the thermal equilibrium state can be described by the macroscopic polarisation vector $\mathbf{M}$. When the oscillating magnetic field is turned off, the system returns to the thermal equilibrium state, and this process involves the generation of measurable electromagnetic signals, the so-called nuclear magnetic resonance (NMR) signal. The NMR signal is the measure of the above-mentioned deviation.

After the works of Bloch et al., nuclear magnetic resonance started to revolutionise the field of chemistry, biochemistry, biology and not so late, also the field of medicine, in particular medical imaging. In fact, in 1973, Peter Laterbeur (Nobel Prize in Medicine/Physiology, 2003) obtained the first true 2D NMR image, [5, 6]. Following Lauterbur's work, a series of important goals have been achieved. In 1975/1976, Richard Ernst et al.[7, 8] with two important works, introduced the new technique of forming two- or three-dimensional images of a macroscopic sample. Based on the application of phase and frequency encoding, followed by a straightforward Fourier transform.

The following are some of the important contributions that have marked the continuing development of MRI:

- 1974/1977 - Raymond Damadian assisted by his post-doctoral students [9, 10] developed the first MRI scanner and successfully detected a tumour in a living animal.
- 1974/1982 - Peter Mansfield, also Nobel Prize in Medicine/Physiology, 2003 (together with Peter Laterbeur), has contributed several fundamental works. He improved the mathematical framework behind MRI and developed the basic technique for fast MR imaging, Echo Planar Imaging (EPI), [11–14].
- 1979/1983 - In 1979 Likes [15] and later in 1983 Twieg and Ljunggren [16, 17], introduced the formalism of *k-space*. Technically, the *k-space* is the Fourier transform (2D or 3D) of the MR image acquired.
- 1986 - Le Bihan [18] published one of the first work on Diffusion Weighted Imaging (DWI). An MR method to image the "*intravoxel incoherent motions*" using appropriate gradient pulses.
- 1987 - Chapman et al. [19] obtained real-time movie imaging from a single cardiac cycle using an MRI system.
- 1990's - MRI started being used in large and small hospitals for neuro and musculoskeletal imaging applications.

- 1991/1993 The scientific community started to face the problem of **motion artefacts** in MR imaging [20–25]. Unfortunately, the acquisition time in MRI is usually longer than a few minutes and not so fast if compared, for instance, to CT (Computed-Tomography). During the examination, the patient can move, and this motion leads to ghost artefacts in the image, which can interfere with the diagnosis. After these first works, researchers kept working on how to limit or solve this problem.

- 1993 - Making use of fast imaging techniques, fMRI of the brain is introduced. Small changes in signal intensity correlate with the brain activities, more in detail, it is associated with blood-oxygenation variations, [26, 27].

- 2000/Today - MRI is a standard medical imaging technique. It's used daily for cardiac MRI, body MRI, fetal imaging and brain imaging. Many research centres have further developed the capabilities of MR systems. Significant achievements have been obtained in terms of hardware and software, and more compact and efficient scanners are available. Every day, these machines are able to provide images characterised by high image quality within a reasonable acquisition time.

1.3 PHYSICS OF MRI

The most abundant element in the human body is hydrogen [28]. The nucleus of the hydrogen atom (one proton) is characterised by having a spin angular momentum, $\mathbf{I} = \frac{1}{2}\hbar$, where $\hbar$ is the reduced Planck's constant $\frac{h}{2\pi}$ [29]. The magnetic moment associated is $\mu_p = 2.792847\mu_N$, with μ_N nuclear magneton. Spin in quantum mechanics refers to an intrinsic property of elementary particles and atomic nuclei, and it's associated with angular momentum. Given a nucleus, there will be a net spin, which depends on its mass number Z, number of nucleons, atomic number A, number of protons and N, neutron number. A nucleus presents a **half-integer** spin when Z is odd and **integer** when Z is even and A is odd. If Z and A are, even the net spin is **zero**. Considering a particle with mass m and electrical charge q, the associated magnetic dipole moment $\boldsymbol{\mu}$ is equal to (Figure 1):

$$\boldsymbol{\mu} = \gamma \mathbf{I}, \ \ where \ \ \gamma = g\frac{q}{2m} \tag{1}$$

γ is the gyromagnetic ratio. The g factor is dimensionless, and its value for protons is $g_p \approx 5.5857$, instead for electrons $g_e \approx 2.0023$. The magnetic dipole moment is characterised to be a quantised variable. Through the magnetic number m_l, μ value is:

$$\mu = \gamma \hbar m_l, \ \ with \ \ m_l = \{-I, -I+1, ..., I\} \tag{2}$$

The term m_l indicates the magnetic quantum number [30].

Classically, the proton can be considered a tiny magnetic bar, a magnetic dipole, and also as a gyroscope, since it has a positive electrical charge ($e = 1.60217\,\mathrm{C}$), see Figure 2. Macroscopically, the spin manifestation is called magnetisation $\mathbf{M}$,

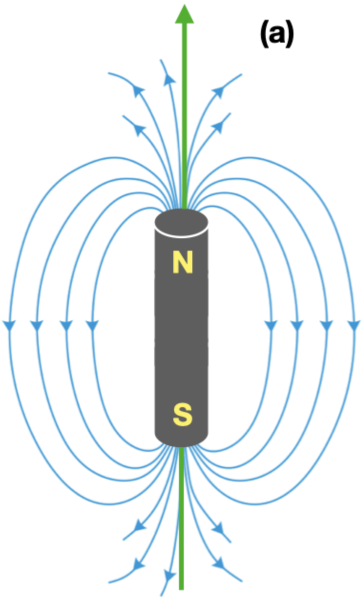

Figure 1: (a): Magnetic dipole with lines of force from the north to the south pole of a bar magnet; (b) classical representation of a proton as a solid sphere charge spinning about an internal axis.

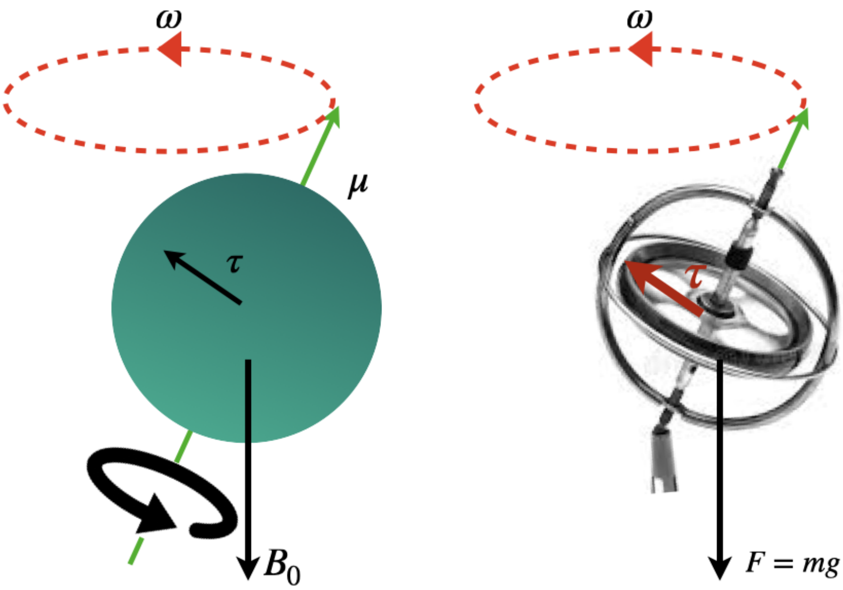

Figure 2: Left: classical magnetic dipole precessing with angular momentum ω around the direction of the static field B_0. Right: Similar to the dipole, a gyroscope spins around its own axis under the force of the earth's gravitational field. There is always a torque τ perpendicular to the internal axis of rotation.

that is, the vector sum of each magnetic dipole moment of the nuclear spins in the volume of interest.

Precession: when a magnetic dipole, μ, is placed in a static magnetic field $\mathbf{B}_0$, it experiences a torque equal to: $\mu \times \mathbf{B}_0$, and if the field is heterogeneous a force equal to: $\mu \cdot \nabla B_0$. Consequently, the magnetic dipole will have a potential energy that can be expressed as $-\mu \cdot \mathbf{B}_0$. This potential energy is minimal when μ and $\mathbf{B}_0$ are parallel. An ensemble of (N) proton spins placed in a static uniform magnetic field quickly reach the thermal equilibrium, Figure 3. Assuming a two-state problem,

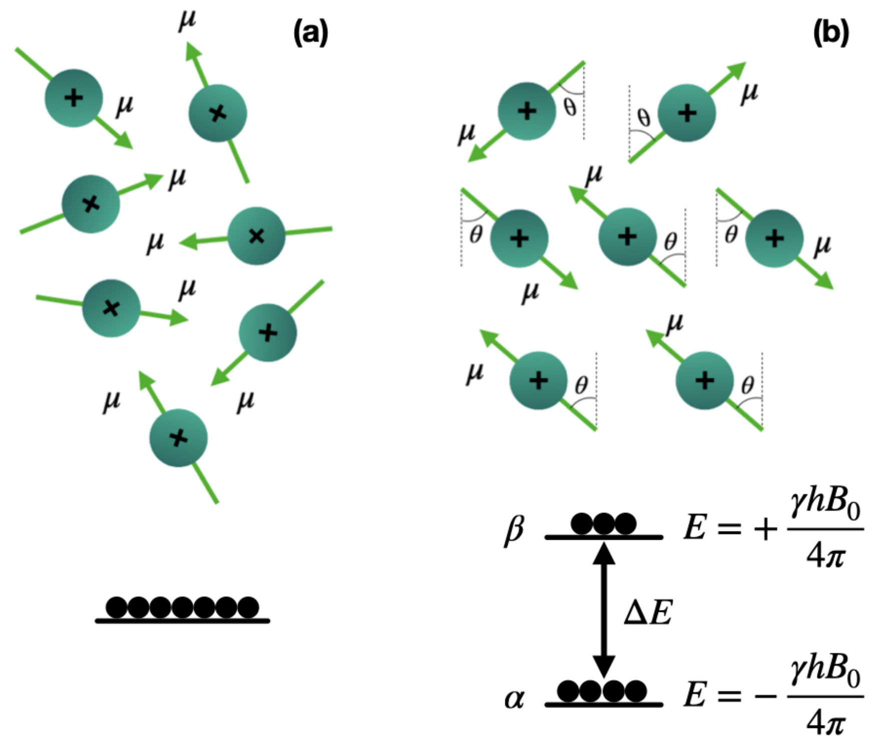

Figure 3: (a) An ensemble of spins with no external static magnetic field, $\mathbf{M} = 0$; (b) when an external static magnetic field $\mathbf{B}_0$ is applied $\mathbf{M} \neq 0$, a greater number of nuclei occupy the lower energy, parallel state.

orientation parallel (↑, with energy $-\mu B$) or anti-parallel (↓, with energy $+\mu B$) to the magnetic field, the distribution for a sample of N protons is:

$$N_\uparrow / N_\downarrow = e^{2\mu B/k_B T} \approx 1 + \frac{2\mu B_0}{k_B T}, \qquad N_\uparrow - N_\downarrow = \frac{2\mu B_0}{k_B T} N_\downarrow \approx \frac{\mu B_0}{kT} N \tag{3}$$

k_B is the Boltzmann constant $(1.380649\text{x}10^{-23} m^2 kg s^{-2} K^{-1})$ and T the temperature of the system considered. The net magnetization is equal to $\mathbf{M} = \mu(N_\uparrow - N_\downarrow)$ p.p.m. at room temperature. Although this is a really small quantity, considering the large number of protons in a tissue sample, it is possible to detect it, if $\mathbf{B}$ is large. Perturbating the net magnetization $\mathbf{M}$, the perpendicular component $\mathbf{M}_\perp$ will precess around $\mathbf{B}_0$ producing a detectable signal. The precession equation is as follows:

$$\frac{d\mathbf{M}}{dt} = \gamma_p \mathbf{M} \times B_0 \tag{4}$$

Category	Subcategory	Frequency (MHz)	Field strength (T)	Wavelength (m)
radio waves	LF (long wave)	$0.03 - 0.3$	$7x10^{-4} - 7x10^{-3}$	$10^4 - 10^3$
	MF (medium wave)	$0.3 - 3$	$7x10^{-3} - 0.07$	$10^3 - 10^2$
	AM radio (MF)	$0.54 - 1.6$	$0.013 - 0.038$	$555 - 188$
	HF (short wave)	$3 - 30$	$0.07 - 0.7$	$10^2 - 10$
	VHF (short wave)	$30 - 300$	$0.7 - 7$	$10 - 1$
	FM radio (VHF)	$54 - 216$	$1.27 - 5.07$	$5.55 - 1.39$
	UHF	$300 - 3x10^3$	$7 - 70$	$1 - 0.1$
	SHF	$3x10^3 - 3x10^4$	$70 - 700$	$0.1 - 0.01$
microwaves		$10^4 - 3x10^5$	$233 - 7x10^3$	$0.3 - 10^{-3}$

Table 1: Frequencies, wavelenghts and magnetic field strengths [32].

Further considerations can be made regarding an ensemble of spins placed in a static magnetic field. First of all, if the temperature of the system is high enough, it is possible to apply the Boltzmann distribution and obtain the angular distribution, P, from the following equation:

$$P = \frac{1}{Z} e^{-\frac{E(\theta)}{k_B T}} \tag{5}$$

where θ is the angle between the dipole and the magnetic field (see Figure 3) and Z the canonical partition function [31], defined as:

$$Z = \sum e^{-\frac{E(\theta)}{k_B T}} = 2\pi R \int_0^{\pi} e^{-\frac{E(\theta)}{k_B T}} \sin(\theta) d\theta \tag{6}$$

following, there is the expectation value of the z-component of the dipole moment $\langle \mu_z \rangle$ that is:

$$\langle \mu_z \rangle = \int P(\theta) \mu \cos(\theta) dV \approx -\frac{\mu^2 B}{2 k_B T} \tag{7}$$

It is evident that the magnetisation is linearly dependent on the magnetic field applied, a higher magnetic field implies a higher net magnetisation that translates to a better image quality or a reduced acquisition time. An energy level can be associated with each spin state of the nucleus without an external magnetic field, the energy levels degenerate and when the magnetic field is applied the degeneracy is removed, there is a splitting of the energy levels. The energy level splitting phenomenon is called Zeeman effect [33], and the correspondent energy shift is proportional to the magnetic field strength, Figure 4, Table 1. The classical manifestation of energy splitting is the precessional motion of the magnetization about the magnetic field vector with a characteristic frequency ω_0. This frequency is known as the Larmor frequency and is linearly dependent on the magnetic field:

$$\omega_0 = \gamma B_0 \tag{8}$$

As shown in Figure 4, the associated difference between the energy states is:

$$\Delta E = \hbar \gamma B_0 \tag{9}$$

At the equilibrium state with an applied external magnetic field (i.e. along the z-axis), the net magnetization presents a non-zero longitudinal component, while the transversal averages to zero. Perturbing the system with an additional electromagnetic field will cause a change in transverse magnetization, and the longitudinal component might also change and possibly invert. When the perturbation is turned off, the system returns to the original equilibrium state under the influence of the static magnetic field. This process involves an energy transfer between the perturbed individual spins and their surrounding environment.

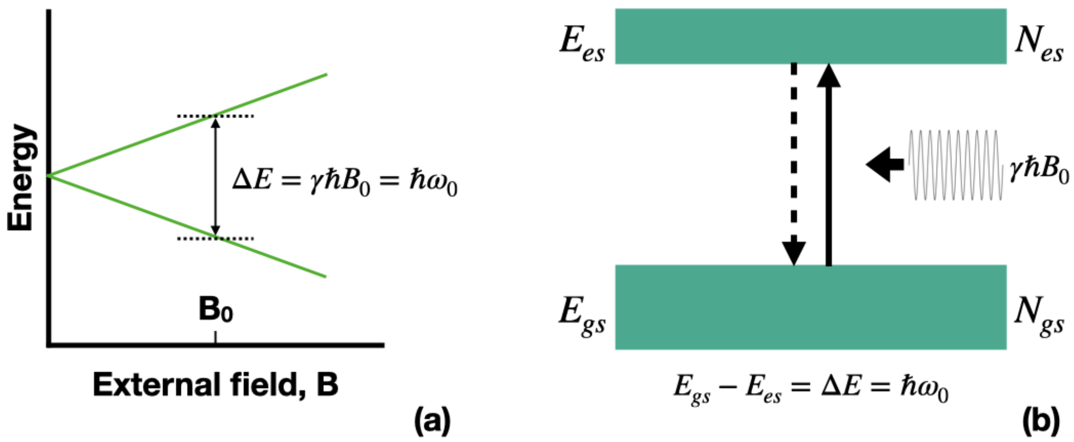

Figure 4: (a) The Zeeman effect, energy level diagram for a spin $\frac{1}{2}$ system, for $B = B_0$ the difference between the excited state; (b) band energy levels representation.

Considering the protons, the magnetization components present monoexponential decays characterized by time constants T_1 and T_2 when returning to the equilibrium state. The first time constant T_1 called longitudinal or spin-lattice relaxation time, provides information about the interaction between the spins and their environment. While the other time constant T_2, transversal or spin-spin relaxation time, is relative to the transverse magnetization decay and the interaction between the individual spins, technically representing an intrinsic irreversible loss of coherence. In reality, spin-spin relaxation is also affected by other effects, for instance, field inhomogeneity. The presence of other effects leads to the definition of an effective time constant called T_2^*:

$$\frac{1}{T_2^*} = \frac{1}{T_2} + \frac{1}{T_2'} \tag{10}$$

where the term T_2' refers to the relaxation time due to field inhomogeneity. Commonly, the T_2^* relaxation time is used as a marker of brain activity [34, 35] or to measure the local effects caused by paramagnetic material, such as iron deposition in the brain [36–39]. In general, the relaxation times in biological tissue are in the following order: $T_1 > T_2 > T_2^*$ [40]. The ensemble of spins ($\frac{1}{2}$-spin systems) placed in a static magnetic field and subsequently perturbed follows a temporal dynamics evolution that can be described by a set of three coupled first-order differential equations. These equations are derived from classical physics, and they are only a first-order approximation. Although the underlying principles are of quantum mechanical origin, the classical method leads to having the same results [41]. Considering the thermal equilibrium state, magnetization $\mathbf{M}$ and magnetic field $\mathbf{B}$ are aligned. The magnetization $\mathbf{M}$ will precess around the $\mathbf{B}$ direction if $\mathbf{M}$ is forced to point in another direction from $\mathbf{B}$ and additionally the resulting torque on the magnetization is: $\mathbf{M} \times \mathbf{B}$. Assuming a constant magnetic field $\mathbf{B}$, and neglecting the relaxation effects, the set of equations can be written as a vector rotation equation:

$$\frac{d\mathbf{M}}{dt} = -\gamma \mathbf{B} \times \mathbf{M} \tag{11}$$

where $\mathbf{M} = (M_x, M_y, M_z)^T$. When the magnetic field is: $\mathbf{B_0} = (0, 0, B_0)^T$, there is a rotation around the z-axis, and the correspondent rotation matrix is:

$$R_z(\theta) = \begin{bmatrix} 0 & \sin\theta & 0 \\ -\cos\theta & 0 & 0 \\ 0 & 0 & 1 \end{bmatrix} \tag{12}$$

thus, the magnetization follows:

$$\mathbf{M}(t) = -R(\omega_0 t)\mathbf{M}_{t=0} \tag{13}$$

the precession is at the Larmor frequency $\omega_0 = \gamma B_0$, and the components of $\mathbf{M}$ are:

$$\begin{aligned} M_x(t) &= M_{x,t=0}\cos\omega_0 t + M_{y,t=0}\sin\omega_0 t \\ M_y(t) &= -M_{x,t=0}\sin\omega_0 t + M_{y,t=0}\cos\omega_0 t \\ M_z(t) &= M_{z,t=0} \end{aligned} \tag{14}$$

The set of differential equations where the relaxation processes (spin-lattice and spin-spin relaxation) are taken into consideration are called **Bloch equations**:

$$\frac{d\mathbf{M}}{dt} = -\gamma \mathbf{B} \times \mathbf{M} + \begin{bmatrix} 0 \\ 0 \\ \frac{M_{eq}}{T_1} \end{bmatrix} - \begin{bmatrix} -\frac{1}{T_2} & & \\ & -\frac{1}{T_2} & \\ & & -\frac{1}{T_1} \end{bmatrix} \mathbf{M} \tag{15}$$

but they can be expressed in a compact form as:

$$\frac{d\mathbf{M}}{dt} = -\gamma \mathbf{B} \times \mathbf{M} - \frac{(M_x\hat{x} + M_y\hat{y})}{T_2} - \frac{(M_z - M_{eq})\hat{z}}{T_1} \tag{16}$$

where $\hat{x}, \hat{y}, \hat{z}$ are the unit vectors of the three spatial directions in the laboratory frame. In addition, other terms may be present to take into account, for instance, phenomena such as diffusion.

To make the Bloch equations easier to solve, it is often convenient to use the concept of a rotating frame of reference. Such a rotating frame is chosen so that it rotates around the z-axis with a frequency ω_r. Assuming the spin system is subject to a static magnetic field and an oscillating linear field $\mathbf{B_1}$ perpendicular to B_0 field written as:

$$\mathbf{B_1} = 2B_2 \cos(\omega_{rf} t)\hat{\imath} \tag{17}$$

and decomposing the $\mathbf{B_1}$ field as sum of right- and left-handed rotating magnetic field components, it is possible to observe that one component rotates with a reduced relative angular frequency in the same direction of $\mathbf{M}$. The effects of such components are neglectable because of an irrelevant the timescale for the measurement process. Furthermore, also neglecting the relaxation affects the Block equations can be reduced to:

$$\frac{d\mathbf{M}}{dt} = -\gamma[B_0\hat{z} + B_1(\cos(\omega_{rf}t)\hat{x} - \sin(\omega_{rf}t)\hat{y})] \times \mathbf{M} \tag{18}$$

The equation 18 describes the simple precession process around B_0, and transforming it into the rotating frame of reference (with frequency $\omega = \omega_{rf}$, where ω_{rf} is the frequency of the Radio Frequency (RF) wave), the unit vectors become:

$$\begin{aligned} \hat{x}_r &= \cos(\omega_{rf}t)\hat{x} - \sin(\omega_{rf}t)\hat{y} \\ \hat{y}_r &= \sin(\omega_{rf}t)\hat{x} + \cos(\omega_{rf}t)\hat{y} \\ \hat{z}_r &= \hat{z} \end{aligned} \tag{19}$$

therefore, it is possible to write the equation 18 as follow:

$$\frac{d\mathbf{M}_r}{dt} = -\gamma\mathbf{B_{eff}} \times \mathbf{M}_r \tag{20}$$

with $\mathbf{B_{eff}}$, the effective magnetic field:

$$\mathbf{B_{eff}} = B_1\hat{x}_r + \left(B_0 - \frac{\omega_{rf}}{\gamma}\right)\hat{z} \tag{21}$$

when the resonance condition is fulfilled, $\omega_{RF} = \omega_0$, only the transverse B_1 component determines the effective magnetic field.

There is another common mathematical representation to rewrite the Bloch equations 14, the axial representation, where the transverse components M_{xy} and B_{xy} are expressed as complex quantities:

$$\begin{aligned} M_{xy} &= M_x + iM_y \\ B_{xy} &= B_x + iB_y \end{aligned} \tag{22}$$

hence, the equations 14 can be written as:

$$\begin{aligned} \frac{dM_{xy}}{dt} &= -\gamma\left(M_{xy}B_z - M_z B_{xy}\right) - \frac{M_{xy}}{T_2} \\ \frac{dM_z}{dt} &= \frac{i}{2}\gamma\left(M_{xy}B_z^{\dagger} - M_z^{\dagger}B_{xy}\right) + \frac{M_{eq} - M_z}{T_1} \end{aligned} \tag{23}$$

When transforming to the rotating frame of reference in the axial representation the magnetization components are:

$$\begin{aligned} M_{xy,r} &= e^{-i\omega_0 t} M_{xy} \\ M_{z,r} &= M_z \end{aligned} \tag{24}$$

the transverse component is transformed with a simple multiplication, and the longitudinal one remains the same in both frames, laboratory and rotating.

The effects of the RF pulses on the magnetisation can be better understood by making use of the rotating frame of reference. A resonant RF pulse produces a magnetic field B_{xy}:

$$B_{xy} = B_1 e^{i(\varphi - \omega_0 t)} \tag{25}$$

that becomes a constant field in the rotating frame of reference:

$$B_{xy,r} = B_1 e^{i\varphi} \tag{26}$$

Considering an RF pulse with duration τ, short enough such that the relaxation effects can be neglected, the equations 23 can be written as follows:

$$\begin{aligned} \frac{d}{dt} M_{xy,r} &= iM_z\gamma B_{xy,r} = iM_z\gamma B_1 e^{i\varphi} \\ \frac{d}{dt} M_z &= i\gamma\left(M_{xy,r}B_{xy,r}^{\dagger} - M_{xy,r}^{\dagger}B_{xy,r}\right) \end{aligned} \tag{27}$$

with the symbol † indicating the complex conjugate. The solutions for transverse and longitudinal magnetization are:

$$\begin{aligned} M_{xy,r} &= \int iM_z\gamma B_1 e^{i\varphi} dt = e^{i\varphi}\left[C_+ e^{+i\gamma B_1 t} + C_- e^{-i\gamma B_1 t}\right] \\ M_z &= C_+ e^{+i\gamma B_1 t} + C_- e^{-i\gamma B_1 t} \end{aligned} \tag{28}$$

the terms $C_{\pm}$ indicate the constants of integration and they are determined by the initial values. In the initial state of equilibrium $t = 0$, the magnetization components are:

$$\begin{aligned} M_z(t=0) &= M_{eq} \\ M_{xy,r}(t=0) &= 0 \end{aligned} \tag{29}$$

and the constants of integration are:

$$C_+ = C_- = \frac{1}{2} M_{eq} \tag{30}$$

hence, the solutions for $M_{xy,r}$ and $M_{xy,r}$ become:

$$\begin{aligned} M_{xy,r} &= M_{eq} e^{i(\varphi + \frac{\pi}{2})} \sin(\gamma B_1 t) \\ M_{xy,r} &= \frac{e^{+i\gamma B_1 t} + e^{-i\gamma B_1 t}}{2} M_{eq} = M_{eq} \cos(\gamma B_1 t) \end{aligned} \tag{31}$$

These results tell us that the magnetization in the rotating frame of reference experiences a rotation arount the B_1 field (the RF field). There is a periodic magnetization transfer from the z-axis to the xy-plane and vice versa for the duration τ of the RF pulse. The rotation axis is in the xy-plane and the orientation of such axis is determined by the RF phase φ. Applying a short RF pulse, the magnetization experiences a constant external field in the $\mathbf{B_1}$ direction and precessing for the duration τ of the RF pulse. During the RF pulse the magnetization sweeps out an angle α, called Flip-angle (FA), and it can be easily calculated:

$$\alpha = \gamma B_1 \tau \tag{32}$$

The exponential term with the RF phase φ has a magnitude value equals to 1 and for this reason does not influence the FA. However, there are two particular cases:

- a $90°(\frac{\pi}{2})$ RF pulse rotates the magnetization by 90°, the longitudinal magnetization is transferred to the transverse plane (xy-plane);
- a $180°(\pi)$ RF pulse inverts the magnetization and the relative phases, acting as an inversion and refocusing pulse.

It is important to note that until this point, only the case where a perfectly resonant excitation RF pulse has been taken into account, but in practice this condition is not met all the time. There could be different reasons to have an "off-resonance" condition, for instance, the resonance is not achieved due to technical limitations, or it is a deliberate condition to excite specific portions (slice of interest) of the sample. Finally, assuming that the rotating frame frequency is the same as the RF field $\mathbf{B_1}$, the Bloch equations can be written as follows:

$$\begin{aligned} \frac{d}{dt} M_{xy,r} &= -i\gamma(B_0 - B_1) M_{xy,r} + i M_z \gamma B_1 \\ \frac{d}{dt} M_z &= i\gamma\left(M_{xy,r} - M^{\dagger}_{xy,r}\right) B_1 \end{aligned} \tag{33}$$

These equations can be solved only for special cases, and there is no general analytical solution. The precession frequencies of the magnetization and RF pulse are not equal, and this is reflected by the off-resonance term in $\frac{d}{dt} M_{xy,r}$. The consequences of the off-resonance condition are a persistent slow precession and a frequency shift. In practice, the off-resonance leads to a reduced efficiency of the RF pulse without achieving the desired flip-angle, usually lower and additionally, there is a non-zero phase contribution on the transverse magnetization. When the off-resonance is significantly large, it is possible to have no excitation at all, and although no excitation takes place, still this the condition can be desirable for some imaging applications.

The next crucial point in MRI is the use of spatial magnetic field gradients. Magnetic field gradients are:

- used to select imaging slices;
- manipulate the phase of the processing spins;
- essential for spatial encoding.

The magnetic field is generated in order to have a linear dependency with the position $\mathbf{r} = (x, y, z)^T$, in practice, given the magnetic field gradient $\mathbf{G} = (G_x, G_y, G_z)^T$:

$$B(\mathbf{r})\hat{z} = \big(\mathbf{G}(t) \cdot \mathbf{r} + B_0\big) \tag{34}$$

Thus, the spin dynamics become spatially dependent and considering the rotating frame of reference with frequency $\omega_r = \gamma\big(\mathbf{G} \cdot \mathbf{r} + \mathbf{B}_0\big)$, the transverse magnetisation evolution can be written as follows:

$$\frac{d}{dt}M_{xy,r} = i\gamma\mathbf{G}(t) \cdot \mathbf{r}M_{xy,r} - \frac{M_{xy,r}}{T_2} \tag{35}$$

the latter equation has the following solution, equation 36, as shown by Nishimura et al. [42]:

$$M_{xy,r}(t) = M_{xy,r}(t=0)e^{-\frac{1}{T_2}t}e^{i\int_0^t \gamma\mathbf{G}(t)\cdot\mathbf{r}dt} \tag{36}$$

furthermore, the integral $\int_0^t \gamma\mathbf{G}(t) \cdot \mathbf{r}dt$ can be decomposed yielding to:

$$M_{xy,r}(t) = M_{xy,r}(t=0)e^{-\frac{1}{T_2}t}e^{i\gamma(\int_0^t G_x x dt+\int_0^t G_y y dt+\int_0^t G_z z dt)} \tag{37}$$

besides considering the relation:

$$k_n = \frac{\gamma}{2\pi}\int_0^t G_n dt, \qquad with \qquad n = x, y, z \tag{38}$$

the previous solution (eq. 37) can be rewritten as:

$$M_{xy,r}(t) = M_{xy,r}(t=0)e^{-\frac{1}{T_2}t}e^{i2\pi(k_x x+k_y y+k_z z)} \tag{39}$$

The key role of gradients is to create a phase difference depending upon the value of $\mathbf{k}$. Image information is recovered by making use of this property. Further, the major important characteristic of the gradients is the time integral, also called gradient moment, it constitutes the net effect of the gradient. Although the gradient shape is also an important factor to consider, it has a minor impact. The gradients for the three orthogonal spatial dimensions are:

$$\begin{aligned} \mathbf{G_x} &= \big(\partial B/\partial x, 0, 0\big)^T \\ \mathbf{G_y} &= \big(0, \partial B/\partial y, 0\big)^T \\ \mathbf{G_z} &= \big(0, 0, \partial B/\partial z\big)^T \end{aligned} \tag{40}$$

To obtain an MRI signal, it is essential that the rotating transverse magnetisation is present, and it can be detected by a radio frequency coil. An RF coil allows having an inductive coupling with the precessing magnetisation. When the system is in its equilibrium state, there is no transverse magnetisation, and consequently, no signal is detected. Disturbing the equilibrium state by applying, for example, an RF pulse, the transverse magnetisation will assume a non-zero value, and the signal generated will be detected by the coil. The detected signal is characterised by a carrier frequency equal to the Larmor frequency, i.e. the precession frequency of magnetisation. The exponential decay T_2^* characterises the envelope of the measured signal S, when the transverse magnetisation is in the relaxation phase. The measured signal S is called Free Induction Decay (FID) and is maximum after a 90° RF pulse, when all the longitudinal magnetisation is transferred into the transverse plane.

In practice, the FID signal is not commonly used for acquiring images because the time required by the spatial encoding being too long, and the signal is lost before the image can be encoded. To overcome the loss of signal, the FID is refocused to create echoes, making image acquisition feasible. The Echo Time (TE) is indicated as the time after which an echo occurs. Technically, TE is measured from the centre of the RF pulse to the time of the peak echo amplitude. There are different echo signals that can be obtained using a proper combination of RF pulses. The most common ones are: **spin**, **gradient** and **stimulated echoes** [43–45].

- **Spin echoes** are obtained applying an RF refocusing pulse onto dephased transverse magnetization. In particular, the refocusing pulse is applied at the time $\frac{TE}{2}$, before it, the magnetisation experiences a dephasing caused by the field inhomogeneity and an intrinsic non-reversible relaxation. With the refocusing pulse, the magnetisation is mirrored along the axis of the pulse, the reversible effects are cancelled, and finally, a signal peak occurs. A spin echo has an envelope of two FIDs facing each other, and the peak at TE is characterised by the T_2 signal loss. Choosing the TE value appropriately, it is possible to have a different amount of T_1 or T_2 contrast dependency in the image. The spin echo sequence is obtained from an $90°(\frac{\pi}{2})$ RF pulse followed by one or more $180°(\pi)$ refocusing pulses. An important advantage of using refocusing pulses in spin echo sequences is better robustness against susceptibility artefacts when compared to gradient echo sequences [43].

- **Gradient echoes** are instead recovered exploiting the effect of a gradient used to support dephasing along a specific spatial direction and with another gradient of opposite polarity but the same gradient moment of the first one [45].

- **Stimulated echoes** are the result of the application of a minimum of three consecutive $90°(\frac{\pi}{2})$ RF pulses. Sequentially, the first pulse creates coherent transverse magnetisation, the second pulse transforms the transverse magnetisation into longitudinal and the last pulse retrieves the longitudinal magnetisation into the transverse plane allowing a refocusing of the magnetisation and the formation of an echo [44].

The receiver coil in an MR scanner detects a signal only in the transverse direction, and such signal reflects the magnetic flux changes that can be expressed in terms of transverse magnetization. Considering the contribution of each spin in the receptive volume of the receiver coil, and assuming that the coil has a uniform sensitivity is possible to calculate the signal as the integral of all contributions:

$$S_t(\mathbf{r}, t) \propto \iiint_V M_{xy}(\mathbf{r}, t) dV \tag{41}$$

Replacing with the appropriate form of the Bloch equations, the signal becomes:

$$S_t(r, t) \propto \iiint_V M_{xy,r} e^{i\omega_0 t} dV = e^{i\omega_0 t} \iiint_V M_{xy,r} dV \tag{42}$$

The Larmor frequency is taken out of the integral because there is the assumption that the external field is homogeneous in the Region-Of-Interest (ROI), hence independent of position. Furthermore, considering that the detected signal is demodulated, the Larmor frequency term can be omitted:

$$S_t(\mathbf{r}, t) \propto \iiint_V M_{xy,r} dV \tag{43}$$

The demodulation of the signal corresponds to a direct measurement in the rotating frame of reference.

1.4 IMAGE FORMATION IN MRI

The MR images encode information from signals sourced by 3D voxels, using a correct combination of gradients. Gradients are particular loops of wire or conductive sheets on a cylindrical shell placed inside the bore of the scanner. When the gradients are activated, an additional magnetic field is created, the latter distorts the main magnetic field, and as a result, the resonance frequency of spins varies as a funtion of their position, Figure 5. In this manner, the gradients allow the spatial encoding of the MR signal.

Considering a simple 2D MRI sequence (Figure 6 (a)) three main blocks constitute the entire process: slice selection, obtained with the first gradient, called Slice Selection gradient (G_{SS}), Figure 5; Frequency Encoding gradient (G_{FE}) and Phase Encoding gradient (G_{PE}), basically to move inside the plane just selected with the slice selection. It is possible to vary the combination of the gradients to obtain more complex spatial encoding methods.

The first step to localise a signal from a specific slice is obtained applying a gradient (G_{SS}) simultaneously with an RF pulse that will excite the slice, where the spins will be flipped to the transverse plane. When a linear gradient is applied,

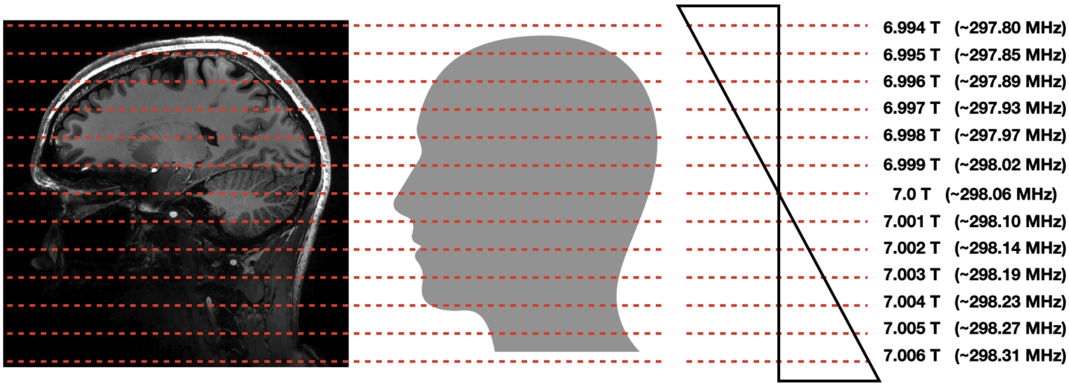

Figure 5: Application of the slice selection gradient G_{SS}. On the right side there are reported how the frequency varies accordingly with the strength of the gradient applied.

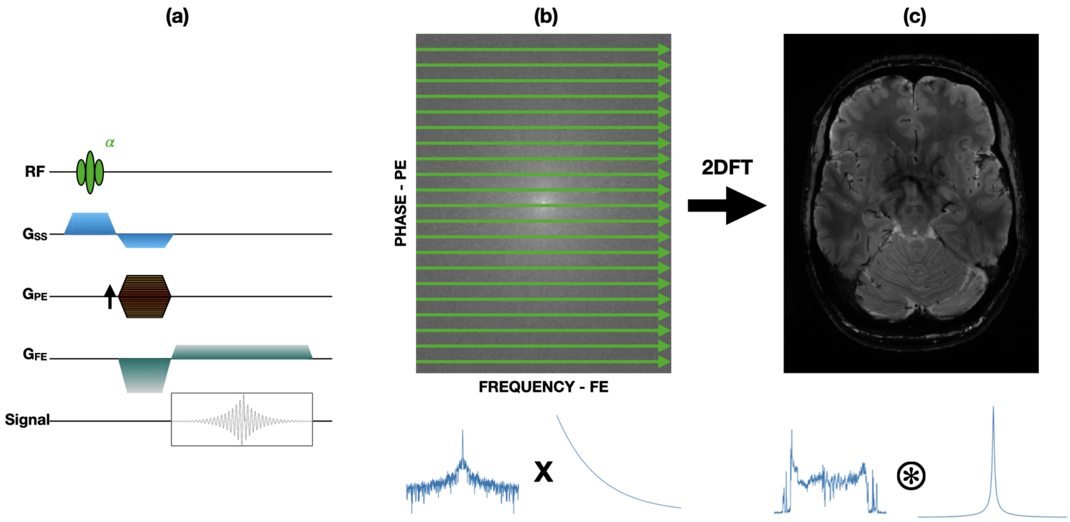

Figure 6: Image acquisition of a T_2^*-weighted 2D gradient image. (a) Pulse sequence diagram; (b) k-space 2D-image and (c) reconstructed 2D-image.

the Larmor's frequency of the spins are subject to a linear dependency with the position along the gradient, Figure 5.

The simultaneous application of a narrow-band RF pulse with the slice selection gradient ensures that the resonance condition is only met in a subset of voxels, the slice perpendicular to the applied gradient. Taking into account the rotating frame of reference and a local off-resonance due to a gradient $\mathbf{G}_r$, the frequency offset is given by $\omega_r - \omega_0 = \gamma \mathbf{G}_r \cdot \mathbf{r}$. The RF pulse $B_{xy,r} = B_1 e^{-i(\omega_{rf} - \omega_r)t + i\varphi}$ with frequency ω_{RF} modifies the transverse magnetisation as follow:

$$\frac{d}{dt} M_{xy,r} = i\gamma \mathbf{G}_r \cdot \mathbf{r} M_{xy,r} + i M_z \gamma B_1(t) e^{-i\omega_{rf} + i\varphi} \tag{44}$$

A small flip angle guarantees a non-significant impact on the longitudinal magnetisation by the RF pulse, thus the longitudinal and transverse magnetisation is decoupled, therefore the solution:

$$M_{xy}, r(t, r) = ie^{i\varphi} M_{eq} e^{-i\gamma \mathbf{G}_r \cdot \mathbf{r} t} \int_0^t e^{i\gamma \mathbf{G}_r \cdot \mathbf{r} t} \gamma B_1(t) dt \tag{45}$$

and considering a pulse of duration τ:

$$M_{xy}, r(t, r) = ie^{i\varphi} M_{eq} e^{-i\gamma \mathbf{G}_r \cdot \mathbf{r} \frac{\tau}{2}} \int_{-\frac{\tau}{2}}^{\frac{\tau}{2}} e^{i\gamma \mathbf{G}_r \cdot \mathbf{r} t} \gamma B_1(t + \frac{\tau}{2}) dt \tag{46}$$

The integral indicates the Fourier Transform (FT) of the envelop function of the RF pulse, the time evolution of the RF pulse is related to the slice profile, which excites the spins that is under the influence of the gradient. It is clear that the slice has a width (slice thickness) dependent on the bandwidth of the RF pulse and the gradient slope. A sinc-shaped enveloped is used to excite a rectangular slice, considering that a FT of a sinc profile is rectangular. Accordingly to the Fourier Theorem, an envelope requires an infinite long pulse duration and this does not exist in reality, for this reason, the pulse is truncated. As a consequence of the truncation, the slice profile extends outside of the desired slice. Therefore, to avoid image artefacts, a non consecutively sampling is used, no slices are directly adjacent to each other. The slice centre is given by $r_s = \frac{\omega_{rf} - \omega_0}{\gamma G_r}$, while the slice thickness $\Delta d = \frac{\Delta\omega_{rf}}{\gamma G_r}$ is strictly dependent from the RF pulse bandwidth $\Delta\omega_{RF}$, and the strength of the applied gradient $G_r = |\mathbf{G}_r|$. If the RF pulse has an arbitrary shape, the bandwidth can be defined as the full-width-at-half-maximum (FHWM). It is important to consider also the phase term before the FT because the applied RF pulse causes the transverse magnetisation to be dephased. The dephasing needs to be removed to allow an optimal signal acquisition from the selected slice. Inducing a phase shift in the opposite direction is possible to remove the dephasing, this can be done by applying a gradient with half the gradient moment of the slice selection gradient, as shown in Figure 6 (a), G_{SS}.
Once the slice selection has been applied along the z-axis it is possible to select a specific section of that slice along the x-axis (column-wise). All the spins along the x-axis of the slice have the same frequency and phase but different amplitudes, summing up all the signals will result in a large wave of the same frequency. By applying another magnetic gradient in the x-axis G_{FE}, usually called "read out" or "frequency gradient", the Larmor frequencies of the spins will vary along that direction. In this way, there will be signals with different frequencies depending on the location along the slice and eventually, they will have different phases. Now the signals summary produces a large signal at the start, because they are in phase, and then there is a drop off as the phases diverge.

As stated above, applying a magnetic field gradient for an interval of time, δt, implies a linear variation with the position along the applied gradient of the Larmor frequency. The time integral of the Larmor frequency is the phase angle $\Delta\varphi$

and it is also linearly dependent on the position: $\frac{d}{dt}M_{xy,r} = i\gamma\mathbf{G}\cdot\mathbf{r}M_{xy,r}$ with the following solution $M_{xy,r}(t+\delta t) = M_{xy,r}(t)e^{i\gamma\mathbf{G}\cdot\mathbf{r}\delta t}$. After a fixed amount of time δt, the phase angle is $\Delta\varphi = \gamma\mathbf{G}\cdot\mathbf{r}\delta t$. To better understand phase encoding, we can consider it in terms of sampling for periodicity. Considering a homogeneous object, after the application of the phase encoding gradient, we will obtain a very small signal from the whole object. The main reason behind this behaviour is that the induced phase shifts disperse the magnetisation, and consequently, there is a small net transverse magnetisation. If we now consider an object with a specific periodicity along the gradient direction, we will have a gradient strength at which the object's periodicity is equal to the phase term induced by the gradient. This means that all the spins in the periodic object will have a phase always multiple of 2π, and the transverse magnetisation is aligned, resulting hence in a large signal. It is possible to observe and measure the spatial frequencies relative to the periodicity by applying a different gradient strength each time and repeating the steps. The measured signal after each phase encoding step can be finally used to reconstruct the corresponding MR image through the Fourier transform. Furthermore, phase encoding can be performed in all dimension, 1-, 2- and 3-dimensions, but the latter one is rarely performed due to the long scan time.

In general there are several modes of encoding in MRI: 1D (a spectrum of profile), 2D (one slice or many single slices), 3D (slab selection), 4D (3 spatial dimesions plus an extra dimension that could be for instance the frequency when acquiring a spectra for each voxel) and also higher dimensionalities are possible. The 2D imaging is the one descripted above and is on a per slice basis. As mentioned earlier, in a slice excited via slice selection (G_{SS}), the in-plane dimensions are encoded with G_{PE} and G_{FE}. Whilst, a 3D imaging method consists in a 2D phase encoding and a frequency encoding for the remaining dimension. Obviously each imaging method, 2D or 3D, presents advantages and disadvantages. For 2D methods the main advantages are first of all the scan time, 2D acquisition are usually faster and secondarily images are not prone to so called aliasing artefacts, however, as discussed above the slices cannot be acquired consecutively or too close together due to the fact that the slice profiles might overlap and crosstalk introducing artefacts. Instead, with regard to 3D methods, there is the disadvantage of a longer scan time due to the higher number of encoding steps, but on the other side there is no need to consider the slices profile and for this reason all the voxels can be selected adjacent to each other in all spatial dimensions. When it is required to acquire a specific ROI also usually called "slab", a 3D method can prevent the excitation outside of such region.

All the voxels at position $\mathbf{r} = (x, y, z)^T$ contribute to the magnetisation, but each voxel has a frequency $\omega(\mathbf{r}, t)$ and phase offset φ:

$$\begin{aligned} M(\mathbf{r}, t) &= M_i(\mathbf{r}, t)e^{i(\omega(\mathbf{r},t)t+\varphi(\mathbf{r},t))}\Lambda(\mathbf{r}) \\ \omega(\mathbf{r}, t) &= \omega_0 + \mathbf{G}\cdot\mathbf{r} \end{aligned} \tag{47}$$

the term $M_i(\mathbf{r}, t)$ is referred to the magnetisation before spatial encoding begins while the slice selection function is $\Lambda(\mathbf{r})$. The function $\Lambda(\mathbf{r})$ describes the slice profile and for an ideal 2D rectangular slice:

$$\Lambda(\mathbf{r}) = \text{rect}\left(\frac{2z}{\Delta z}\right) \tag{48}$$

assuming the frequency encoding in the x-axis direction:

$$\omega(x) = \omega_0 + \gamma \int_0^t G_x x dt \tag{49}$$

then, the phase encoding in the y-axis direction for a time duration τ:

$$\varphi(y) = \gamma \int_0^\tau G_y y dt \tag{50}$$

and z the slice selection direction, the signal equation becomes:

$$\begin{aligned} S(x, y, z, t) &\propto \Delta z \int\int_{x,y} M_i(x, y, z_0, t) e^{i(\omega(x)t + \varphi(y))} dx dy \\ &= \Delta z \int\int_{x,y} M_i(x, y, z_0, t) e^{i\omega_0 t + 2\pi i(k_x x + k_y y)} dx dy \end{aligned} \tag{51}$$

taking into account that the spatial frequencies are the time integral of the gradients:

$$k_n = \frac{\gamma}{2\pi} \int_0^t G_n dt, \quad n = \{x, y, z\} \tag{52}$$

and for this particular case:

$$\begin{aligned} k_x &= \frac{\gamma}{2\pi} G_x \tau \\ k_y &= \frac{\gamma}{2\pi} G_y \tau \end{aligned} \tag{53}$$

these represent the basis of the "k-space" or the acquired MRI data [46]. Choosing how and when gradients are applied allows a large number of possible k-space trajectories to acquire the MRI data. However, to reconstruct an image from raw data, a proper trajectory has to be chosen in order to collect enough information. Furthermore, the signal equation assumes the form of a FT in 2D or 3D when phase manipulation is executed by gradients:

$$S(x, y, t) \propto \int\int_{x,y} M_{i,r}(x, y, z_0, t) e^{2\pi i(k_x x + k_y y)} dx dy \propto \text{FT}\left\{M_{i,r}(x, y, z_0, t)\right\} \tag{54}$$

The signal contains information about the transverse magnetization of the ROI, and for the FT a step-by-step the process is executed in order to fill the image matrix:

$$\begin{aligned} S(x, y, t) &\propto \int\int\int_{x,y,z} M_{i,r}(x, y, z_0, t) e^{2\pi i(k_x x + k_y y + k_z z)} dx dy dz \\ &\propto \text{FT}\left\{M_{i,r}(x, y, z, t)\right\} \end{aligned} \tag{55}$$

$S = S(k_x, k_y, k_z, t)$ is the signal in the k-space.

The FT underlies the relationship between k-space and image space. This relationship makes easy the calculation of the FoV and the voxel size δ through the following:

$$
\begin{aligned}
FOV_{x,y,z} &= \frac{1}{\Delta k_{x,y,z}} = \frac{N_k}{k_{max}}\Big|_{x,y,z} \\
\delta_{x,y,z} &= \frac{1}{k_{max}}\Big|_{x,y,z}
\end{aligned}
\tag{56}
$$

Δk refers to the k-space line spacing, N_k to the matrix size and $k_{max}$is the maximum k-space value. The resolution is limited by two main factors: the maximum gradient strength and the receiver bandwidth (directly related to the maximum detectable frequency) [41].

1.5 MOTION ARTEFACTS

Motion during MR acquisitions leads to effects such as image unsharpness, contrast degradation, ghosting (both coherent and incoherent), signal loss caused by the spin dephasing or unwanted magnetization evolution and also the possibility of observing strong undesired signals, see Figure 7. Obviously, these artefacts can interfere with the diagnosis or do not allow a correct post-processing analysis as brain extraction, segmentation and so on. Practically, there are two main factors that directly influence the amount of motion corruption, resolution of the acquired image and the scan time. A higher image resolution will correspond to a higher sensitivity to motion artefacts, similarly a longer scan time means a higher probability of having the subject's movements.

In order to correct or mitigate motion artefacts, it is fundamental to understand the physical principles behind the generation and the appearance of them in an MR image. Motion artefacts are generally a result of a complex interaction between several factors, more specifically: the structures imaged, the type of motion, the MR pulse sequence parameters and the k-space pattern acquisition.

As described in section 1.4, the spatial encoding consists of a repetition of many sequential steps, and this process are intrinsically slow when compared, i.e., to computed tomography (CT). The data acquisition occurs in the "k-space", and this corresponds to the spectrum of the spatial frequencies of the scanned object [46]. The k-space is characterised by having the low frequencies in its centre and the high frequencies in the periphery. The low frequencies provide us with information about contrast and shapes, while the high frequencies complement this with information about edges and details [46]. In general, biological samples present a very local spectral density in k-space, centered around $k = 0$, and for the brain cortex it is possible to observe a fractal-like nature [47]. The fractal-like nature corresponds to a slower decay of spectral density in k-space. The relationship between

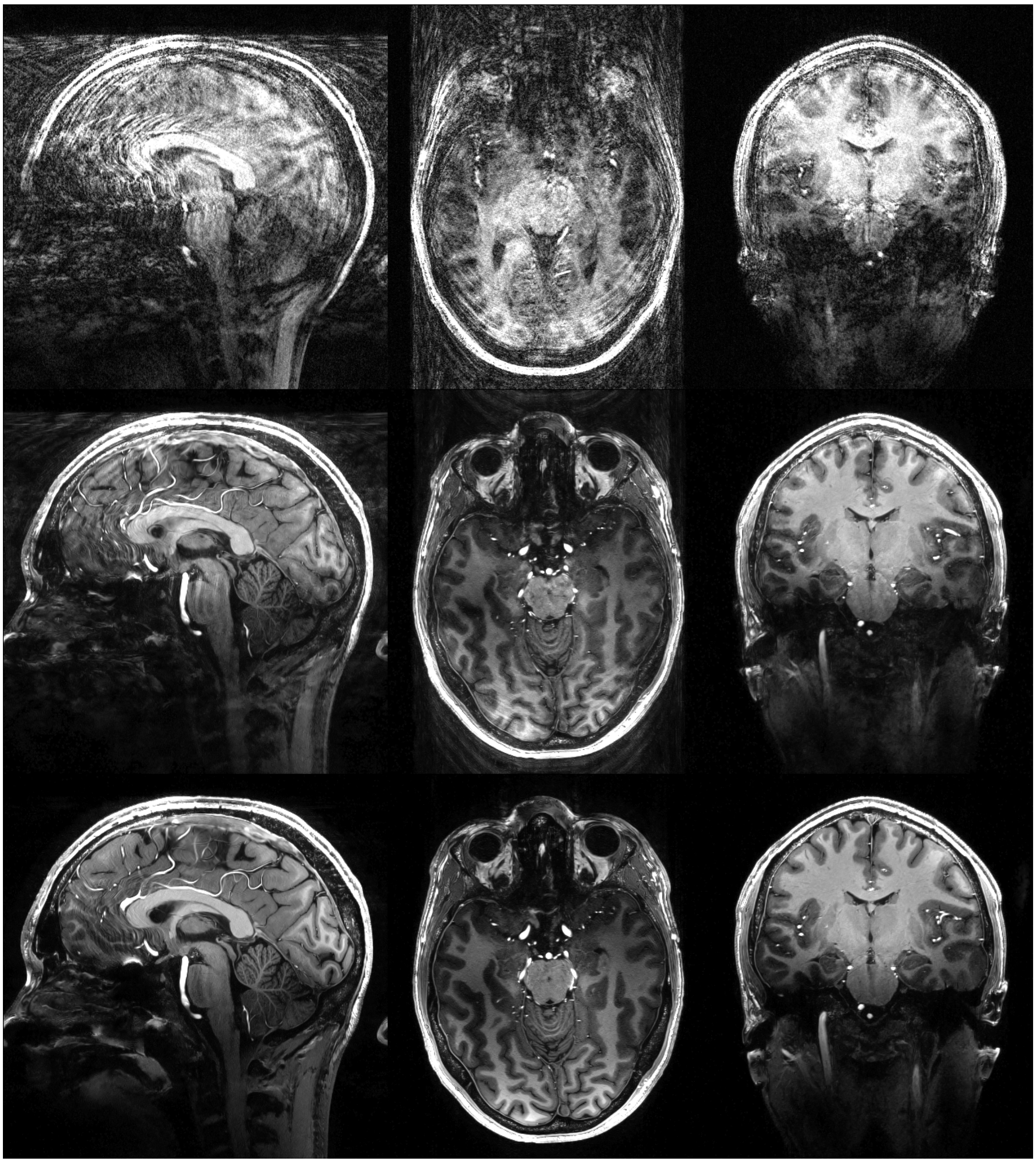

Figure 7: Motion artefacts for a T1-weighted volume acquired at 7T with a 3D-MPRAGE sequence. Left side: sagittal view; centre: axial view; right: coronal view. Top row: heavy level of corruption; middle row: mild level of corruption; bottom row: no motion artefacts.

Sources	Type	Occurence	Pattern	Direction
physiological	rigid	intra-scan	periodic	in-plane
tremors	non-rigid	inter-scan	quasi-periodic	trough-plane
children	fast	inter-image	continuos	
	slow		random	

Table 2: Sources, type, occurence, pattern and direction of motion.

the image space and the acquired k-space tells us that every sample in k-space affects the entire image, this becomes obvious simply considering that an object is described by a set of global planar waves in the k-space. Thus, when there is a single sample change in k-space the entire image is affected by this variation.

Blurriness and ghosting effects are related to the signal readout process, while signal loss and the strong undesired signals appearance is related to signal generation and the chosen sequence parameters. In practice, the ghosting effect is a partial or complete repetition of the imaged object along the phase-encoding direction. When the periodic motion is synchronized with the k-space sampling, the coherent ghosting effect appears in the image. The coherent ghosting is characterized by having a precise number of replicas [48–50]. Instead, when the periodicity in k-space is violated, then incoherent ghosting appears. It can be observed as multiple overlapped replicas and, in some cases, also as stripes in the phase-encoding direction. The assumption at the basis of the MR image reconstruction is that the object remains stationary during the scan time, any violation of the stationary status will result in artefacts. The inconsistencies are the main cause of the readout-related motion artefacts. Based on the above knowledge, it is possible to list a few common situations, i.e.:

- when using a sequential k-space acquisition, "slow continuous drifts" will have a minor impact in terms of motion artefacts;
- very strong ghosting artefacts appear in case of periodic motion;
- for a particular case, such as interleaved multishot acquisition, also slow continuous drifts can produce significant ghosting artefacts.

This list can be extended by adding many other case scenarios, but it is beyond the scope of this thesis work. In Table 2 there are shown the main characteristic of motion divided as follows: source, type, occurrence, pattern and direction. Motion can be characterised by the combination of simultaneous type of patterns, i.e., periodic plus random, and so on, combining all the specifics shown in Tab. 2. Despite a large number of possible combinations, the basic mechanism of data corruption takes into account the following processes:

- incorrect phase accumulation;
- excitation history effects;

- B_0 and B_1 distortions;
- effects of rotations will result in a non-homogeneous sampling of the k-space for multi-shot imaging;
- physiological noise caused by cardiac or respiratory motion.

The tissue motion is the cause of an incorrect phase accumulation when the gradients are turned on. As mentioned in section 1.3, the signal acquired is the result of echoes, but if the tissues are not stationary during the scanning, then spins acquire an additional phase if moving in the direction of the gradient. Inconsistencies will appear as a result of the phase variation for the different phase-encoding steps [51].

Another important aspect has to be considered when the slice-selective RF pulses are used because they can generate artefacts called "excitation history effects". When considering out-of-plane or trough-plane motion between these RF pulses, the main effect is an alteration of the signals, very weak or very strong. In this case, the k-space will present magnitude inconsistencies.
Furthermore, the motion of the tissues can sensibly alter the magnetic static B_0 field, this is mainly due to the long-ranging magnetic susceptibility effects [52, 53]. Also, the B_1 fields, relative to transmission and detection of the MR signal, may also vary accordingly with the body position [54].
Furthermore, it is also important to mention the effects caused by the rotations during the acquisition process in multi-shot imaging. For this particular case, even if there is applied some sort of compensation technique, the k-space will be non-homogeneously sampled, and typical motion artefacts will degrade the image quality [55, 56].
The last factor to take into account as a mechanism of data corruption is the physiological noise, mainly due to breathing or cardiac motion. This is mostly affecting the functional imaging acquisitions, where signals are usually very small, and the physiological noise can be a confounding factor during the post-processing analysis [57].

Despite all the efforts of researchers in solving the problem of motion artefacts, there is no definitive solution to date [58]. However, for both clinical and research applications, there are available several approaches to limit or avoid image degradation due to motion. In Table 3 there are shown the three main strategies to mitigate or partially solve the problem of motion artefacts in MRI: motion correction techniques, prevention of body motion during the scan and the artefact reduction [32, 41, 59].

Motion correction	Motion prevention	Artifact reduction
Prospective	Breathhold	Gradient moment nulling
Retrospective	Sedation	Triggering and gating
Deep Learning Retrospective	Training	Faster imaging
Navigators	Foam restraints	Insensitive sequences
Self-navigated trajectories	Distraction	Phase reordering
	Head holders	Saturation bands
	Feed and wrap (babies)	

Table 3: Main strategies to mitigate motion artefacts in MRI.

Why moving spins accumulate phase: a short mathematical description

The intricacies of spin movements play a pivotal role in image acquisition and quality. Techniques such as phase-contrast imaging proficiently capture the motion patterns of spins within the sample, offering critical insights into internal dynamics. The scan pattern of the MRI device, notably the phase-encoding direction, is intrinsically linked to the manifestation of artefacts, most notably wrap-around and flow/motion artefacts. The latter, predominantly resultant from moving spins accruing phase during the readout phase, engenders blurring in the resultant images, attributed to a quadratic phase term. To ameliorate such distortions, flow-compensation strategies, including gradient-moment nulling, are employed. These sophisticated techniques meticulously adjust the waveforms of imaging gradients, thereby correcting for flow-related dephasing. Consequently, an understanding of the interconnectedness of motion patterns, scan patterns, and flow artefacts is indispensable in optimising MRI technology, as these elements collectively influence the fidelity of the spins' movements within an MRI sample, thereby dictating the quality of the resultant imaging.

When the spins in an MRI sample are moving, they accumulate a phase that is proportional to their velocity. This phenomenon is known as phase accumulation. The phase of a moving spin can be described by a mathematical formula that involves the spin's position, velocity, and time

$$\phi = \gamma \cdot G \cdot t \cdot x \tag{57}$$

where ϕ is the phase, γ is the gyromagnetic ratio, G is the gradient strength, t is the time, and x is the position of the spin. The phase accumulated by a spin at position $\mathbf{r}$ over time t is the integral of its Larmor frequency, which depends on the local magnetic field:

$$\phi(\mathbf{r}, t) = \gamma \int_0^t B(\mathbf{r}(\tau))d\tau \tag{58}$$

Substituting the expression for $B(\mathbf{r})$:

$$\phi(\mathbf{r}, t) = \gamma \int_0^t [B_0 + \mathbf{G} \cdot \mathbf{r}(\tau)] d\tau \tag{59}$$

For rigid body motion, the position $\mathbf{r}(t)$ can be expressed as a function of the initial position $\mathbf{r}_0$ and the motion parameters. Assuming a translation $\mathbf{T}(t)$ and a rotation represented by a rotation matrix $\mathbf{R}(t)$, the position at time t is:

$$\mathbf{r}(t) = \mathbf{R}(t)\mathbf{r}_0 + \mathbf{T}(t) \tag{60}$$

Phase accumulation due to rigid body motion can be expressed by substituting the expression for $\mathbf{r}(t)$ in the phase equation:

$$\phi(\mathbf{r}_0, t) = \gamma \int_0^t [B_0 + \mathbf{G} \cdot (\mathbf{R}(\tau)\mathbf{r}_0 + \mathbf{T}(\tau))] d\tau \tag{61}$$

Neglecting the effect of B_0 and considering it being uniform across the region of interest, its contribution to phase can be ignored for the analysis of motion effects. Therefore, the equation can be simplified as:

$$\phi(\mathbf{r}_0, t) = \gamma \int_0^t \mathbf{G} \cdot (\mathbf{R}(\tau)\mathbf{r}_0 + \mathbf{T}(\tau)) d\tau \tag{62}$$

The mathematical formulation can be extended for non-rigid body motion [60], but are not presented here as they are out of the scope of this thesis.

1.6 GOAL OF THIS THESIS

The focus of this thesis work is to qualitatively and quantitatively analyse two motion correction strategies: prospective motion correction (PMC) with an OMTS for ultra high-resolution brain imaging at 7T (Sec. 2 and 4) and additionally a second part for deep learning based retrospective motion correction (Deep Learning based RMC (DL-RMC)) (Sec. 3 and 5), used for the detection, quantification and correction of motion artefacts in case of brain imaging at high field MRI (1.5 and 3.0 T).
PMC is a well-established general technique proposed the first time by Haacke and Patrick in 1986 [61]. It consists of a real-time update of the pulse sequence using tracking data that can be acquired by different modalities.
While DL-RMC is a rather recent strategy that makes use of artificial intelligence techniques, and specifically training deep learning models or "neural networks" in order to perform the different tasks, detection, quantification and correction, as specified above.
Both strategies obviously present advantages and disadvantages, along with their limitations in applicability, and this will be examined in the course of this thesis work.

Part II

PMC AND DEEP LEARNING BASED RMC

2 PROSPECTIVE MOTION CORRECTION

2.1 MRI HARDWARE

Before proceeding with the details regarding PMC, the hardware setup is briefly described here. The main component of an MRI system is a very large magnet that generates a strong static magnetic field (B_0, 140000 bigger than B_{earth}). Follows another fundamental component: the gradient coil. An MRI scanner has three sets of gradient coils integrated inside the bore of the main magnet, see Fig. 8. The gradient coils allow for generating additional magnetic fields, specifically along the x, y and z directions, with which the required linear changes in the imaging volume are possible. The last main hardware component is the RF coil, which also can be integrated into the scanner bore, and this is known as the body coil. However, the RF coils are one of the most customizable hardware in an MRI scanner. For the in-vivo measurements made in this work, a birdcage RF coil has been used. Typically a birdcage coil presents a cylindrical shape, and it is built by a variable number of rung segments. The RF coil is used to transmit and receive the time-variant magnetic field B_1 [32, 41, 62, 63].

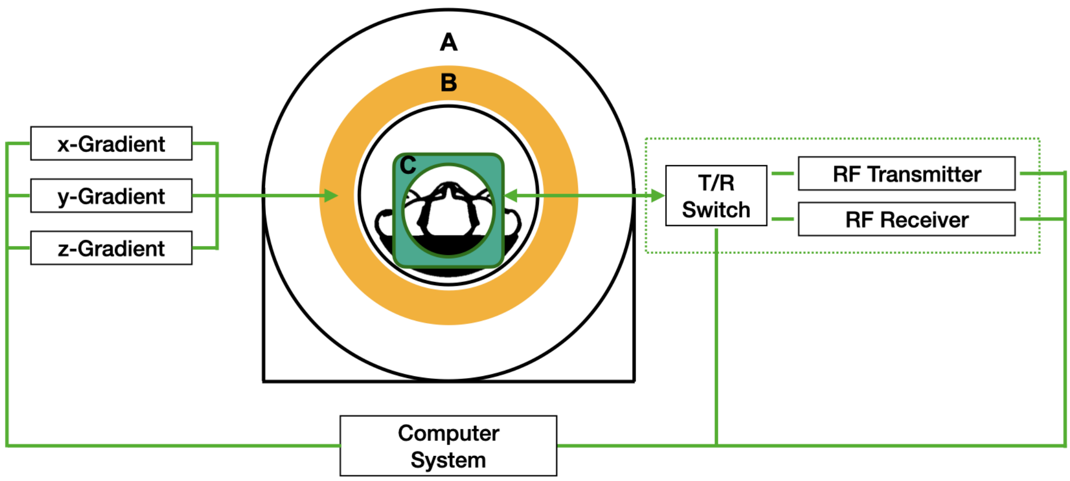

Figure 8: Schematic representation of an MR scanner. A is the magnet, B is the gradient coils, and C is the head coil.

Here is the hardware list of the system used:

- Magnet: 7T Magnetom whole-body MRI (Siemens Medical Solutions, Erlangen, Germany), 1H Larmor frequency 297.14 MHz, 5-6 l/d liquid Helium boil off without scanning, 60 cm bore size, 90 cm warm bore, passively shielded with 230t of iron;

- Gradients: Whole-body gradient coil SC72 (maximum gradient strength: 70mT/m, slew rate: 200 T/m/s);
- Coil: Siemens (Nova Medical, Wilmington, MA, USA) 1TX / 32RX Channel Head Coil with mirror mount for visual stimuli;
- Console: Siemens Syngo VB17.

Although a detailed description of the hardware and operation of an MRI scanner is of paramount importance, this thesis work is beyond that scope and for further details on the topic, please refer to the following reference textbooks [64–66].

2.2 PROSPECTIVE MOTION CORRECTION

The term prospective motion correction (PMC) refers to the correction technique by real-time adjustment of the imaging pulse sequence. It was first proposed by [67] and [68] more than 20 years ago.

With PMC is possible to maintain data consistency during scanning [61]. The theory behind it is conceptually simple, the difficulties of this technique usually lie in the practical implementation. A complete theoretical description of PMC can be found in the following reference works [69–72]. As summarized in the review work of Maclaren et al. [73], the main result is the following: a point of the imaged sample undergoes an affine transformation:

$$\mathbf{x}'(t) = \mathbf{A}(t)\mathbf{x} + \mathbf{t}(t) \tag{63}$$

where $\mathbf{A}(t)$, a time-varying linear transformation with 9 degrees of freedom which includes: rotation, scaling and shearing. While $\mathbf{t}(t)$ represents the time-varying translation vector with 3 degrees of freedom. Thus, the total number of degrees of freedom is 12. In order to compensate for the sample's translation $\mathbf{t}(t)$, a changing RF transmit and receive phase is applied. However, for the compensation of the transformation $\mathbf{A}(t)$, the gradient waveform has to be transformed as:

$$\mathbf{g}'(t) = \mathbf{A}(t)\mathbf{g}(t) \tag{64}$$

this indicates that the gradient waveform must be transformed by $\mathbf{A}(t)$ with the linear operations of rotation, scaling and shearing. Considering that for brain imaging, it is possible to assume the brain as a rigid object, the equation 64 can be simplified as:

$$\mathbf{g}'(t) = \mathbf{R}(t)\mathbf{g}(t) \tag{65}$$

where scaling and shearing are excluded, and only translations and rotations are taken into account. This also reduces the degrees of freedom from 12 to 6, three for rotations and three for translations, respectively. $\mathbf{R}(t)$ is the rotation matrix that represents the rotation of the image object over time. In this manner, to correct for

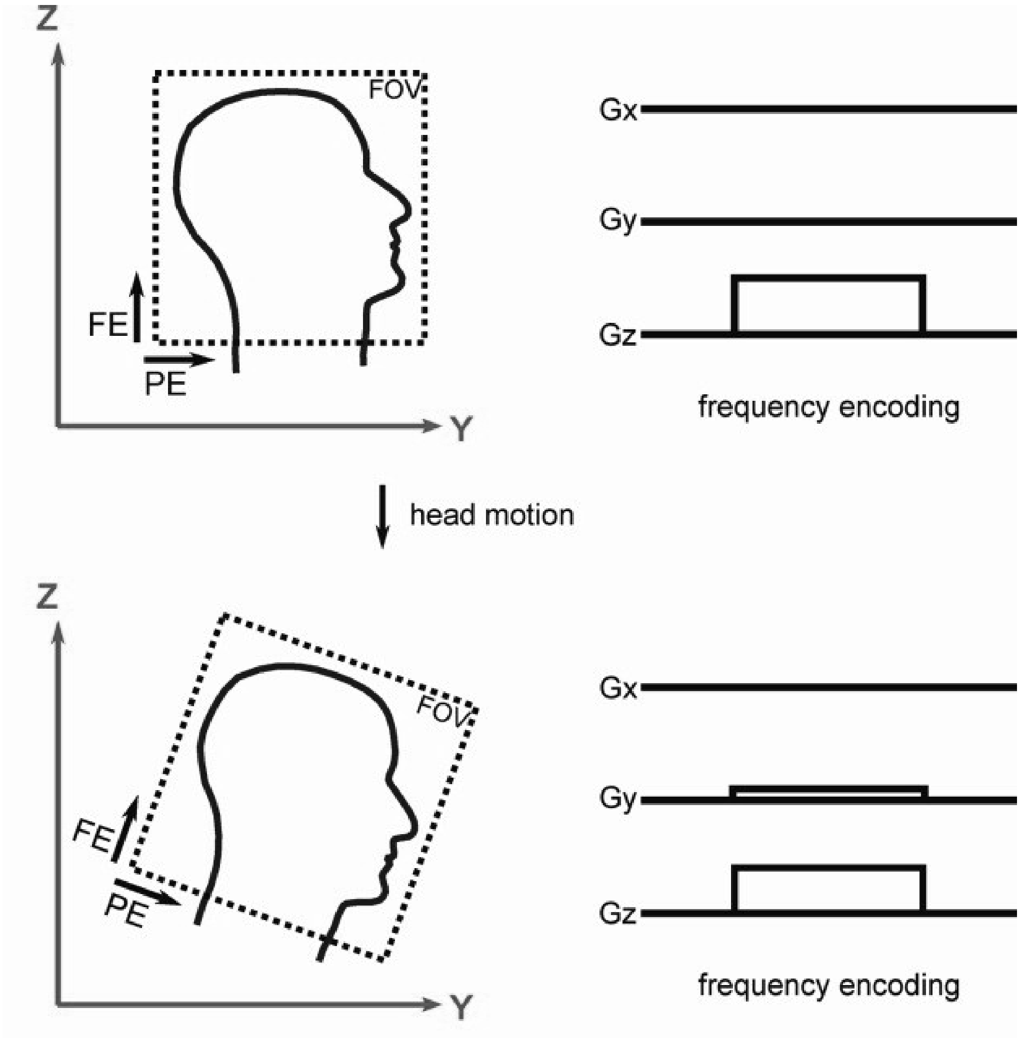

Figure 9: FoV adjustment using PMC. Gradient directions are adjusted following a rotation to ensure that every voxel in the sample encounters the same field as it would have in the absence of the rotation. [Taken from, with license, [73]]

rotations, a proper combination of the x,y and z gradients will allow to compensate for such transformation, see figure 9.

The working principle of the PMC system in the case of brain imaging is as follows: a tracking system continuously keeps track of the positioning and orientation of the subject's head, considered a rigid body; this information is then transferred to the scanner control; in this way, the sequences are updated in real-time, and, the images obtained are not corrupted by motion artefacts, see Figure 10.
The tracking data can be obtained in different ways: k-space or image-space navigators, markerless optical head tracking and camera systems, etc.. All these tracking

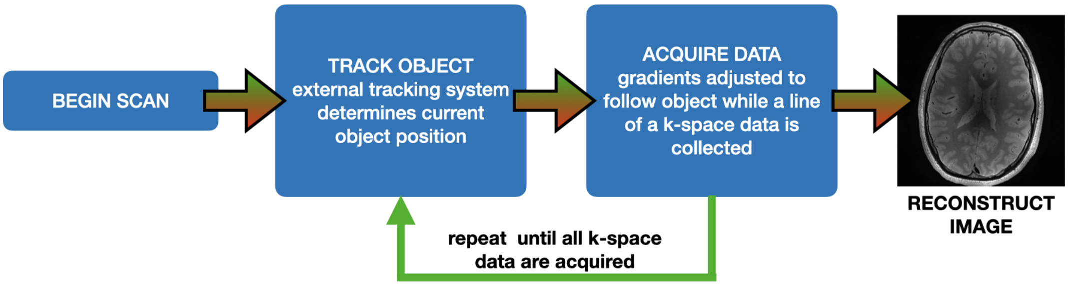

Figure 10: Working principle of PMC

modalities differ in terms of accuracy and precision [73–78]. Furthermore, there are other parameters to consider, such as patient interaction and sequence independence. For instance, in the case of an optical tracking system, such as in this thesis, there are minimal or no modifications of the pulse sequences, on the other hand, there is a direct interaction for the subjects who have been asked to use a mouthpiece. While if we consider k-space or image-space navigators, there is no interaction at all for the subjects, and conversely the pulse sequences have to be modified in order to include the tracking of the head motion.

2.3 OPTICAL MOTION TRACKING SYSTEM

The OMTS utilized in this thesis work relies on the detection of the 3D position (X, Y, Z) and orientation (Pitch, Yaw, Roll) of a Moiré Phase Tracking (MPT) marker (Metria Innovation Inc., Milwaukee, WI, USA). The in-bore optical MR compatible camera (MT384i, Metria Innovation Inc., Milwaukee, WI, USA) acquires 80 frames/s following the head motion through the Moiré phase patterns generated by the MPT marker, figure 12. Such MPT marker is rigidly coupled with the subject's head through a mouthpiece that was tailor-made for each subject [79], figures 11 and 12. Using a personalized mouthpiece not only allows a rigid coupling but is also useful to prevent pseudo-motion. The optical camera tracks in real-time the MPT marker with a precision of 0.01 mm and $0.01°$, for translations (x, y, z) and rotations (α, β, γ, corresponding to Pitch, Yaw and Roll), respectively [80]. An example of tracking data stored usually in log files is shown in Figure 13, these

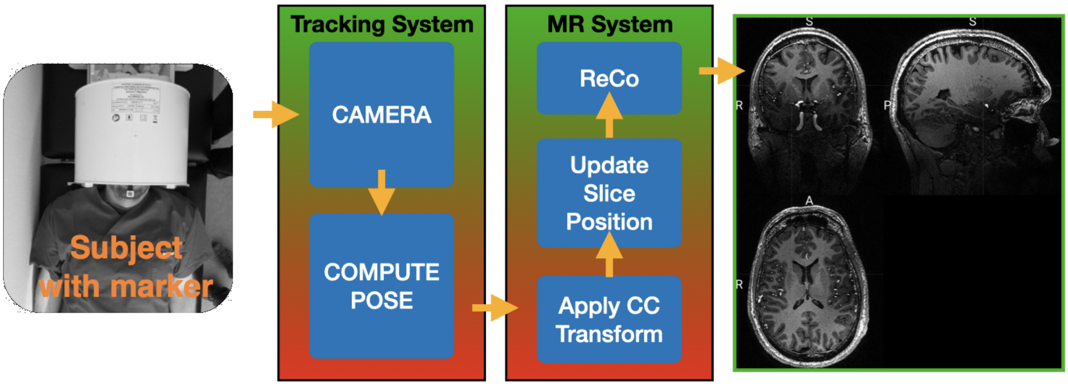

Figure 11: PMC workflow.

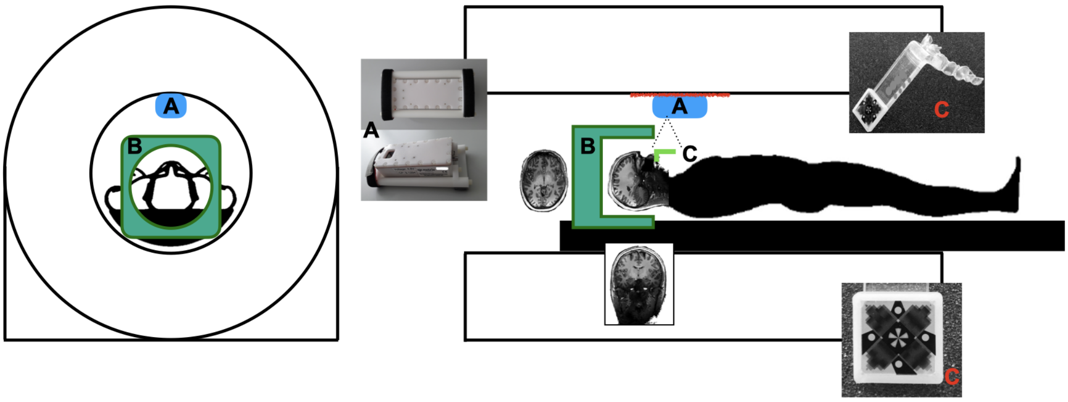

Figure 12: The camera (A) has two Velcro straps. Additional Velcro straps are permanently glued to the bore of the scanner (red line), enabling the mounting and unmounting of the camera when necessary. The green square (B) represents the head coil, (C) Mouthpiece and Moiré Phase Tracking (MPT) marker.

data are converted in terms of positioning and orientation (POSE) and sent to the scanner control PC in order to update the gradients and follow the movements of the head.

2.4 CROSS-CALIBRATION

For proper use of PMC, a so-called "cross-calibration" operation was performed between the OMTS and the scanner coordinates before starting with a session of measurements. The cross-calibration is a mandatory step to perform when using an external OMTS because only a well-calibrated tracking system guarantees minimal systematic error. In general, the cross-calibration can be performed in different ways, i.e. using image registration, it can be iterative or non-iterative, etc.. For this work, the iterative approach has been utilised. A rigid body model is considered to transform the tracking data to the scanner coordinate system and obtain the affine

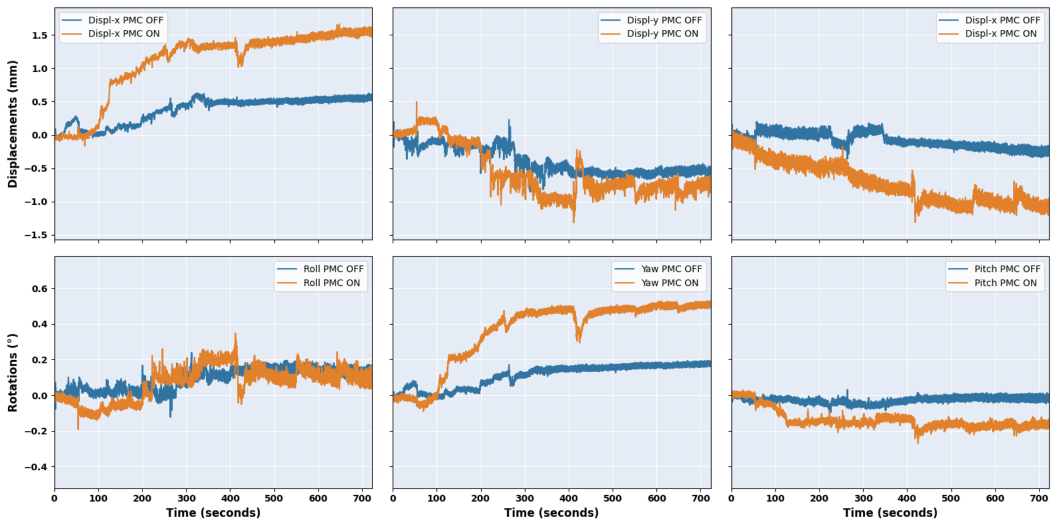

Figure 13: Motion patterns. Top row: displacements or translations for the x,y and z directions. Bottom row: Roll, Yaw and Pitch. Every plot shows two tracking curves, one for PMC OFF (blue line) and one for PMC ON (orange line), respectively.

transformation matrix. The transformation matrix is obtained after an iterative calibration procedure [75, 81] and also based on the work of Kadashevich et al. [82], that is as follows:

- first step: a 3D acquisition of the phantom designed for PMC allows an estimation of the coordinate transformation. In practice having measurements from the acquired MR images of the same objects in two coordinate frames is it possible to estimate the coordinate transformation similarly to the procedure described by Tremblay et al. [83];
- second and next steps: the phantom is rotated 180° and scanned again, after every step, the coordinate transformation is iteratively refined in order to minimise the residual errors.

The number of iterations can vary, and the procedure stops when the values fall below the desired threshold. It is also important to mention that all the inaccuracies in the tracking data, such as noise and drift or distortions in the MR images, i.e., field distortions, fat-water shift, etc., requires further nonlinear corrections [82]. Kadashevich et al. [82] developed a robust procedure to automatically select motion for cross-calibration.

2.5 MR PULSE SEQUENCES

As mentioned in section 1.4 the MR pulse sequence is a series of events comprising RF pulses, gradient waveforms, and data acquisition. With the pulse sequence is possible to manipulate the magnetisation and acquire the desired signal simply by altering the sequence parameters, such as Repetition Time (TR), TE, Inversion Time (TI), FA, matrix size, FoV, slice thickness, etc.. Every imaging sequence is characterised by means of exciting and localising an MR signal. In practice, RF pulses and gradients are always present. Typically, an MR imaging sequence consists of several repetitions of a basic pulse sequence module with defined parameters (TR, TE, etc.) until all data for a complete dataset are collected. It is possible to divide the MR pulse sequences into two main families: Spin echo and Gradient echo-based acquisitions [84–86]. For the scans performed in this thesis, the following MR pulse sequences were used:

- Gradient Echo, Gradient Echo (GE);
- Magnetization-Prepared Rapid Gradient Echo, MP-RAGE;
- Turbo Spin Echo, Turbo Spin Echo (TSE).

All the sequences were already ready-to-use and properly modified to include PMC functionalities. However, the sequences were optimised to acquire images with the desired resolution and contrast.

Gradient Echo

A basic GE sequence is a progressive saturation sequence on longitudinal magnetisation M_z, in this manner, a so-called "steady-state" will be obtained after several RF excitations. Considering the condition where the TR is much greater than T_2, due to the long TR, the transverse magnetisation M_{xy} completely decays before each new RF excitation, but at the same time the TR is usually shorter than or on the order of T_1 and this will lead to have a non-full recovery of M_z (with initial amplitude M_0). Instead, a new longitudinal equilibrium magnetization M_{SS} (steady state) is reached after several repetitions [45]. The value of M_{SS} can be calculated using the Ernst equation 66 [87]:

$$M_{SS} = \frac{1 - e^{-TR/T_1}}{1 - e^{-TR/T1} \cos\alpha} \tag{66}$$

From the equation 66, it is evident that a basic gradient echo sequence will provide an image T_1-weighted and the relative signal intensity is strictly dependent on the rotation TR/T_1 and the FA (α). However, considering the general equation 67 for GE sequences:

$$S_{GE} \propto \frac{\sin\alpha \cdot (1 - e^{-TR/T_1}) \cdot e^{TE/T_2^*}}{1 - e^{-TR/T_1} \cos\alpha} \tag{67}$$

the time decay of the signal S_{GE} is therefore determined by T_2^*. A different weighting contrast can be obtained by adjusting the sequence parameters FA, TE and TR. Table 4 shows the basic rules to have the desired contrast, a GE sequence can provide proton density (PD), T_2^* or T_1 contrast, and also T_2. An example showing T_2^*-weighted MR images acquired at 7T with a GE based sequence is reported in figure 15. For a basic GE sequence, the image-formation principle is based on the

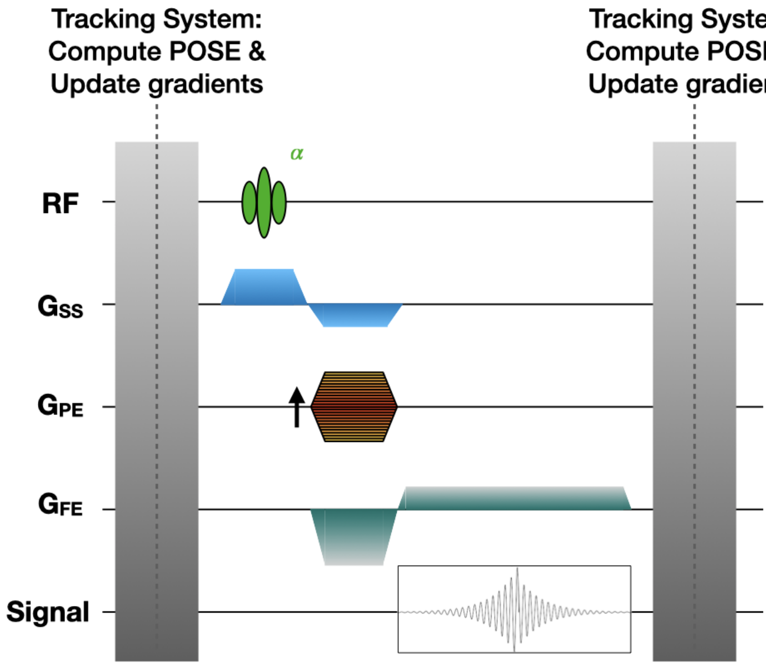

Figure 14: Gradient echo pulse sequence diagram.

Contrast	FA	TR	TE
PD weighted	Small	Long	Short
T_1 weighted	Large	Short	Short
T_2^* weighted	Small	Long	Long

Table 4: Gradient Echo sequence parameters adjustment.

concept of dephasing and rephasing the MR signal using the imaging gradients. Furthermore, GE sequences are affected by the effects of magnet inhomogeneities and local susceptibility changes because there are no compensations applied for these distortions. However, there can be applied cancellation effects for water and fat signals particularly important for GE sequences. In particular, for this thesis work, the GE sequence named Fast Low Angle Shot (FLASH) has been used [88] to acquire T_2^*-weighted images. The transverse relaxation time constant T_2^*, usually much smaller than T_2 is:

$$\frac{1}{T_2^*} = \frac{1}{T_2} + \frac{1}{T_{inhom}} = \frac{1}{T_2} + \gamma \Delta B_0 \tag{68}$$

where γ is the gyromagnetic ratio (see section 1.3) and ΔB_0 represents the distortion effects due to the local susceptibility changes mentioned previously. For a more detailed description of GE sequences, refer to the following textbooks [32, 41, 86].

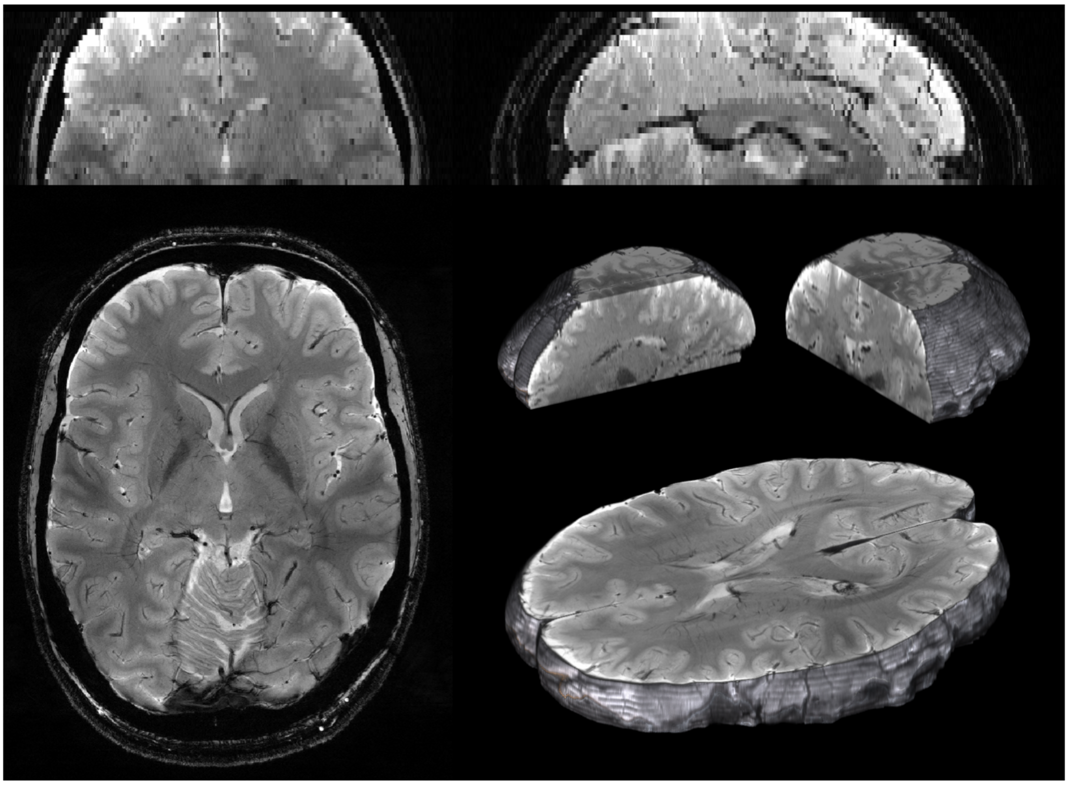

Figure 15: T_2^*-weighted 2D gradient images.

Magnetisation-Prepared RApid Gradient Echo, MP-RAGE

The second MR pulse sequence chosen was a 3D MP-RAGE generically called MP-RAGE or Turbo-FLASH for the Siemens scanner. It is one of the most common strategies to obtain T_1 weighted images with a short TR and very low FA. Usually, a short TR and a low FA lead to a very poor T_1 weighting. To obtain the desired T_1 contrast, the MP-RAGE sequence makes use of a magnetisation preparation, such as the inversion pulse, followed by a series of GE pulse sequences. The short TR is an advantage because the k-space lines are acquired closer in time, in this manner, there is a reduction of the blurriness introduced by the signal modulation of the inversion recovery curve [89–91]. In figure 16 it is shown the pulse sequence diagram for a 3D MP-RAGE sequence. With this type of sequence is possible to acquire very high-resolution T_1-weighted images that show very accurate anatomical details, especially in the case of neuro-imaging scans. It is characterised by being fast, and the Acquisition Time (TA) can be calculated as follow:

$$TA = NSA \times N_{PE} \times (N_{slices} \cdot TR + TI + TD) \tag{69}$$

with NSA the number of signal acquisitions, N_{PE} the size of the phase-encode matrix, TI N_{slices} number of slices,TR the already mentioned repetition time, the inversion time TI and the time delay (TD) as shown in the sequence diagram,

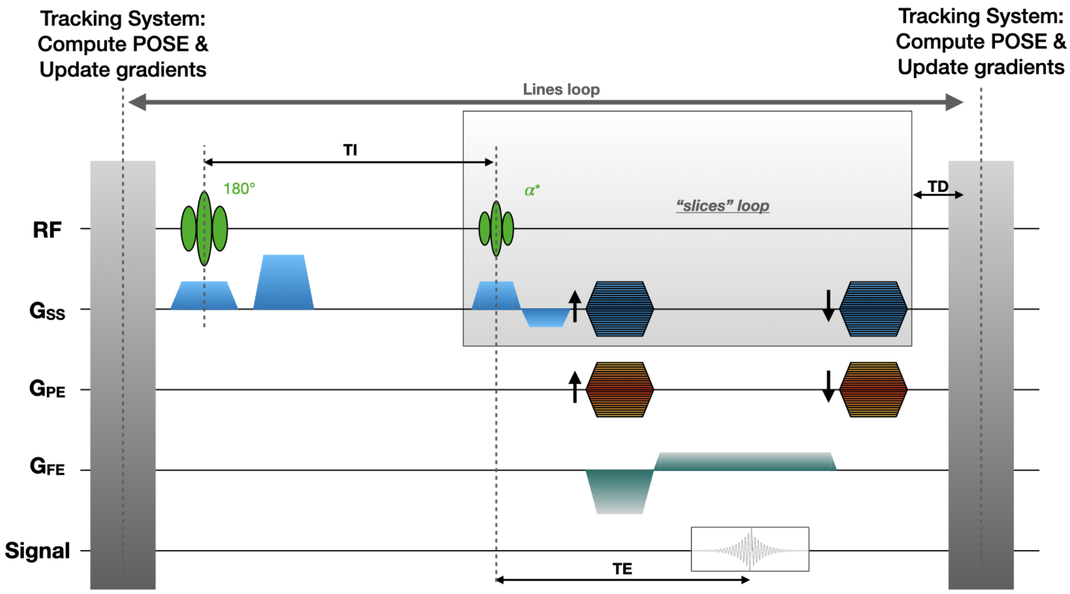

Figure 16: 3D MP-RAGE pulse sequence diagram.

figure 16. In figure 17, it is shown an acquisition of T1-weighted images acquired at 7T making use of a 3D MP-RAGE sequence. Once again, refer to the following

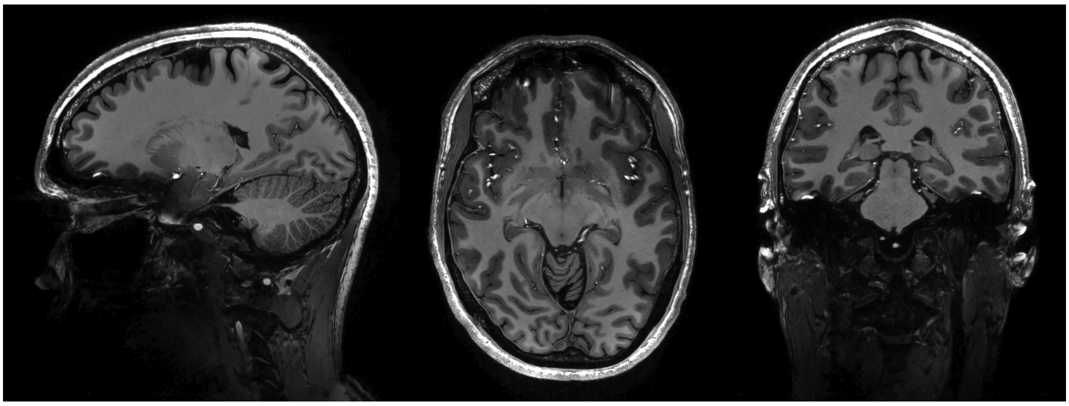

Figure 17: Multi-planar high-resolution 3D T1-weighted MP-RAGE images acquired at 7T. From left to right: sagittal, axial and coronal orientation.

textbooks [32, 41, 86], for a thorough and detailed description.

Turbo Spin Echo, TSE

The third and last MR pulse sequence used in this work has been the TSE sequence. It is a Spin Echo (SE) based sequence adapted to reduce the TA. Often, the TSE sequence has replaced the original SE technique due to its improved imaging speed. Considering a basic SE sequence, there is a single echo measured during each

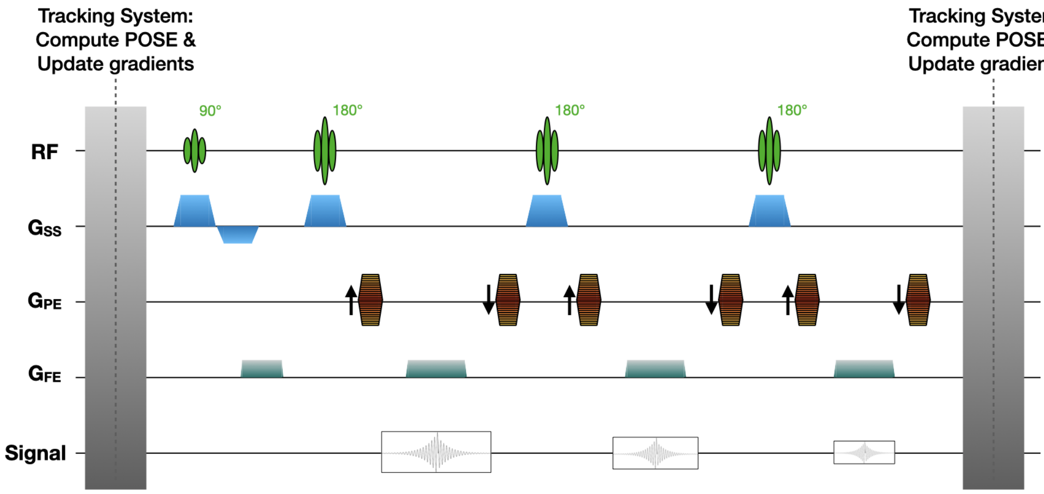

Figure 18: Turbo Spin Echo pulse sequence diagram.

TR. While the main characteristic of a TSE sequence is the capability to acquire multiple echoes per TR, after each 90° excitation pulse. To acquire the multiple echoes, a series of 180° inversion pulses are transmitted, and after each one, there is an echo acquisition, as shown in figure 18. In this manner, multiple lines of the k-space can be encoded after a single 90° excitation pulse. The number of echoes acquired per cycle is known as the Echo Train Length (ETL), in figure 18 there is shown a TSE sequence with an ETL of three. TSE sequences are also advantageous when acquiring with a rectangular FoV, and obviously, the phase encoding direction corresponds to the smallest matrix size dimension. Another benefit of using TSE sequence is the correction of external magnetic field inhomogeneity by the 180° inversion pulses. However, there are a few disadvantages to consider. First of all, there is a non-specific T_2 image weighting, this is due to the fact that the T_2 weighting of an image is dependent on the TE and by its definition, that is, the time interval between the excitation pulse and the peak echo. Considering the multiple echoes, there is a clear variation of the TE. This effect becomes more evident as the ETL increases. It also has to be considered that the effective TE depends on how the TSE echoes are used to fill the k-space. Another important disadvantage is the reduced Signal-to-Noise Ratio (SNR), in practice, the echo amplitude decreases as a function of time from the excitation pulse. Furthermore, when scanning with TSE sequences, the number of interleaved slices is less than in other sequences. A more detailed description and specifications about TSE sequences can be found in the following articles and textbooks [32, 84–86, 92–94].

3 DEEP LEARNING BASED MOTION DETECTION AND CORRECTION

3.1 INTRODUCTION TO DEEP LEARNING FOR MEDICAL IMAGING

The term "deep learning" refers to a subset of "machine learning", a branch of artificial intelligence and computer science [95]. Machine learning focuses on the use of data and algorithms to imitate the way that human beings learn [96]. Arthur Samuel is credited for coining the term machine learning in 1959 [97], but only over the last couple of decades, it has been possible to observe the massive development and use of the machine and deep learning applications. The main branches in terms of the learning paradigms of machine learning are:

- supervised: there are labelled data available for learning the function that maps feature vectors in the input to the labelled data in output [98];
- semi-supervised (or weak supervision): there are only a limited amount of labelled data, or the data are noisy. This method is used for the same applications of supervised learning [99];
- unsupervised: there is no labelled data available. In this case, the "machine" creates a representation of the input data and learns patterns and structures from unlabelled data [100, 101].
- reinforcement learning: it discovers through trial and error which actions yield the greatest rewards [102, 103].

Although the terms machine and deep learning are sometimes used interchangeably, it is to be noted that deep learning is a subset of machine learning. However, in this deep learning era, the tag "Machine Learning" (can also be referred to as classical machine learning) is given to non-deep learning-based machine learning algorithms. There are several key differences between them. Classical machine learning models are trained to perform tasks making use of manually extracted features from the raw data while deep learning models learn useful representations and features automatically from the raw data allowing them to skip completely the features extraction step.

Other important differences are reported in table 5.

The development of AI methods had and have a huge impact on medical imaging technology, medical data analysis, medical diagnostics and more in general on healthcare. The possibilities to use AI methods in healthcare are numerous, below, a short list of the main applications:

- data acquisition and image reconstruction [104–106];

Classical Machine learning	Deep learning
Models can use a small amount of data to make predictions	Requires a large amount of data
Requires a human intervention to correct and learn	Automatically extracts features and learns
Shorter training time (ranging from a few seconds to a few hours) and lower accuracy	Longer training time and higher accuracy
Makes simple, linear correlations	Makes non-linear, complex correlations
Can train on low-end machines (such as a simple personal computer with a CPU (Central Processing Unit))	Needs a specialised GPU (graphics processing unit) to train

Table 5: Machine vs Deep Learning.

- quantitative tissue parameters estimation [107, 108];
- **artefacts detection and image denoising/correction** [109–111];
- super-resolution [112, 113];
- image imputation / synthesis [114, 115];
- image registration [116, 117];
- image segmentation [118, 119];
- diagnosis and prediction [120, 121].

In this thesis, the main applications of deep learning were detection and correction of motion artefacts. The first application, the detection of motion artefacts and quantitative analysis of the degradation, falls into the classical problems of image classification and regression. Image classification refers to the problem of identifying which of a set of categories, in our case, corrupted or not corrupted by motion artefacts, an image belongs to. Instead, regression refers to the process of finding the relationships between the input image and the score associated with the output, in this case, the SSIM value as explained in section 3.3. For this work, image classification and regression constitute the basic ingredients of the image quality assessment process. Once the MR images are properly assessed is possible to move to the next stage: the deep learning based retrospective motion correction. The latter falls into the image correction or even reconstruction problem. In practice, neural networks get in input an image corrupted artificially by motion artefacts and give back an image without artefacts. For all the applications carried out, the neural networks were trained in a supervised manner.

To understand the working mechanism of the Artificial Intelligence (AI) methods employed in this thesis, one need to start with the "original" AI model - the perceptron. By stacking multiple perceptrons, an MLP is created - can be considered as a universal function approximator. These models can be trained using optimisation techniques, like, gradient descent. These are explained in the following section. Finally, the class of AI methods used for working with images, CNN, is also discussed.

3.2 Fundamentals: Perceptron, Multilayer Perceptron, Gradient Descent and Convolution

Perceptron

The simplest neural network is a perceptron, and it can be considered as an artificial neuron. McCulloch and Pitts created the perceptron in 1943 [122]. The first machine to use it was created in 1958 at Cornell Aeronautical Laboratory by Frank Rosenblatt with funding from the US Office of Naval Research [123, 124]. The perceptron was designed to be a machine rather than a programme, and while it was initially implemented as software for the IBM 704, it was later realised as the "Mark 1 perceptron" in specially manufactured hardware. This device had an array of 400 photocells that were connected at random to "neurons" in order to recognise images. Potentiometers were used to encode the weights, and electric motors were used to update the weights as the learner progressed [125].
Despite the perceptron's initial appearance as a promising technology, it was soon established that perceptrons could not be taught to recognise a wide variety of pattern classes. Because of this, neural network research was stagnant for a long time before it was realised that multilayer perceptrons, also known as feedforward neural networks with two or more layers, had higher processing speeds than single-layer perceptrons. Only linearly separable patterns can be learned by single-layer perceptrons [126]. One line will divide the data points generating the patterns in a single node for a classification task with some step activation function. Although more nodes can result in more divisions, these divisions must be merged in some way to achieve more complicated categories. Many problems that would not otherwise be solvable only require a second layer of perceptrons or even linear nodes.
A straightforward yet effective approach for the supervised learning of binary classifiers is the perceptron. An algorithm known as a binary classifier may determine if an input falls into one of two categories, such as yes/no, true/false, positive/negative, etc. Input values (Input nodes), weights and biases, net sum, and an activation function are the four essential parts of a perceptron. The characteristics or properties of the data that we want to categorise are the input values. The parameters known as weights and biases govern how much each input value contributes to the final result. The bias is a constant number that is added to the total of the weighted inputs, whereas the weights are integers that multiply with the input values. To increase the classifier's accuracy, the weights and biases can be changed as

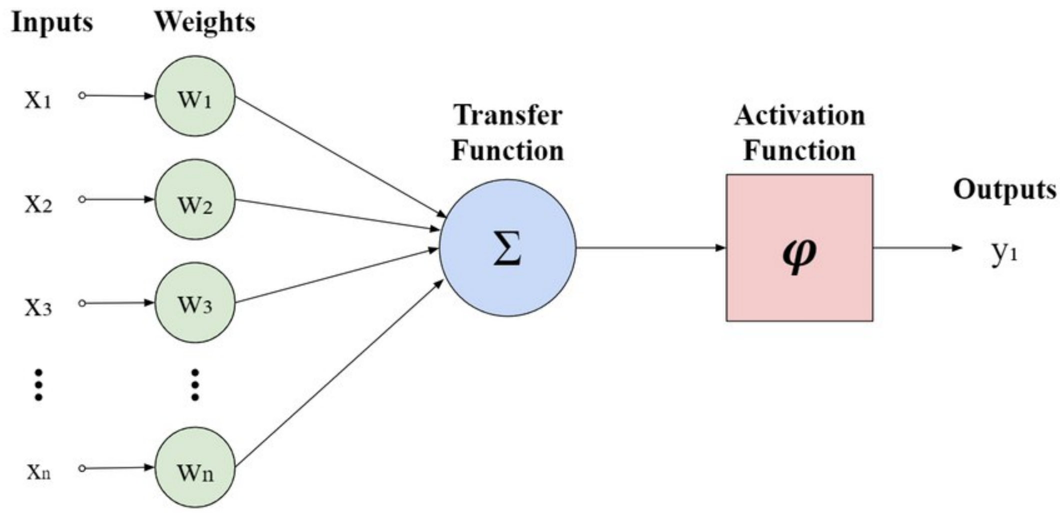

Figure 19: A Perceptron [127]

it learns. The weighted inputs plus bias are added to create the net sum. It shows how strongly, given its current parameters, the perceptron prefers one class over another.
The activation function is a rule that decides what output value (0 or 1) to assign based on the net sum. A common activation function, the so-called step function, assigns 1 if the net sum is greater than zero and 0 otherwise. To summarise, a perceptron takes an input vector $x = [x_1, x_2, ..., x_n]$ and computes an output $y = \Phi(w \cdot x + b)$ where $w = [w_1, w_2, ..., w_n]$ are weights, b is bias, $\cdot$ is the dot product, and Φ is the activation function, shown in figure-19.

Multilayer Perceptron

An artificial neural network called a MLP is made up of several layers of perceptrons [128]. A MLP uses numerous hidden layers between the input and output layers to learn more intricate and non-linear patterns than a single perceptron can. A hidden layer is a layer that conducts some intermediate calculation but does not immediately interact with the input or output data. The number of perceptrons in each hidden layer, each with its own weights and bias, might vary.
The input data is passed through each layer of the MLP, each perceptron is activated, and the final layer produces an output vector. The MLP can then compute an error measure by comparing the output vector to the target output vector (the labels or classes). An example of an MLP is shown in figure-20. The MLP can then reduce the error by adjusting its weights and bias using a learning approach like backpropagation. Backpropagation is a method for training artificial neural networks using gradient descent, see next section 3.2. Calculating the gradient of the error function with respect to each neural network parameter is how backpropagation works.

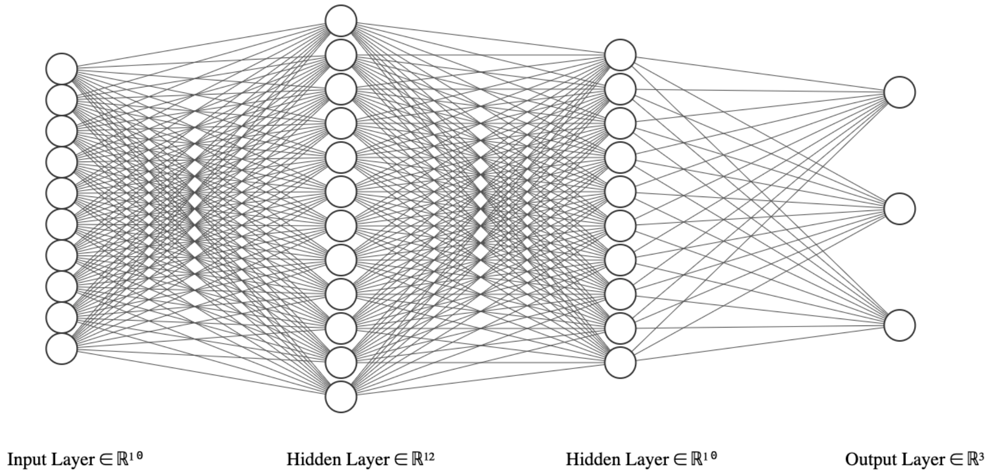

Figure 20: An example of an MLP with one input, two hidden, and an output layer.

In conclusion, an MLP is a neural network that learns complex and non-linear patterns from data using many layers of perceptrons. In order to achieve this, data is passed through each layer, activation functions are used, errors are calculated, and parameters are updated.

Gradient Descent

An optimisation technique called gradient descent locates the local minimum of a differentiable function. A function that has a clearly defined derivative at each point is said to be differentiable. Every place where the function value is lower than any neighbouring points is considered to be a local minimum.
By repeatedly moving in the opposite direction of the function's gradient at the current position, gradient descent works. The function's direction of the sharpest growth is indicated by the gradient, which is a vector. The function value can be decreased by moving in the gradient's opposite direction. An example of the gradient descent process is shown in figure-21.
Two factors are needed for gradient descent: a stopping criterion and a learning rate. The size of each step depends on the rate of learning. Gradient descent converges slowly with a small learning rate, but it can diverge or overshoot with a high learning rate. The stopping criterion determines when gradient descent should be stopped, such as when the change in function value is minimal or when a predetermined maximum number of iterations has been reached.
By minimising an error or cost function, gradient descent is frequently used to train neural networks and machine learning models. Indicated by the cost function is how well the model fits the data. Using gradient descent, it can be enhanced the model's precision by changing the model's parameters [129].

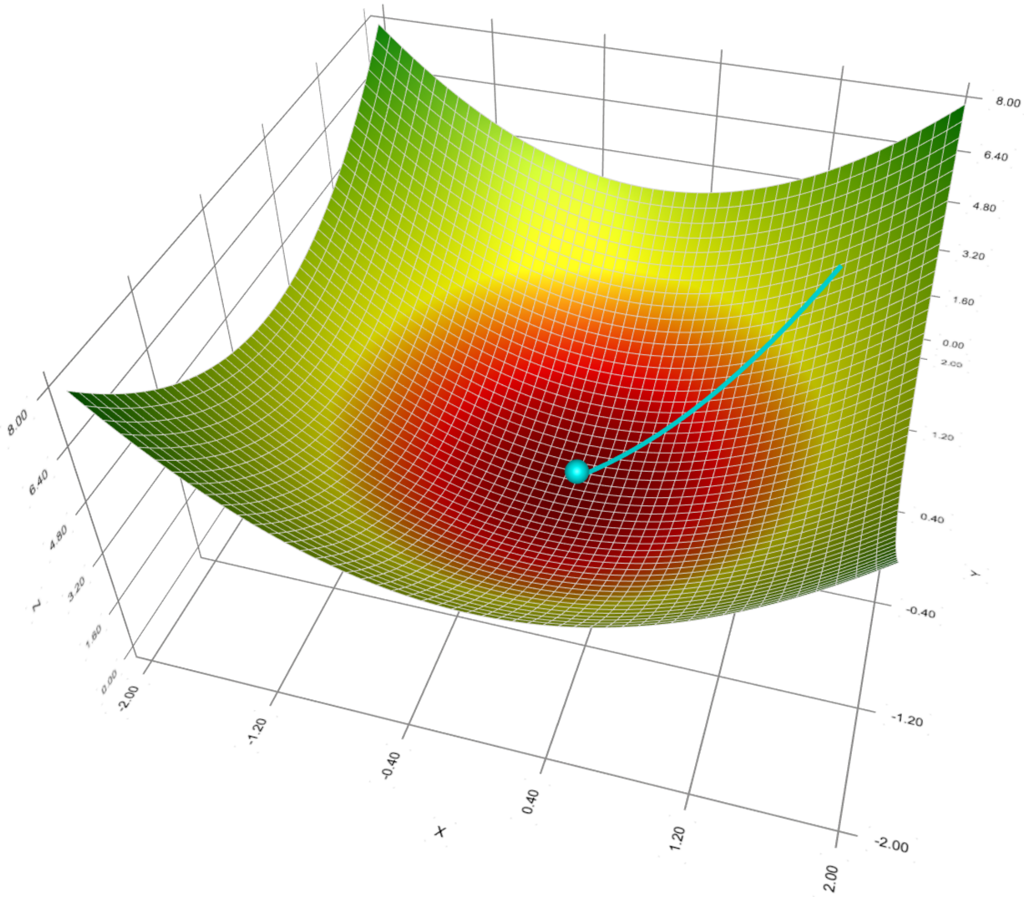

Figure 21: An example of the gradient descent process that demonstrates movement on the loss plane.

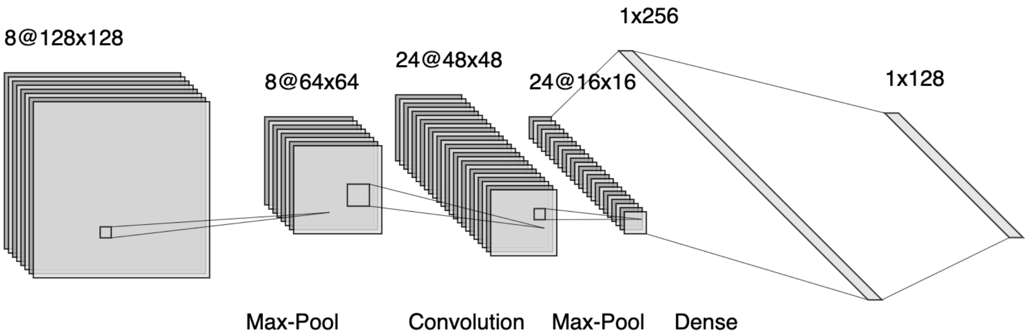

Figure 22: An example of a CNN with two max pool layers separated by a convolution layer, followed by a fully-connected (dense) layer.

Convolution

CNNs, a subset of Deep Neural Network (DNN)s that can evaluate visual information, use a unique approach called convolution [130]. CNNs can extract features from images and learn from them thanks to convolution [131]. Convolution is the straightforward process of applying a filter to an input to produce an activation. An edge, a corner, or a colour are examples of patterns or features that are defined by a filter, which is a small matrix of numbers. Another matrix of numbers that represents an image or a portion of an image serves as an input. The amount by which the filter matches the input at a specific point is expressed as a single value known as an activation.
Convolution is achieved by sliding the filter across the input and multiplying each filter element by the matching input element. The activation value is then obtained by adding up all of these products. We repeat this procedure for each and every conceivable site of the filter on the input to produce a feature map, which is a map of activations. The feature map displays the location and the degree of feature detection made by the filter on the input. Convolution decreases the dimensionality of images and extracts useful features, assisting CNNs in learning from them. It is possible to obtain different feature maps that emphasise certain features of an image by applying various filters to it. For instance, different filters may be used to identify colours, vertical edges, and horizontal edges. This allows for building more intricate and abstract features that reflect more complicated ideas like forms, objects, or faces by stacking numerous layers of convolution with various filters. An example schematic is shown in figure 22.

3.3 IMAGE CLASSIFICATION AND REGRESSION

IQA is a fundamental step to evaluate MR images [132–135]. The main purpose of this process is to find out if the quality can guarantee images are diagnostically reliable and exempted from artefacts, in such a way as to avoid unreliable diagnosis [136, 137]. Often the evaluation process requires time and is subjectively dependent upon the observer in charge of carrying it out [138]. Furthermore, different levels of expertise and experience of the readers (experts designated to perform the IQA) could lead to a non-perfect matching assessment. Another intrinsic issue of the IQA for MR images is the absence of a reference image. No-Reference IQA techniques with and without the support of machine and deep learning support have been proposed in the last years for the evaluation of the visual image quality [134, 136, 139–146]. These techniques are able to detect and quantify the level of blurriness or corruption with different levels of accuracy and precision. However, there are many factors to take into consideration when choosing which technique to apply, the most important are reported in table 5, and in addition to that is important also to consider the **hyperparameter tuning**, deep learning can be tuned in various different ways and it is not always possible to find the best parameters, while machine learning offers limited tuning capabilities [95, 147, 148]. Furthermore, it is always important to keep in mind that using machine learning there is a fundamental step of feature extraction. It is not obvious that the selected feature is the best one to solve the problem, and for this reason, it is preferable to use a deep learning approach where the feature extraction is automatically done by the artificial neural network. Although the list of machine and deep learning techniques used for regression and classification tasks are constantly being updated [149–152], there is still missing an objective gold standard IQA tool for MR images [133]. The aim of this work is to provide an automated IQA tool able to detect the presence of motion artefacts and quantify the level of corruption or distortion compared to the ground truth image, based on the regression of the SSIM [153]. This tool has been designed to be able to work for a large variety of MR image contrast, such as T_1, T_2, T_2^*, PD and Flair weighted images and independently from the resolution and orientation (axial, sagittal or coronal) of the considered image. Additionally, it has been introduced a contrast augmentation step in order to increase the range of variability of the weighting, for instance, a T_1-weighted image can present a different weighting, showing a more or less pronounced contrast between Grey Matter (GM), White Matter (WM) and Cerebrospinal fluid (CSF). As mentioned above, there is no reference image for the IQA, but for the SSIM calculation, it is always necessary to have two images (corrupted vs motion-free artefacts image), for this reason, in our work the corrupted images were artificially created, making use of two different algorithms, one implemented by Shaw et al. [154] (package of the library TorchIO [155]) and a second algorithm developed in-house [110]. Furthermore, when training a neural network model in a fully-supervised manner, as in this case, it is required to access a large amount of labelled or annotated data [156]. For regression, it is necessary to have the target value, in our case, this is represented by the SSIM value.

The artificial neural networks trained for the classification and regression tasks were ResNet-18 and ResNet-101, two variants of ResNet [157], a novel architecture called Residual Network, launched by Microsoft Research experts in 2015. The main difference between them is the number of layers, details for both models can be found in appendix 7.2. Since the start of the deep learning age, every consecutive winning architecture used more layers in a DNN [130] to lower the error rate, in particular, after the first CNN-based architecture (AlexNet [130]) that won the ImageNet 2012 competition [1]. This is effective for smaller numbers of layers, but when there are more layers, a typical deep learning issue is known as the vanishing/exploding gradient arises [95, 158–160]. This results in the gradient becoming zero or overly large. Hence, the training and test error rate similarly increases as the number of layers is increased.

This architecture introduced the idea of **Residual Blocks** to address the vanishing/-exploding gradient issue, applying a method known as **skip connections**. The skip connection bypasses some levels in between to link layer activations to subsequent layers, creating a leftover block. These leftover blocks are stacked together to create ResNet. The strategy behind ResNet is to let the network fit the residual mapping rather than have layers learn the underlying mapping. Instead, for a deep neural network, the layers gradually learn more complex features, i.e., the first layer learns edges, the second layer learns shapes, the third one objects, and so on. He et al. [157] analysing the training and test error of two CNNs, one with 20 layers and one with 56 layers, found that the error of the 56-layer CNN is higher than the 20-layer one. The vanishing/exploding gradient problem, the setup of the network, or the optimisation function could all be to fault for the 56-layer CNN's failure. The authors contend that the use of Batch Normalisation [95] assures that the gradients have normal norms, despite the fact that disappearing gradients are particularly simple to blame for this. There are several ideas explaining why Deeper Networks don't outperform their Shallow counterparts, but sometimes it is preferable to start with empirical findings and work backwards from there. With the addition of the above-mentioned residual Block, the difficulty of training extremely deep networks has been reduced.

The most important characteristic of ResNet is shown in figure 23. As already explained, the "Skip Connection" identity mapping is the key factor of such a model. The sole purpose of this identity mapping, which has no parameters, is to add the output from the layer below to the layer above. With x indicating the inputs, $\mathcal{F}(x)$ the residual mapping function, relu the rectified linear unit activation function [95]. However, x and $\mathcal{F}(x)$ may not have the same dimension. This is due to the fact that convolution operation shrinks the spatial resolution of an image, and for this rea-

1 "ImageNet Large Scale Visual Recognition Competition 2012 (ILSVRC2012)". https://image-net.org/challenges/LSVRC/2012/results.html

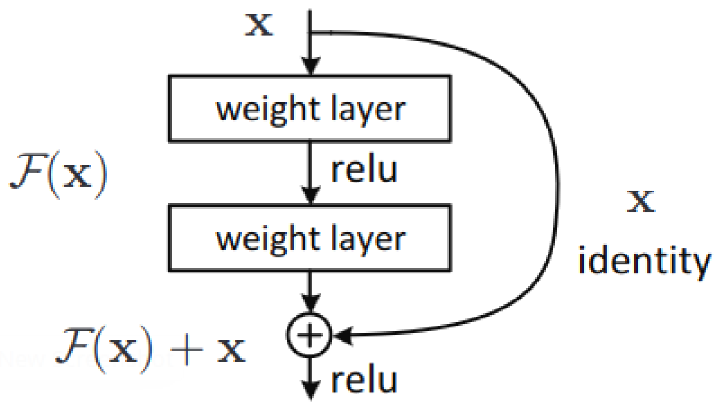

Figure 23: A building block of ResNet from the original paper [157]

son, the identity mapping is multiplied by a linear projection W_s to expand the channels of shortcut in order to match the residual [161]:

$$y = \mathcal{F}(x, \{W_i\}) + W_s x \tag{70}$$

W_i indicates the weight matrix of the i-th connection. The benefit of including the skip connection is that regularisation will bypass any layer that degrades architecture performance. As a result, training an extremely deep neural network is possible without encountering issues with vanishing or expanding gradients.
Similar techniques exist under the name "highway networks", which also employ skip connections. These skip connections also make use of parametric gates, just as Long Short-Term Memory (LSTM) [162]. The amount of data that flows across the skip connection is controlled by these gates. Yet, this design has not offered accuracy that is superior to ResNet architecture.

3.4 Deep Learning Based Retrospective Motion Correction

For limiting the presence of motion artefacts or completely removing them without the need for further data acquisition, several deep learning models have been implemented [109, 110, 163–165]. Basically, a motion-corrupted image is used as the training input, and a motion-clean image is used as the label, and this is how motion correction often works in the image domain. Most investigations limit their goal to a particular motion type because the shape of the motion artefact depends on the kind of motion, see section 1.5. Motion correction has also been done using U-Net architecture, which has proven effective for a variety of medical imaging workloads [166]. The U-Net was utilised by Lee et al. [167] to lessen the ghosting effects brought on by respiratory movements. Here, 1D-real Navigator's data compensation was employed as a label and data augmentation was used to make

up for the missing data by flipping horizontally. In this investigation, the respiratory motion artefact was minimised, but there was still some blurring. For the correction, additional CNNs have also been used. In order to expand the training data and optimise memory usage, Tamada et al. [168] suggested a multi-channel CNN-based model for motion artefact reduction utilising a CNN. The residual between the simulated artefact and predicted images, as well as the residual between the simulated artefact and ground truth images were trained to be optimised. They used the CNN filter in gadoxetate disodium-enhanced arterial-phase liver MRI and showed a significant reduction in artefacts due to increased performance [169].
Although deep learning motion correction models can be used for non-rigid body motion and rigid body motion, the focus of this work is only on brain imaging. The brain has a higher prevalence of rigid motion than other parts of the body like the chest and abdomen because it is less impacted by respiration and peristalsis [54].
One of the earliest research for motion-correction reconstruction using deep learning was presented by Johnson and Drangova [59]. A DNN was used to reconstruct the motion-corrected magnitude MR image from the vector of motion-deformed k-space. This research demonstrated the capability of deep learning-based motion correction techniques. Another work that made use of a conventional U-Net model for motion correction (MoCoNet), which creates the motion-compensated image from the motion-corrupted (only 3D-MPRAGE), was proposed by Pawar et al. [170, 171]. U-Net was trained using simulated data, but the simulation patterns were only allowed to involve straightforward sudden movements. The authors also suggested a motion-simulation technique with enhanced MoCoNet [164]. A linear combination of data that had been strictly modified and distinct images were used in this strategy. When trained on this motion-simulated image, the Inception-ResNet network outperformed the entropy-minimisation technique.
Prior to the motion artefact simulation, Sommer et al. [172] used data augmentation to increase the data fluctuation. The motion-clean image was then subtracted from the motion-corrupted image by Fully Convolutional Network (FCN), which then extracted the motion artefact-only image. Also, as multi-resolution images were used for training, the network-based filtering caused less distortion in anatomical structures. Simulated data were also employed by Duffy et al. [173, 174] to train the regression CNN model that could forecast motion-free images. Although smoothing happened, coherent simulated ghosting and severe motion were better adjusted for random artefacts and mild motion. The findings of this study revealed that real motion artefacts could be removed using neural networks trained with simulated data.
A new Generative Adversarial Network (GAN) framework called MedGAN, which incorporates the novel generator model, was proposed by Armanious et al. [165, 175]. The encoder-decoder technique, which lessens blurriness and boosts the network's capacity, was used to connect three U-Net topologies in order to enhance the details of MR images. The validation was carried out using three distinct tasks, and it has shown promising results in the MR motion correction as well as in the PET-CT translation and PET denoising. The MedGAN joint, which is flexible for

both rigid and non-rigid motion, was also added to the network [163].
The methods discussed above used a Cartesian sampling approach, but different trajectories revealed distinct facets of motion artefacts. In order to demonstrate the motion artefact, Usman et al. [175] and Dou et al. [176] used a variety of radial and spiral k-space trajectories. The Cartesian sequential, Cartesian parallel, and random trajectories were all used in Usman et al. [175] application of the GAN-based architecture. The validation result for the random trajectory was the best since it was less affected by motion than the Cartesian trajectory. In order to compare the outcomes regarding the trajectory, Dou et al. [176] independently used spiral and Cartesian trajectories as inputs of the DNN model.
The aforementioned retrospective motion correction methods correct mainly in-plane motion artefacts. However, Wang et al. [177] suggested an U-Net-based model to correct out-of-plane motion artefacts that make use of motion parameters as well. As a result and in contrast to the traditional gradient-based autofocusing algorithm, the latter was applied to the loss function in order to simplify the computation, boost performance, and provide more reliable motion artefact correction.
Deep learning has been utilised for detection as well as motion correction. In motion-corrupted k-space, Bydder et al. [178] employed the CNN model to identify outliers and remove distorted k-space lines. The reconstruction was then conducted using a low-rank-based technique. This work demonstrated that k-space deformation might also be detected using deep learning. It is noteworthy to mention the work of Haskell et al. They proposed NAMER, a method that combines a CNN and a model-based approach. The motion-corrupted images and their corresponding motion-only artefacts were utilised as the input and output of CNN, and the difference between them was thought to be the initial motion-compensated image. First, they trained the CNN to recognise the motion artefacts. Afterwards, the initial motion-compensated image and the motion-corrupted image were then used to estimate the motion parameters. Ultimately, the model-based reconstruction utilising the computed motion parameters produced the motion-mitigated image. The optimum settings and image were obtained by repeating these three procedures. Integrating CNN and the model-based reconstruction technique enabled faster computation, non-linear problem efficiency, and high robust confidence in the final reconstruction. Only the CNN-based technique to get rid of the motion artefact performed better as a result of their work.

Motion Simulation

The motion-correction methods based on deep learning outlined above were trained with datasets created artificially. In practice acquiring motion-corrupted and motion-clean datasets would require lengthy scan durations, which raises the cost of gathering the training data [165]. To correct motion artefacts using deep learning, motion-simulation approaches were therefore necessary. Since most simulation-based research focus on rigid motion, the following analysis is restricted to this area.

The existing methods for simulating motion can be generally divided into two groups: image-based approaches and k-space-based approaches. Both approaches were utilised in this work. The image-based approach developed in this work follows these steps [110, 111]:

1. get the input image and create an empty (all zeros) complex array with the same dimensions;
2. apply rotations and translations to the input image;
3. transform the rotated/translated image into the Fourier space;
4. copy the first row (or column) of the transformed image and paste it into the empty complex array created in step 1;
5. repeat from step 2 to step 4 replacing sequentially the rows (or columns) of the initial empty complex array until it is completely filled;
6. transform (with the inverse Fourier transform) the filled complex array to the image space.

The steps just described refer to a 2D case, but they are also valid for the 3D case. The only difference lies in the fact that the translations are in all three directions x, y and z, and the rotations are, in this case, three and not only one, as in the two-dimensional case. Choosing a row or column is equivalent to choosing one of the possible in-plane directions (x or y) for the final artificial motion artefacts. To speed up the computational time is preferable to choose rows or columns accordingly with the smallest size.
A sample of images corrupted with this method is shown in figure 24, for this case, it is possible to control the desired level of degradation of the image by adjusting the amplitude of rotations and translations.
The python code developed for this approach can be found in appendix 7.1.

The k-space-based approach involves a direct modification of the k-space in order to reproduce real-looking like motion artefacts. Shaw et al. [179] developed an MRI k-space augmentation technique to create motion artefacts, and it is implemented as transformation (or augmentation) class of the python library TorchIO [155]. The proposed method consists of 5 steps:

1. create a model of random movement using samples from several probability distributions;
2. 'de-mean' the movement transforms that were generated;
3. use the 'de-meaned' movement model to resample the artefact-free volume;
4. create a composite k-space using the individual k-spaces of various resampled volumes;

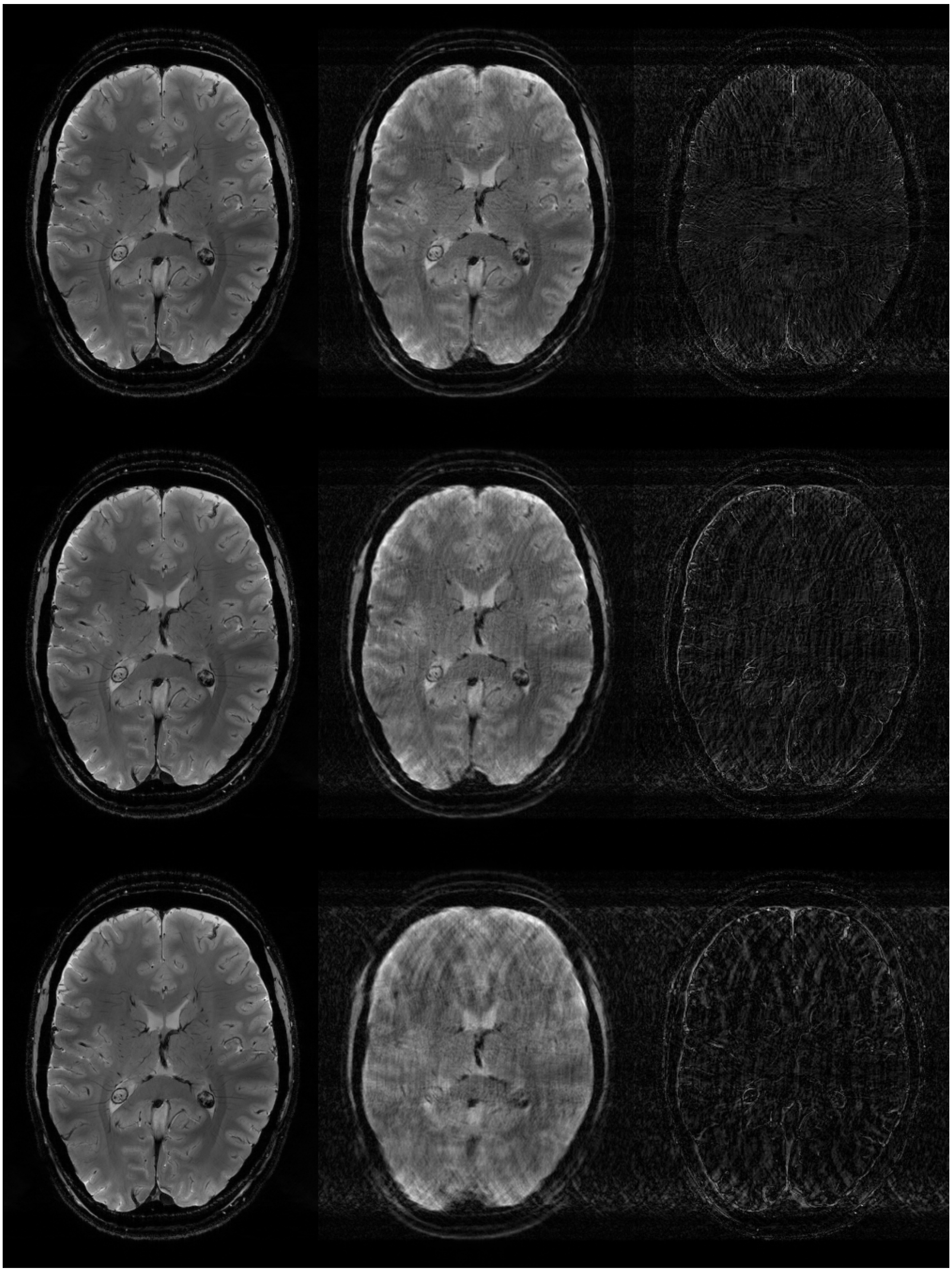

Figure 24: Image-based motion simulation. Left column: original image; central column: corrupted image; right column: the absolute difference between original and corrupted images. First row: light degradation; second row: mild degradation and third row: heavy degradation level.

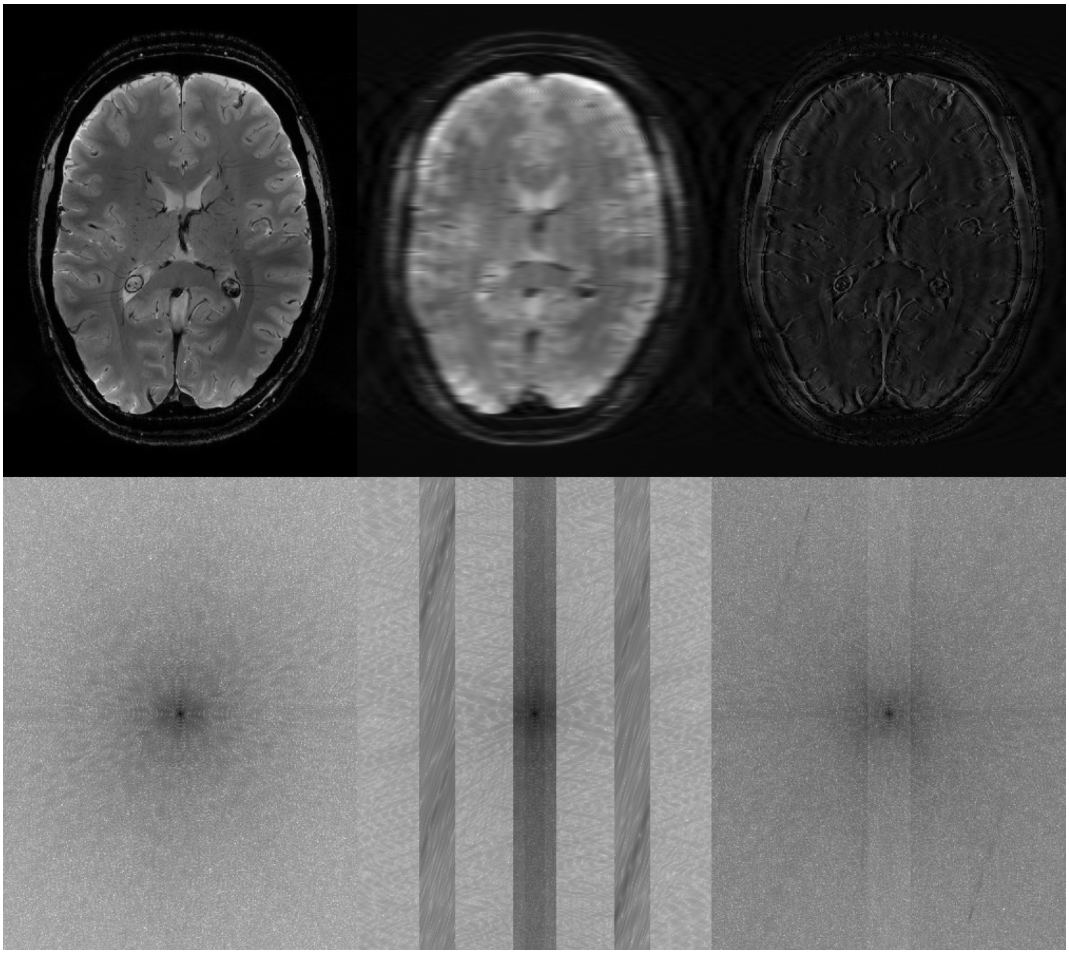

Figure 25: k-based motion simulation 1. Left column: original image; central column: corrupted image; right column: the absolute difference between original and corrupted images. First row: images in image space; second row: k-space of the upper images.

5. transform back to the image space.

A first sample of an image degraded using such a method is shown in figure 25. A few more samples are in figure 26.
Also, in this case, is possible to obtain the desired level of degradation setting different parameters such as rotations, translations, number of transforms, number of ghosting, axis for ghosting, intensity, etc.[2].

2 RandomMotion: `https://torchio.readthedocs.io/transforms/augmentation.html#torchio.transforms.RandomMotion` and RandomGhosting: `https://torchio.readthedocs.io/transforms/augmentation.html#torchio.transforms.RandomGhosting`

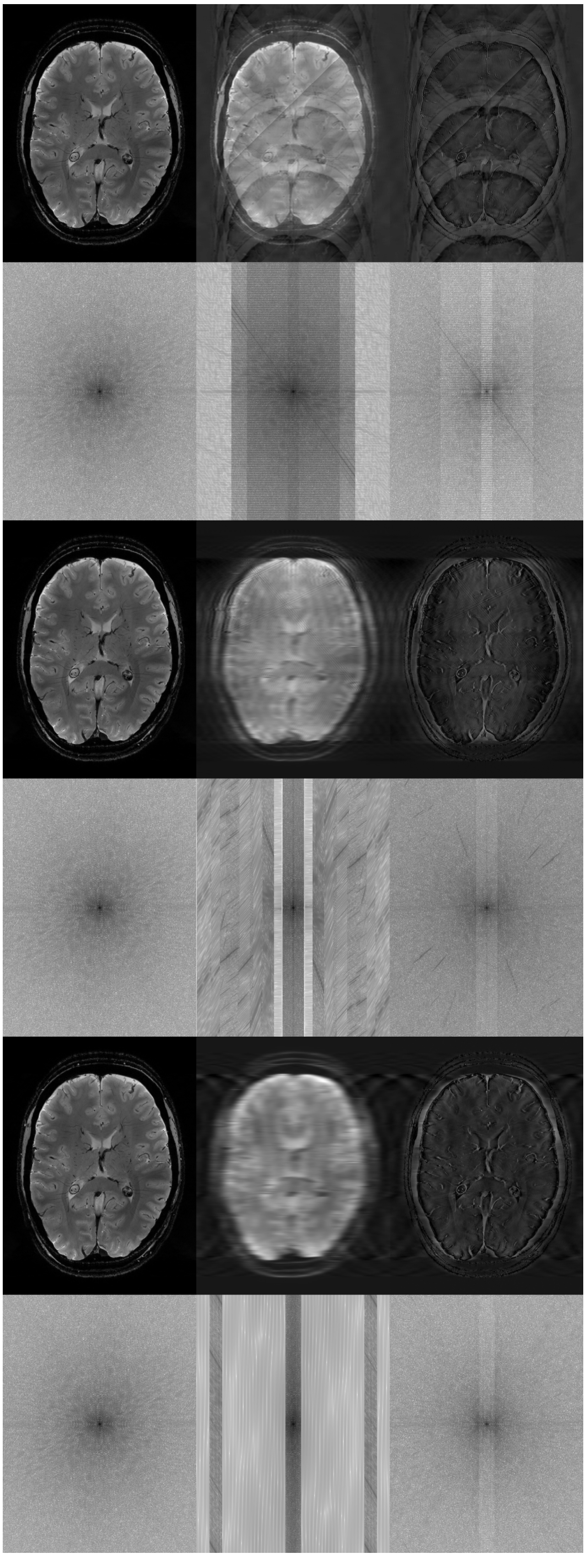

Figure 26: k-based motion simulation 2. Left column: original image; central column: corrupted image; right column: the absolute difference between original and corrupted images. First, third and fifth rows: images in image space; second, fourth and sixth rows: k-space of the upper images.

Goal of this thesis with respect to Deep Learning

As discussed in 1.6, this thesis aims to develop and employ deep learning techniques to detect and quantify motion artefacts in MRIs, followed by correcting the corrupted ones. Moreover, this thesis also develops motion simulation techniques to be able to create training datasets for the deep learning models.

Part III

STRUCTURAL IMAGING WITH PMC

4 PROSPECTIVE MOTION CORRECTION USING OMTS

4.1 EXPERIMENT DESIGN

In this chapter, the details of the experimental part concerning PMC for structural imaging are reported. The majority of the findings presented in this chapter have been published on [180]. The purpose of this study was to determine and quantify whether PMC can improve image quality at 7 T for healthy compliant subjects under the "quasi-no-motion" regime [181]. It is important to note that this study was not meant to evaluate PMC's performance in a larger group of MRI-inexperienced patients.

Twenty-one healthy volunteers were scanned over the course of two independent 75-minute long sessions (14 males, 31.5 ± 6.1 years old, and 7 females, 27.3 ± 3.4 years old). Each subject had a custom-made mouthpiece with the MPT marker attached, that was created using their dental impressions (figure 12). All subjects gave informed written consent before participating, and the procedures were authorised by the local ethics commission. A 7T whole-body MRI scanner (Siemens Healthineers, Erlangen, Germany), a 32-channel head coil (Nova Medical, Wilmington, MA, USA) and the OMTS described in section 2.3 were used to do the scanning (Metria Innovation Inc., Milwaukee, WI, USA). The entire system is shown in figure 12.

The use of personal mouthpieces makes a rigid coupling possible and stops pseudomotion as a result. All of the subjects had previously undergone 3T MRI scan, and at least 66% of them had already undergone 7T imaging. Also, four subjects had prior PMC experience. No subject has ever complained about the mouthpiece or the scanning process in any way, either during or after the scan sessions.

Velcro straps were used to mount and dismount the in-bore camera for each session (figure 12). The marker was tracked with an accuracy of 0.01 mm and 0.01° for translations (x, y, and z) and rotations (corresponding to Pitch, Yaw, and Roll), respectively [80]. The optical camera was set to acquire 80 frames per second. Once tracking information, position, and orientation had been collected from each frame (using a separate control computer), it was delivered constantly to the MRI scanner in order to update the imaging volume once per TR, just before each excitation. The tracking device was calibrated before being used on humans in accordance with the method suggested by Zaitsev et al. [75]. To assess the image quality for a stationary object, each sequence was tested on a phantom. We also assessed how mechanical vibrations caused by gradients during scanning affected the OMTS. The same sequences utilised in vivo were employed to scan a stationary phantom while enabling motion correction.

The sequences employed in these sessions were developed in an earlier PMC-based study [181]. Proton density (PD), T_2, T_1, and T_2^* contrasts were acquired during this study. Using a 2D TSE sequence, the PD and T_2 were both acquired with an in-plane resolution of 0.28x0.28 mm^2 and a slice thickness of 1.0 mm. Using a 3D-MP-RAGE sequence with an isotropic resolution of 0.45 mm^3, the T_1-weighted images were obtained. The slice thickness was kept constant at 1.5 mm while the T_2^*-weighted images were acquired using a 2D gradient-echo (FLASH) sequence with three distinct in-plane resolutions: 0.25x0.25, 0.35x0.35, and 0.5x0.5 mm^2. These images were referred as $T_2^* - w$ (025), $T_2^* - w$ (035), and $T_2^* - w$ (05). Table 6 lists all of the sequences and associated parameters that were used. The acquisition of the

Sequence	MPRAGE	TSE	TSE	GRE	GRE	GRE
Encoding	3D	2D	2D	2D	2D	2D
Contrast	T_1	T_2	PD	T_2^*	T_2^*	T_2^*
PMC	On/Off	On/Off	On/Off	On/Off	On/Off	On/Off
In-plane res. (mm)	0.45 iso†	0.28 iso†	0.28 iso†	0.5 iso†	0.35 iso†	0.25 iso†
Slice thick. (mm)	0.45	1.0	1.0	1.5	1.5	1.5
Matrix size (voxel)	496 x 496	690 x 704	690 x 704	336 x 448	480 x 640	672 x 896
Voxel vol. (mm^3)	0.091	0.078	0.078	0.375	0.184	0.094
slices	416	15	15	30	30	30
TR (ms)	2820	6000	6000	680	680	680
TE (ms)	2.82	59.0	9.9	16.6	15.1	16.6
TI (ms)	1050	-	-	-	-	-
Flip angle (deg)	5	130	130	30	30	30
Bandwidth (Hz/px)	170	473	473	60	60	60
Total ADC (ms)	5.88	2.11	2.11	16.67	16.67	16.67
TA (min:sec)	12:12	5:12	5:12	8:21	11:37	15:58
Parallel imaging	GRAPPA 2	GRAPPA 2	GRAPPA 2	GRAPPA 2	GRAPPA 2	GRAPPA 2

Table 6: Sequence parameters. †Iso is the abbreviation of isotropic [with license from [180]].

T_1, T_2, and PD scans took place during the first of two independent sessions on different dates, and the remaining T_2^* scans were acquired during the second. The application of PMC to the acquisition of sequences was performed in random order throughout each session. The subjects were given clear instructions to remain still throughout each scan. There were 252 total image volumes obtained for the cohort as a whole. Both with PMC ON and OFF, the motion-tracking data was recorded in distinct log files.

The tracking data were averaged to get the global mean and Standard Deviation (SD) for each degree of freedom for each contrast, independently for PMC OFF and ON. The following equations were used to perform the statistical analyses of rotations and displacements:

$$\begin{aligned} \Delta X &= \{x_{i+\delta t} - x_i\}_{i=1,\dots,n-1}, \quad \Delta A = \{\alpha_{i+\delta t} - \alpha_i\}_{i=1,\dots,n-1}, \\ \Delta Y &= \{y_{i+\delta t} - y_i\}_{i=1,\dots,n-1}, \quad \Delta B = \{\beta_{i+\delta t} - \beta_i\}_{i=1,\dots,n-1}, \\ \Delta Z &= \{z_{i+\delta t} - z_i\}_{i=1,\dots,n-1}, \quad \Delta \Gamma = \{\gamma_{i+\delta t} - \gamma_i\}_{i=1,\dots,n-1} \end{aligned} \tag{71}$$

where n is the number of time points in each sequence, and ΔX, ΔY, ΔZ, ΔA, ΔB and $\Delta\Gamma$ and are arrays storing the displacements and rotations finished in the time $\delta t = 1\,sec$. The histograms for each of these arrays were generated, and the Mann-Whitney U test was used for the statistical analysis [182]. The scans (Off/On) that showed significantly different motion patterns in the same subject were removed in order to prevent bias in the comparison of PMC OFF versus ON (i.e., if the subject moved significantly more or significantly less during one of the acquisitions). Figure 27 illustrates the process used to weed out scans with inconsistent motion. The procedure is as follows:

1. Motion patterns recorded by the OMTS;
2. Calculation of distributions, see Equation 71, mean and SD values for each degree of freedom;
3. Average of SDs for displacements and rotations;
4. Calculation of the motion parameter ratio between scans: $\frac{\sigma_{PMC-ON}}{\sigma_{PMC-OFF}}$, selection of subjects with similar motion patterns (i.e. the ratio of 1 ± 0.5), and exclusion of subjects where this ratio was smaller than 0.5 or larger than 1.5.

4.3 SUBJECTIVE IMAGE QUALITY ASSESSMENT

Four neuroscientists with at least five years of MR image processing and image-quality assessment expertise conducted subjective evaluations of image quality. The image quality was evaluated, with a focus on the degree of corruption brought on by motion artefacts. Scans were separated into six different groups, one for each contrast and in-plane resolution. Each rater performed a blinded side-by-side comparison, while the presentation of the two images with and without PMC was randomised. The raters were only instructed to evaluate the image quality in a paired (side-by-side) comparison and provide ratings to both image volumes considering the presence of motion artefacts. The score ranged from 1 to 10, where 1 corresponded to the worst image quality (greatest presence of motion artefacts) and 10 to the best image quality. Using Pingouin [183], the intraclass correlation coefficient was calculated [184, 185] to evaluate the agreement between raters (table 7).

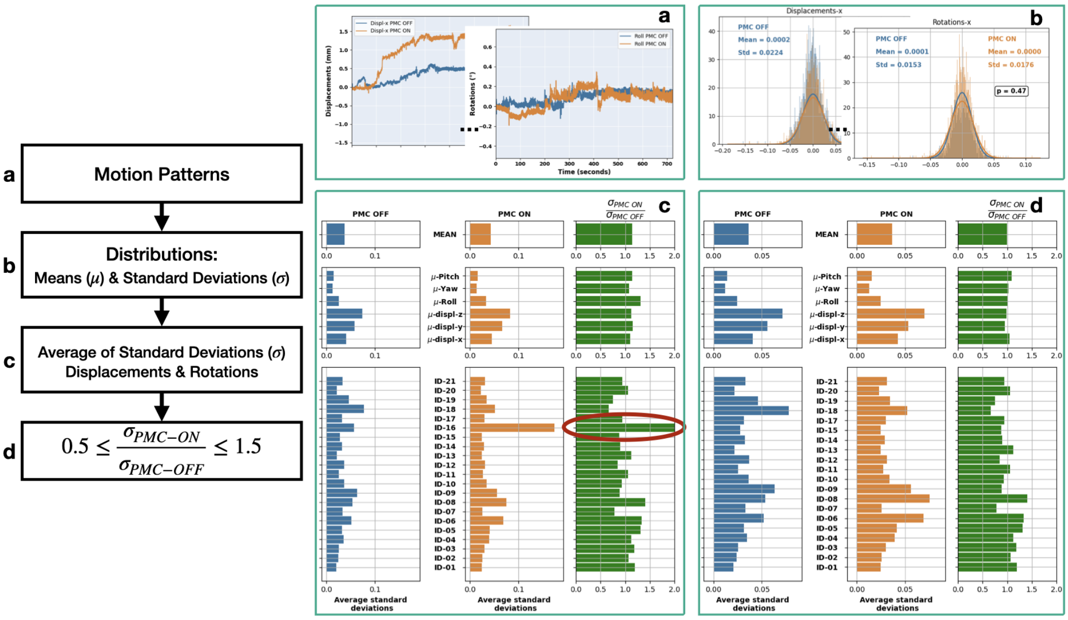

Figure 27: An example of motion pattern analysis and exclusion of volumes: a) motion tracking data; b) calculation of distributions, Equation 71; c) average of SD values of displacements and rotations for each subject/acquisition; d) filtered volumes, as explained in section 4.2 [with license from [180]].

Contrast	T1-w	T2-w	PD-w	T2*-w(05)	T2*-w(035)	T2*-w(035)
ICC	0.89	0.89	0.80	0.68	0.79	0.85

Table 7: Intra-class correlation coefficient (ICC). Average raters' absolute ICC per group. [with license from [180]]

4.4 OBJECTIVE IMAGE QUALITY ASSESSMENT

There have been several proposed criteria for evaluating the presence of motion artefacts or assessing the quantitative quality of MR images [141, 186–188]. For example, the MRIQC software [141] is a useful tool for automated quality assessment, it focuses mostly on T_1 and T_2 contrast image volumes acquired at lower magnetic fields (1.5 T and 3 T). While the Average Edge Strength (AES), which measures the amount of edge blurring in a picture, and a texture-based indicator based on the Haralick method are the two indicators used in the framework for PMC evaluation provided by Pannetier et al. [186]. Gradient entropy is frequently used to measure variations in the quality of MR images [187]. AES and gradient entropy were utilised in this study as metrics to quantitatively assess image quality. The gradient entropy values rise as the level of corruption rises, but the AES values fall as the motion artefacts rise [186, 187]. For the statistical analysis of the outcomes, the Mann-Whitney U test was used [182].

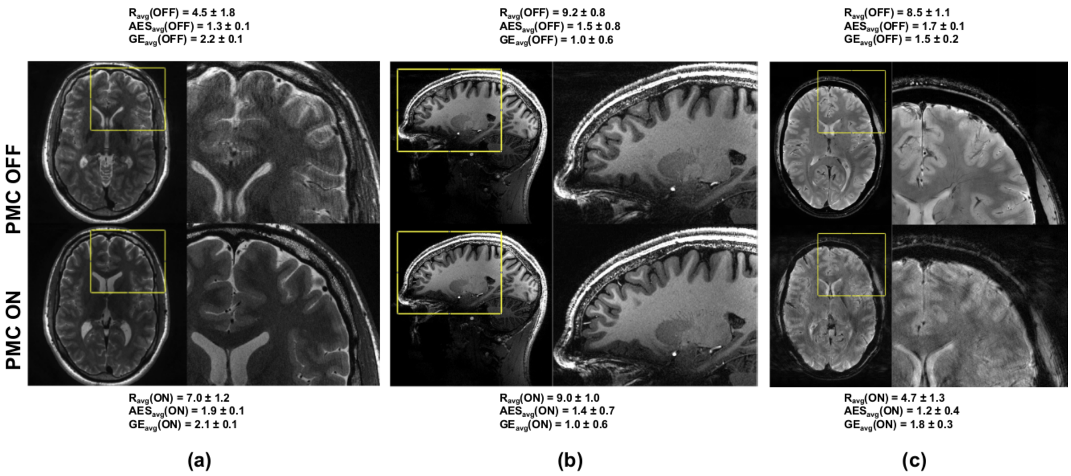

Figure 28: Sample images: All three possible scenarios. **(a)** PMC OFF worse performance than PMC ON, T_2-w images with resolution $0.28x0.28x1.0\,mm^3$; **(b)** PMC OFF similar performance as PMC ON, T_1-w images, isotropic resolution $0.45\,mm^3$; **(c)** PMC OFF better performance than PMC ON (reflections in the OMTS system, explained in Fig.29), T_2^*-w images, resolution $0.25x0.25x1.5\,mm^3$. R_{avg} is the average subjective score, while AES_{avg} and GE_{avg}, the average scores over all slices in the volume for AES and gradient entropy metrics, respectively. [with license from [180]]

4.5 RESULTS

There were three possible outcomes for each of the quality evaluations. The images acquired with PMC were first noticeably superior to the images of the same subject acquired using the same sequence but without PMC; second, the image quality of the images acquired with and without PMC was comparable; and third, the image quality of the images acquired with PMC was inferior to that of the images acquired without PMC support. These three potential outcomes are illustrated by examples of findings obtained with and without PMC in figure 28. Several scans were excluded from each group in accordance with the preceding scheme (see section 4.2 and figure 27). For instance, T_1-w images of Sub-ID 16 were disregarded because the subject moved excessively while being acquired with PMC ON, as shown in figure 27. The Sub-IDs 4, 6, 13, and 18 for T_2-w, 4, 6, 15, and 18 for PD, 6 for T_2^*(05) and 6, 15, and 16 for T_2^*(035), as well as 20 for T_2^*(025), were also disregarded. Also, T_2^*(025) of Sub-ID 16 was disregarded due to the existence of marker reflections, which resulted in incorrect tracking (figure 29). This is a drawback of such systems. If the marker is perfectly perpendicular to the camera, reflections will happen; as a result, the marker's surface will reflect the illumination back into the camera.

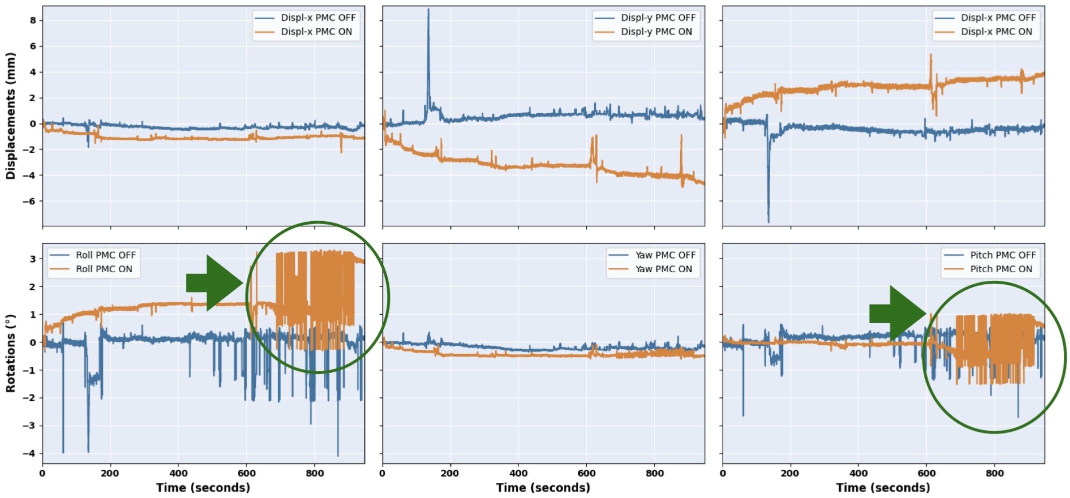

Figure 29: Motion patterns in the event of reflections of the MPT marker: false pose data marked with a green circle [with license from [180]].

The four raters evaluated the image quality for each of the 252 image volumes, notably checking for the presence of motion artefacts. Table 7's intraclass correlation coefficient showed that the raters' agreement ranged from 0.68 (for T_2^*[05]) to 0.89. (for T_1).

Compared to PMC OFF, PMC ON has demonstrated a statistically significant improvement (5.5%) across all contrasts and resolutions. For PMC OFF and PMC ON, the overall averaged score and SD were 8.21 ± 0.36 and 8.77 ± 0.24, respectively. Figure 30 gives information on each contrast group in detail. The outcomes are displayed for each rater, each contrast, and all available T_2^*-w image resolutions. Moreover, the average ratings from all raters are displayed. The experts gave PMC ON a higher grade for each of the T1, T2, and PD-w pictures. The picture quality of these groups' PMC ON scans improved by 9.6%, 9.8%, and 9.2%, respectively. There were no statistically significant differences in the T_2^*-w images. It should be noted, nevertheless, that the scores given to the scans without PMC were already rather good (between 8 and 10); as a result, there wasn't much room for improvement.

The AES and the gradient entropy were the two metrics employed for the objective evaluation, as explained in section 4.4. Figure 31 displays the outcomes. In favour of PMC ON acquisitions, the overall AES result was statistically significant (6% better). Only one contrast, T_2^*(025)) has demonstrated a substantial statistical improvement with PMC ON of 5.3% when each group is taken separately. With the

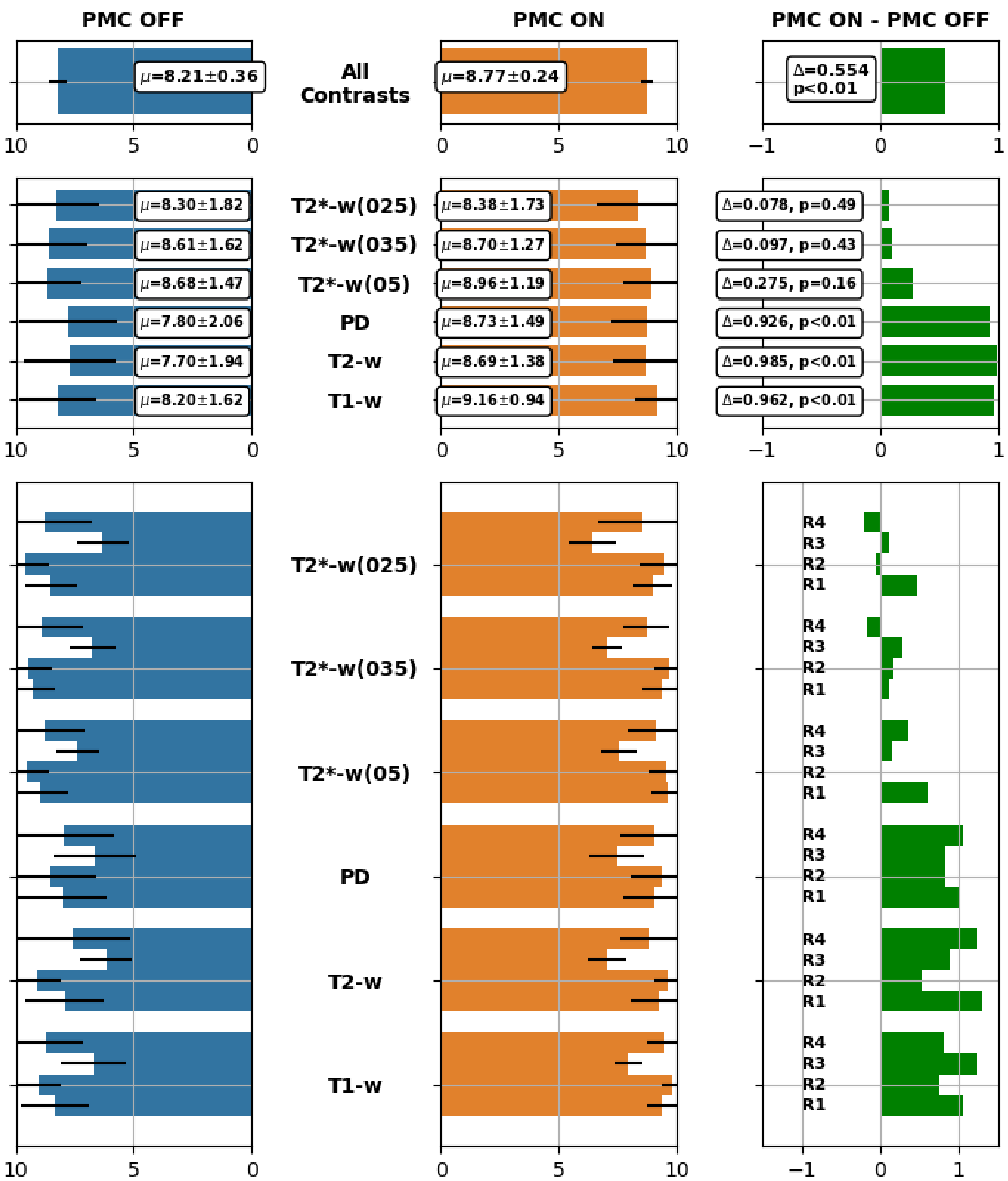

Figure 30: **Results of the subjective assessment.** Bar plots containing average scores calculated for each group and for all groups together. R1, ..., R4 refer to Reader 1 to Reader 4 [with license from [180]].

exception of the T_1-w images, where AES was marginally higher with PMC OFF, all of the groups showed improvements with PMC ON, even if this improvement was not statistically significant.
Gradient entropy did not reveal any statistically significant difference between the two groups — with and without PMC —when all contrasts were taken into account, not even when they were taken into account separately. Yet, for acquisitions supported by PMC, gradient entropy consistently produced favourable outcomes,figure 31.

All the results, including motion patterns and statistical analysis of the relative metrics can be viewed at `https://github.com/sarcDV/PMC-Results`.

4.6 DISCUSSION

In this study, a thorough assessment of PMC has been carried out for ultrahigh field structural brain imaging on a group of healthy volunteers who were told to remain as still as possible throughout the scans. To compare and quantify the variations between the high-resolution in vivo brain imaging of these healthy compliant subjects acquired with and without PMC, systematic subjective and objective evaluations have been made.
The images, whether they were collected with or without PMC, received ratings that were primarily between 8 and 10, as shown in figure 30. Hence, regardless of the correction status, all scans exhibited high to extremely high image quality. Yet, it was still clear from the overall subjective rating that using PMC enhanced the image quality. For the subjective assessment, the use of PMC had a statistically significant favourable effect for three of the four contrasts (three of the six groups), and there was still an improvement for the final contrast (three groups of T_2^*-w images), but it was not statistically significant. The intraclass correlation coefficient ranged between 0.68 and 0.89 despite the fact that all of the experts who participated in the evaluation process had experience evaluating the quality of MR images and had received similar training. It is crucial to emphasise that the aim was to determine the degree of deterioration in addition to determining whether a picture was corrupted or degraded by artefacts. This needs to be stressed because it differs significantly from how clinical routine is usually conducted, in which scans are evaluated within a few seconds to determine whether rescanning is required or the image quality is sufficient to make a clinical diagnosis.
PMC can improve the image quality for five out of six groups (T_2, PD, T_2^*[05], T_2^*[035], and T_2^*[025]), according to both objective measures. In contrast to the subjective assessment, which indicated statistically significant findings in favour of PMC ON for this contrast, for T_1-w images, AES is in favour of PMC OFF while gradient entropy has revealed no difference (both not being statistically significant). However, a MP-RAGE case where AES is better without correction but the images are visibly better with PMC is shown in figure 33. This typically raises the issue of how broadly these measurements may be used to evaluate the quality of small motion artefacts [189]. For instance, Mattern et al. [190] used a similar sequence to scan

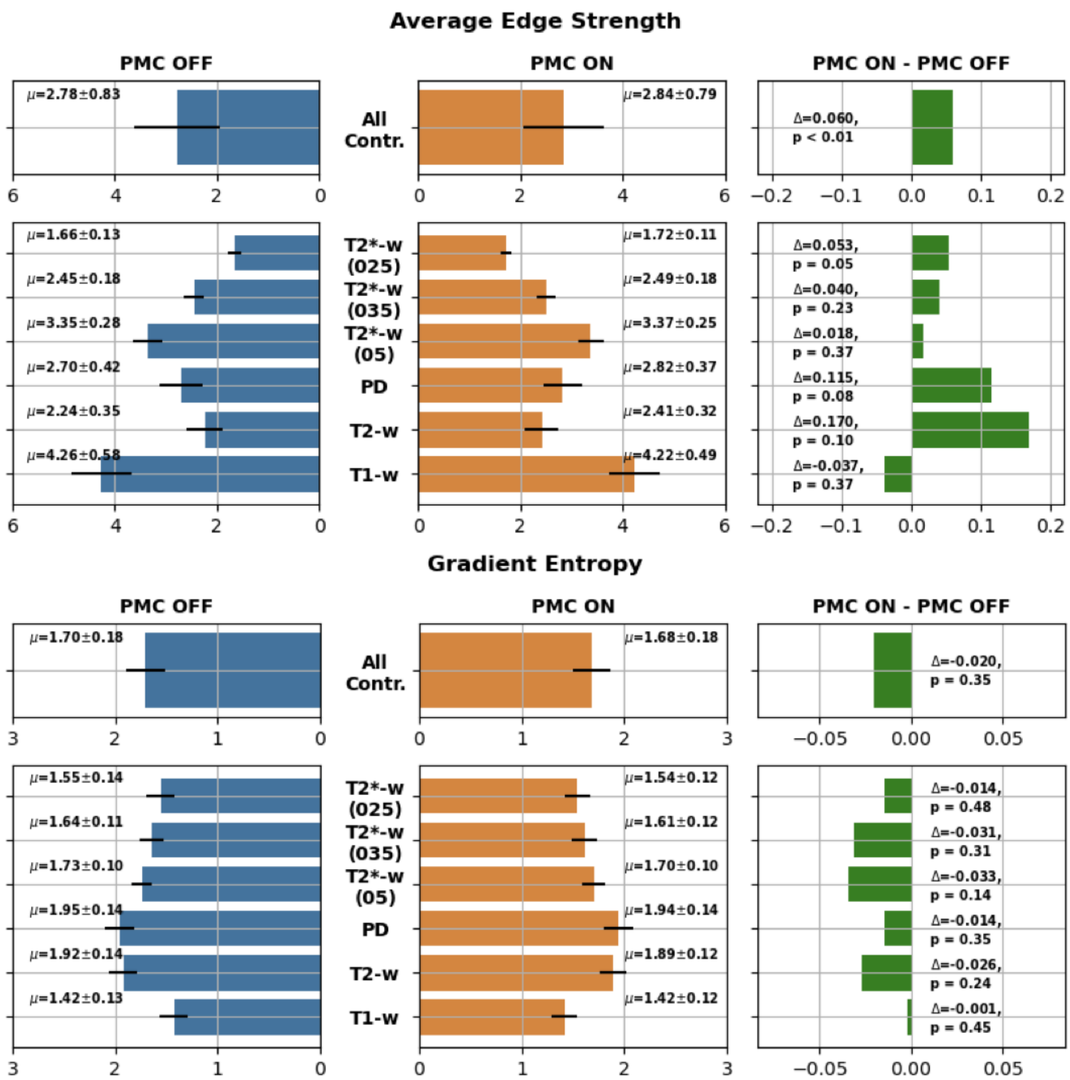

Figure 31: Results of the objective assessment: bar plots containing average scores calculated for each group and for all groups together. Top: Average Edge Strength; Bottom: Gradient Entropy [with license from [180]].

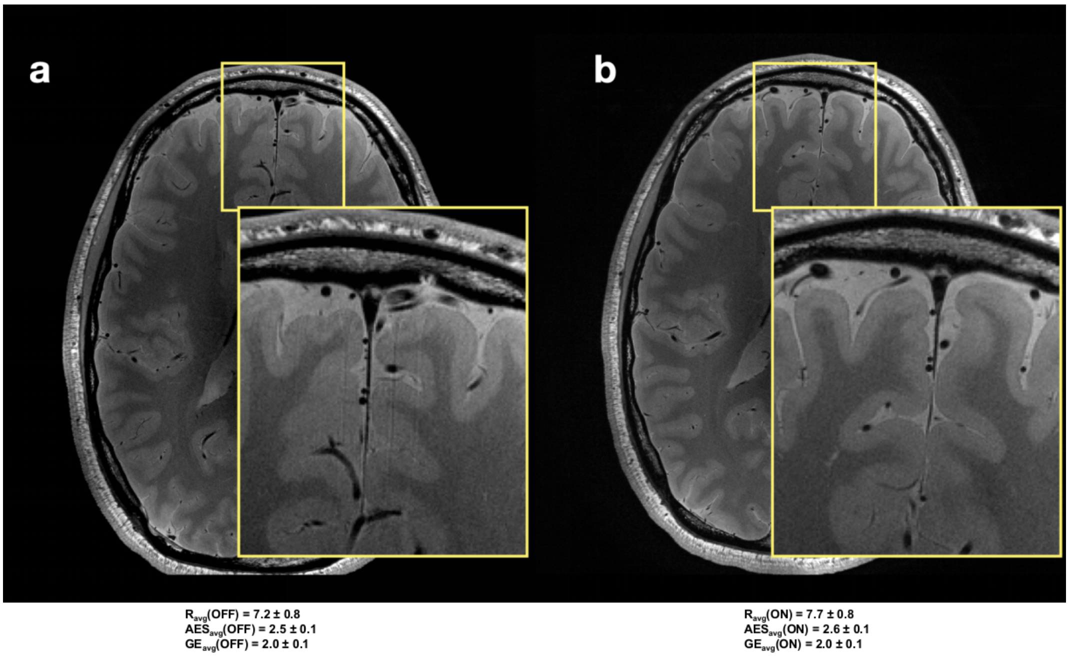

Figure 32: Comparison of PD-w images acquired for the same subject. Left side (a) image acquired without the support of PMC. Right side (b), the image acquired with PMC. For both images, a zoomed-in area shows details. The subjective average score (R_{avg}), and the average AES (AES_{avg}) and average gradient entropy (GE_{avg}) over all slices in these volumes are reported [with license from [180]].

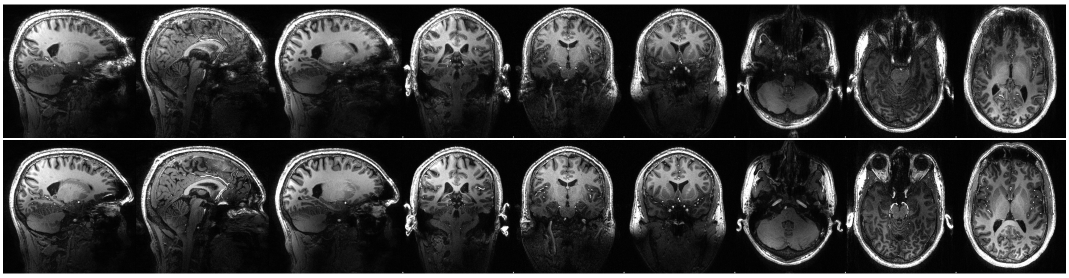

Figure 33: Comparison of T1-w images acquired for the same subject. Top row: PMC Off, bottom row: PMC On.

four healthy subjects (instead of the 2D sequence used in this work, they used a 3D gradient-echo sequence for susceptibility-weighted imaging). In their work, PMC acquisitions with a resolution of $0.33\text{x}0.33\text{x}1.25\ mm^3$ demonstrated a notable reduction in motion artefacts in the majority of cases and a significant improvement in the reliability of quantitative susceptibility values. Four subjects were scanned using equivalent sequences in a different study by Stucht et al. [181]. Moreover, the $0.44 - mm^3$ isotropic T_1-w images and the $0.25\text{x}0.25\text{x}2.0\ mm^3$ gradient-echo (T_2^*-w) images in their work demonstrated the potentiality of PMC. However, in terms of the number of scanned subjects as well as the variety and amount of sequences acquired for each subject, these studies cannot be properly compared.

Although each sequence was tested on a phantom to assess the effect of vibrations and found that gradients had no impact on the motion patterns or image quality, it was not possible to conclusively demonstrate that the same is true for in vivo imaging. The mechanical characteristics and coupling of the setup may change depending on the experimental settings, such as how the patient table is loaded. Additionally, the performance of the OMTS may be impacted by various mounting circumstances. With the exception of one scan, no anomalies were observed in the tracking data that suggest potential PMC faults or erroneous tracking (discussed in section 4.5 and shown in figure 29). The camera was mounted using Velcro straps, as stated in section 2.3, figure 12. No further investigation was performed into the Velcro's ability to guarantee the mechanical properties and orientation of the camera remaining steady throughout a scan and in between scans. A similar point of concern is present regarding Velcro's gradual deterioration with continued usage. This might result in various mounting situations, which would then impact how well the OMTS worked. Moreover, variations in contrast and SNR may influence the outcomes of the objective evaluation [133, 191]. It is notable that in some instances (shown in figure 32), the PMC-ON image's artefact reduction was not immediately apparent.

According to these findings, PMC employing an OMTS can enhance the image quality of already excellent scans of healthy, compliant people without the presence of intentional motion.

4.7 PMC FOR INTENTIONAL MOTION

This section describes an additional scanning session performed for only three healthy volunteers to evaluate the use of PMC in case of intentional movements. The 3D-MP-RAGE sequence described in table 6 was used. The scan was repeated four times per subject, with and without PMC, with and without intentional motion. For the acquisitions with intentional motion a video was shown to each subject and was asked to follow the object shown in the video with their own head. The intentional motion can be used to simulate clinical conditions such as tremor or dyskinesia. This study served to test the effectiveness of PMC in the case of large movements always trying to emulate a clinical-type scenario.
A summary of each session per subject is shown in figures 34, 35, and 36. At first sight, utilising PMC seems to have no significant difference when primarily examining the scenario without deliberate motions. The exception is the case of subject number 1 shown in figure 34, in fact, when scanning with PMC ON and although the subject was instructed to remain as stable as possible, sudden movements with amplitudes of more than 1 cm and rotations of more than 5° were recorded. These movements affected the acquisition and the images show residual motion artefacts.
On the other hand, considering the scenario with intentional movements, once again the use of PMC is of paramount importance in limiting the presence of motion artefacts. Although, the system is not able to completely prevent the presence of motion artefacts, brain structures are better delineated than in images acquired without PMC.

4.8 CONCLUSION

In order to systematically evaluate high-resolution MRIs at 7T in cooperative subjects, this thesis work presented a large-scale study on PMC. The majority of the acquired images showed very high or high image quality. Every scenario has improved according to subjective evaluation with PMC ON, however, only three of them were statistically significant. For five of the six groups, objective measures have demonstrated that the images obtained with PMC were of higher image quality; however, for the sixth group, the metrics did not agree on a clear winner and did not accord with the subjective metric. In this research, only the images with comparable motion patterns for PMC ON and OFF were taken into account. Hence, PMC can be credited for the improvements seen. Based on our findings, we draw the conclusion that PMC offers higher image quality for high-resolution images when there is no deliberate motion and that it should be taken into account even when high-resolution scans at 7T are obtained from healthy compliant participants. Furthermore, evaluations conducted on volunteers with intentional motion also provided insights into the limits of PMC for extreme cases and demonstrated that PMC can improve image quality even when the level of motion is very high. Based on which it can be concluded that it can be used with non-complaint patients (e.g. patients with Parkinson's disease) as well if used in conjunction with further motion prevention techniques or with RMC.

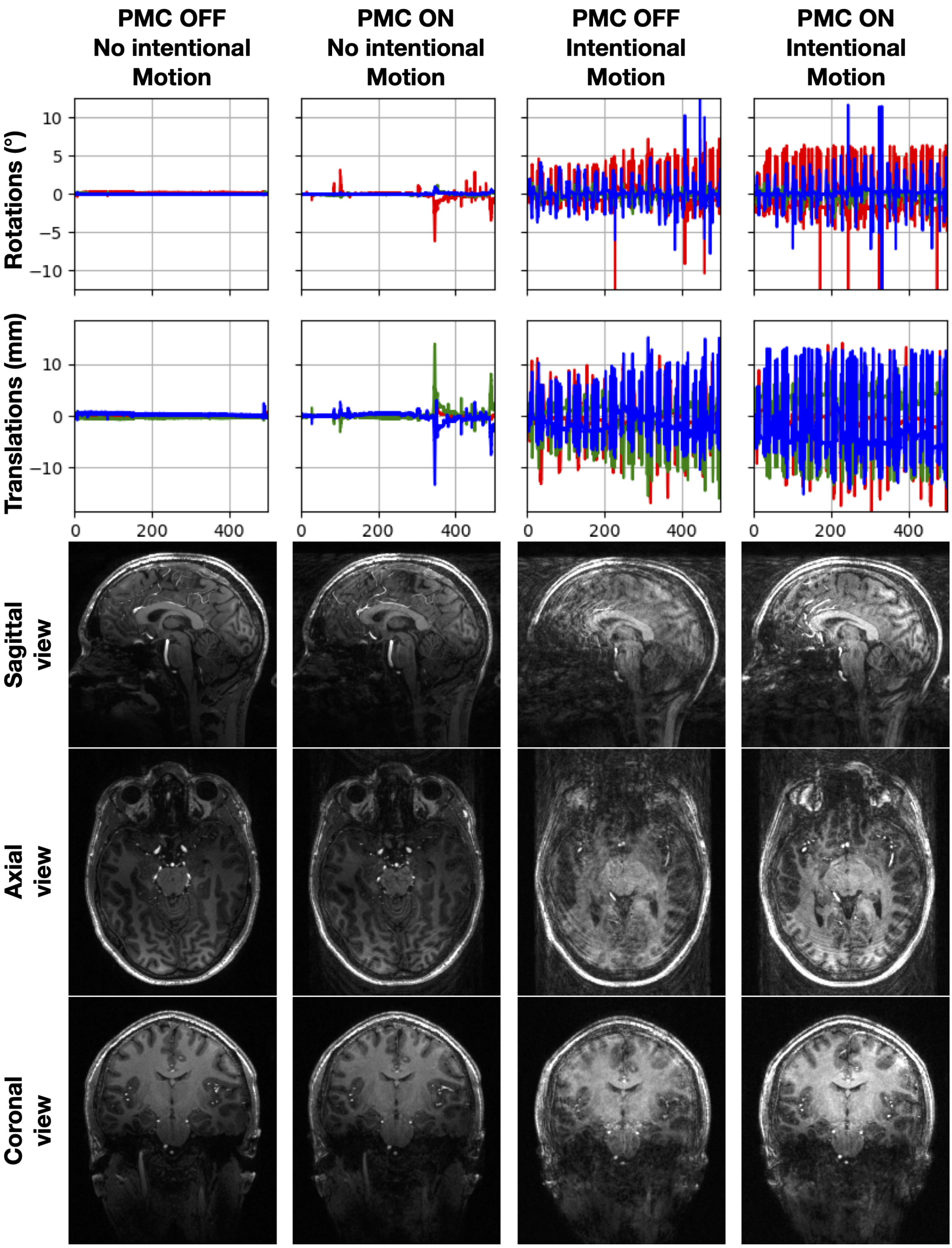

Figure 34: From top to bottom, the first two rows show the rotations and translations stored in the log files of each scan, third, fourth and fifth row a slice in sagittal, axial and coronal view, respectively. From left to right, first column scan without intentional motion and PMC OFF, second no intentional motion and PMC ON, third intentional motion with PMC OFF and last column, intentional motion with PMC ON.

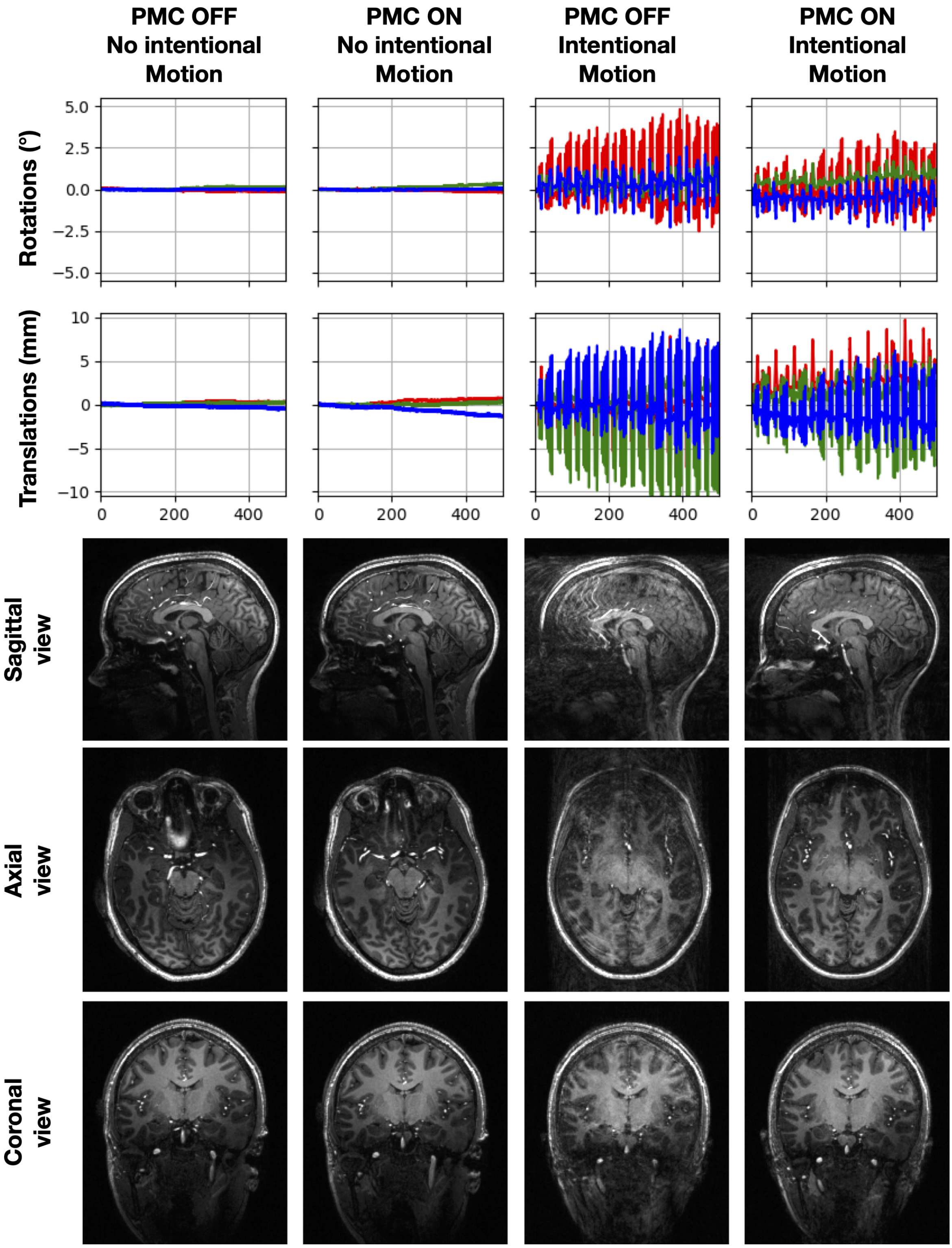

Figure 35: As in figure 34.

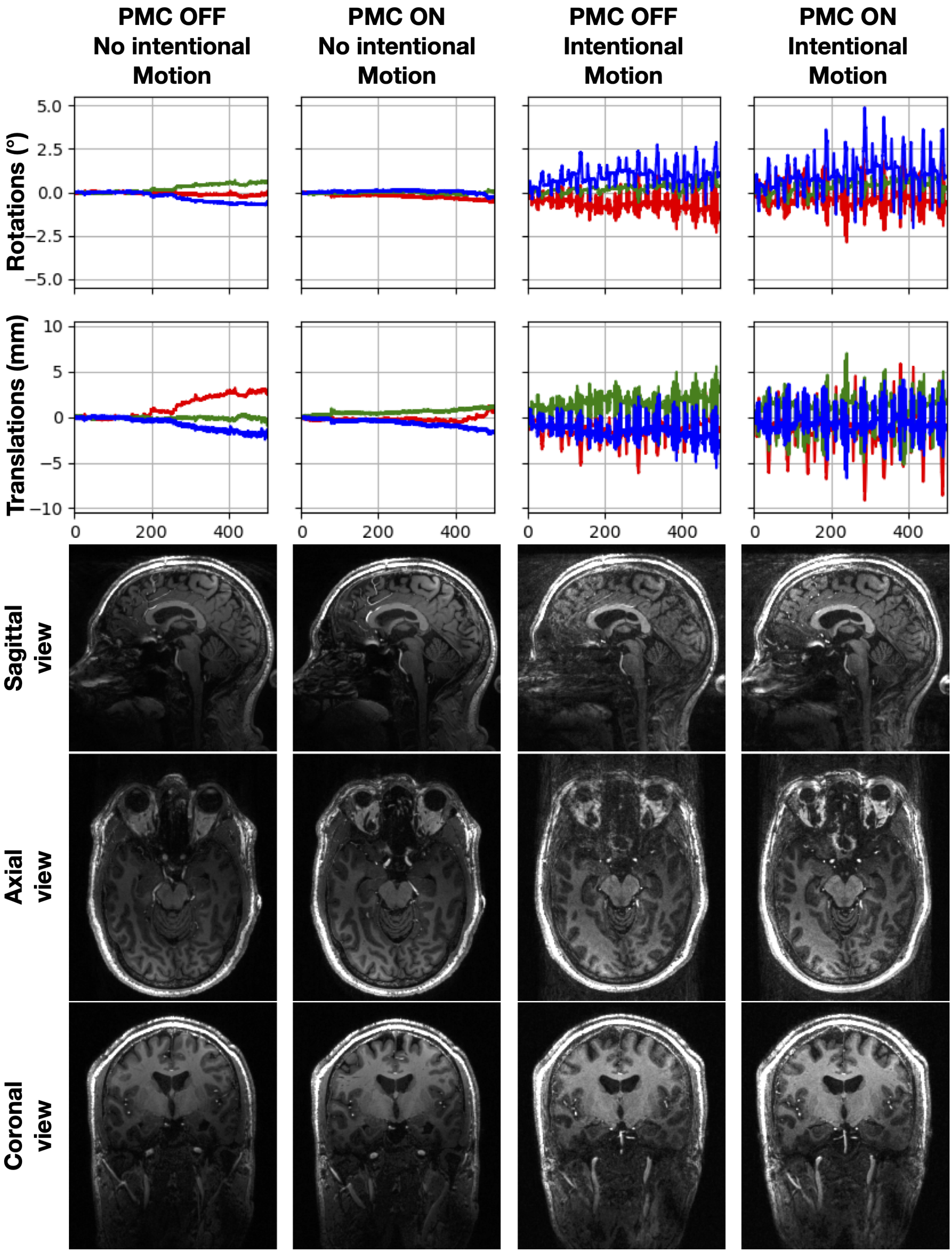

Figure 36: As in figure 34.

Part IV

RETROSPECTIVE MOTION ARTEFACTS DETECTION AND CORRECTION USING DEEP LEARNING

5 MOTION ARTEFACTS DETECTION AND RETROSPECTIVE CORRECTION USING DEEP LEARNING

The motion detection and correction research using deep learning techniques are the focus of this section. Contrary to the PMC section (sections 2 and 4), where the goal was to correct motion artefacts in ultra high-resolution images acquired at ultra-high field, the objective of these methods are to supplement the aforementioned section. They have been applied to images acquired both at the ultra-high field and in a clinical setting.

As the first step, the thesis presents a novel deep learning based IQA technique in section-5.1, to assess the quality of an MRI in terms of the presence of motion artefacts. As part of the same, a new set of contrast augmentation techniques was developed - to make deep learning methods more robust against changes in MRI contrast, and also created an in-house motion simulation pipeline - to be able to create larger training datasets with motion artefacts resembling real-world motion in MRI. Furthermore, this thesis presents two novel techniques to perform RMC using deep learning. Section-5.2 presents novel techniques to modify existing deep learning models - to improve their motion correction capabilities using "prior-assistance", while section-5.3 combines contrast augmentation techniques (presented in section-5.1) with deep learning model to improve the generalisability of the model.

5.1 IMAGE QUALITY ASSESSMENT THROUGH SSIM PREDICTION

As explained in section 1.5 motion artefacts in MRIs can significantly lower the accuracy of a diagnosis. Prior to moving further with the clinical diagnosis, the quality of the MR image must be evaluated. Motion artefacts may necessitate a repeat scan because they can change how certain structures, such as the brain, lesions, or tumours, are defined. Otherwise, a misdiagnosis (such as the wrong pathology) or inaccurate diagnosis (such as the correct pathology but inappropriate severity) may occur.

After scanning, IQA is a quick, automated process that can help determine whether the obtained images are sufficient for diagnosis [132–134]. This procedure's major goal is to establish if the images are diagnostically reliable and devoid of undesirable artefacts [136, 137]. The evaluation process frequently takes time and depends on the observer's subjective judgement [138]. Also, the readers' (the experts chosen to conduct the IQA) varying degrees of experience and knowledge could produce inconsistent assessment outcomes. The lack of a reference image is another inherent problem with the IQA for MR images. In recent years, reference-free IQA methods with and without machine learning and deep learning support have been

presented for the assessment of visual image quality [134, 136, 139–146]. However, there is still no gold standard IQA for MR images, despite the fact that the number of typical machine learning and deep learning approaches utilised for regression and classification tasks is constantly growing [133, 149–152].
The purpose of this work is to develop an automated IQA tool based on the prediction of the SSIM [153] that can identify the presence of motion artefacts and measure the degree of corruption or distortion in comparison to an "artefact-free" counterpart. This tool was created to function for a wide range of MR image contrasts, including T_1, T_2, PD, and FLAIR weighted images, and without regard to the resolution or orientation of the image under consideration. A contrast augmentation step has also been added in order to broaden the weighting range. When MRIs are acquired in real life, and there are any artefacts in the image, there are no "artefact-free" equivalents to compare the image to in order to determine its quality. However, two pictures are necessary for SSIM calculation (corrupted vs motion-artefact-free images). Due to this, two separate methods were used in this work to artificially produce corrupted images: one was built in-house [110](see section 7.2) while the other was implemented by Shaw et al. [154] (package of the library TorchIO [155]).

ResNets are the core of the proposed automatic IQA method [157, 192]. ResNets with two different depths were used here: 18 (ResNet-18) and 101 (ResNet-101), see section 7.2. Each model has undergone two separate training sessions, both with and without the contrast enhancement step. During the training, these procedures are carried out,(figure 37):

1. a random slice (2D image) from one of the three orientations - axial, sagittal, and coronal - is chosen from a 3D input volume. Slice selection for anisotropic volumes is limited to maintaining the orientation of the initial acquisition;

2. if contrast augmentation is enabled, one of the following contrast augmentation algorithms is randomly chosen:

    - Gamma adjustment on the input image [193];
    - Logarithmic adjustment on the input image [194];
    - Sigmoid adjustment on the input image [195];
    - Adaptive histogram adjustment on the input image [196];

3. the 2D image is subjected to motion corruption using one of these two methods:

    - TorchIO [154, 155], Figure 38 (a);
    - in-house algorithm, Figure 38 (b);

4. between the input 2D image and the associated corrupted image, the SSIM is determined;

5. the selected model is given the corrupted image and the calculated SSIM value for training.

Table 8 lists the three datasets that were used in this study: the train, validation, and test sets. 200 volumes were utilised for training, 50 for validation, and 50 for testing. the second group (Table 8, Site-A) of 114 volumes were acquired with a 3T scanner, the third group (Table 8, Site-B) of 93 volumes was acquired at 7T, and a final group (Table 8, Site-B) of 25 volumes were acquired with various scanners. The first group, which consisted of 68 volumes, was chosen from the public IXI dataset[1](1.5 and 3T). Resampling was done on the volumes from IXI, Site-A, and Site-B to achieve an isotropic resolution of 1.00 mm^3.
The following parameters were chosen for the training:

- learning rate: $1e^{-3}$;
- batch size: 100;
- loss function: Mean Squared Error (MSE) [197];
- optimizer: the Adam optimizer [198];
- number of epochs: 2000.

All the images were always normalised and resised or padded to have a 2D matrix size of 256x256. From the 50 volumes of the test dataset, a total of 10,000 pictures were repeatedly chosen at random, corrupted, and tested using the same procedures as during training, including contrast augmentation, random orientation selection, and corruption.
The predicted SSIM values were first displayed against the ground truth SSIM values, as shown in Figure 40, and then the residuals were calculated as follows to assess the performance of the trained models. Figure 41 shows $Residuals = SSIM_{predicted} - SSIM_{groundtruth}$.
An image's expected SSIM value can be compared to an indicator of the degree of distortion or corruption in the image. To compare this value with a subjective evaluation, however, is difficult when using this method on a real clinical case. This issue was resolved by turning the regression task into a classification task. Three distinct experiments for the same were carried out by selecting 3, 5, and 10 classes, respectively. The SSIM range [0-1] was evenly divided into sub-ranges for each scenario. For example, there were three sub-ranges for the three classes: class-1: [0.00-0.33], class-2: [0.34-0.66], and class-3: [0.67-1.00]. The same procedure was used to create classes for 5 and 10.
The trained models were also tested using a second dataset made up of randomly chosen images from clinical acquisitions. As indicated in Table 9, this dataset included five subjects, each of whom had had a different number of scans. As there were no ground truth reference images in this situation, one expert also performed

1 Dataset available at: https://brain-development.org/ixi-dataset/

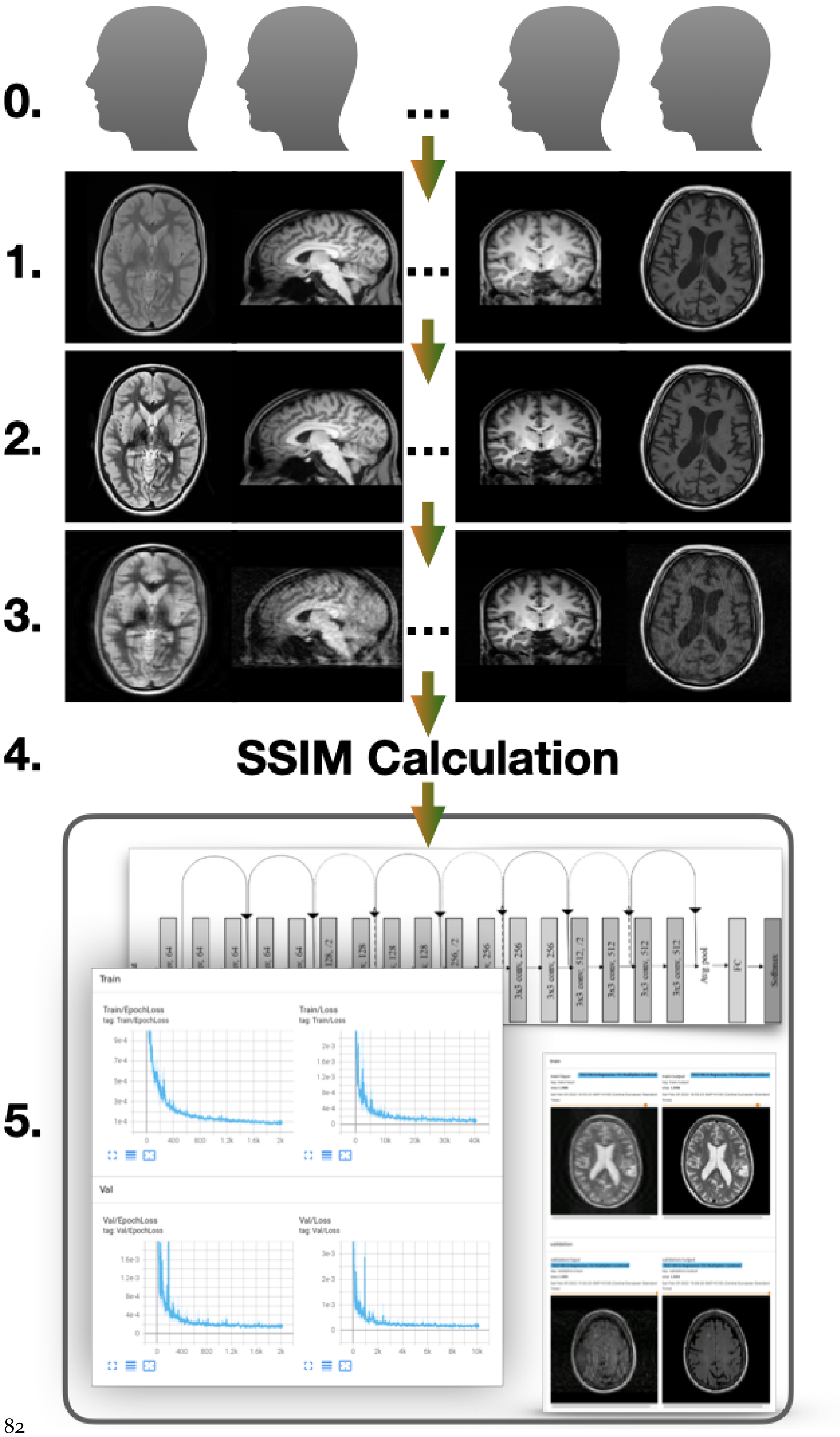

Figure 37: Graphical illustration of the pipeline developed.

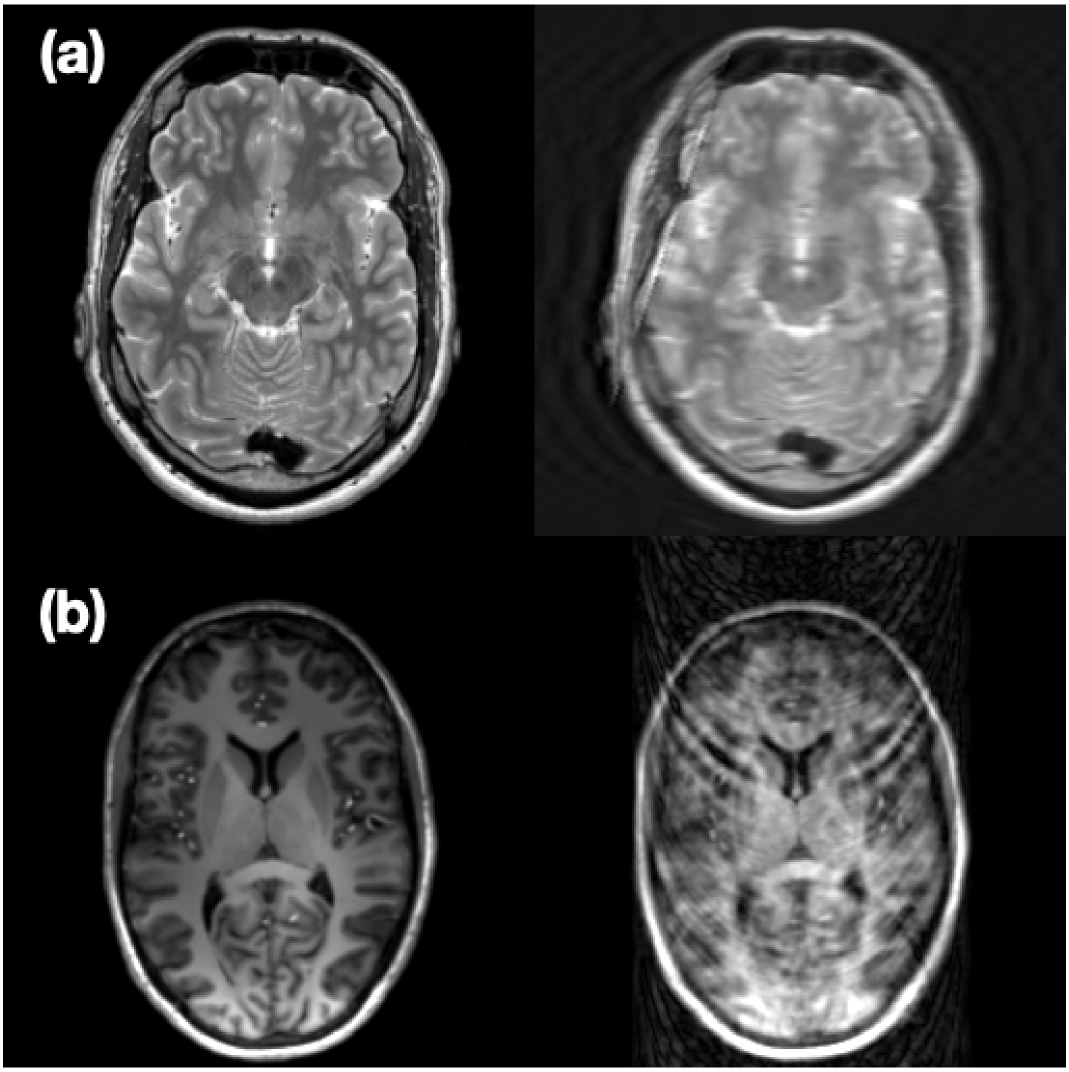

Figure 38: Sample of artificially corrupted images. On the left column are the original images, and on the right are the corrupted ones. **(a)**: image corrupted making use of TorchIO library, **(b)**: image corrupted making use of the home-made algorithm

Table 8: Data for training, validation and testing.

Data	**Weighting**	**Volumes**	**Matrix Size** m(M) x m(M) x m(M)†	**Resolution** (mm^3) m(M) x m(M) x m(M)†
		TRAINING		
IXI	T1,T2,PD	15,15,15	230(240)x230(240)x134(162)	1.00 isotropic
Site-A	T1,T2,PD,FLAIR	20,20,20,20	168(168)x224(224)x143(144)	1.00 isotropic
Site-B	T1,T2,FLAIR	20,20,20	156(156)x224(224)x100(100)	1.00 isotropic
Site-C	T1	3	192(512)x256(512)x36(256)	0.4(1.0)x0.4(0.9)x0.9(4.4)
Site-C	T2	11	192(640)x192(640)x32(160)	0.4(1.0)x0.4(1.0)x1.0(4.4)
Site-C	FLAIR	1	320x320x34	0.7x0.7x4.4
		VALIDATION		
IXI	T1,T2,PD	1,5,7	230(240)x230(240)x134(162)	1.00 isotropic
Site-A	T1,T2,PD,FLAIR	4,4,4,4	168(168)x224(224)x143(144)	1.00 isotropic
Site-B	T1,T2,FLAIR	6,6,4	156(156)x224(224)x100(100)	1.00 isotropic
Site-C	PD	1	240x320x80	0.8x0.8x2.0
Site-C	T2	1	240x320x80	0.8x0.8x2.0
Site-C	PD	1	240x320x80	0.8x0.8x2.0
		TESTING		
IXI	T1,T2,PD	2,4,4	230(240)x230(240)x134(162)	1.00 isotropic
Site-A	T1,T2,PD,FLAIR	6,4,4,4	168(168)x224(224)x143(144)	1.00 isotropic
Site-B	T1,T2,FLAIR	6,6,5	156(156)x224(224)x100(100)	1.00 isotropic
Site-C	T1	2	288(320)x288(320)x35(46)	0.7(0.8)x0.7(0.8)x3.0(4.4)
Site-C	T2	2	320(512)x320(512)x34(34)	0.4(0.7)x0.4(0.7)x4.4(4.4)
Site-C	FLAIR	1	320x320x35	0.7x0.7x4.4

†: "m" indicates the minimum value while "M" is the maximum.

Table 9: Clinical data

Data	Weighting	Volumes	Matrix Size m(M) x m(M) x m(M)†	Resolution (mm^3) m(M) x m(M) x m(M)†
Subj. 1	T1,T2,FLAIR	1,4,2	130(560)x256(560)x26(256)	0.4(1.0)x0.4(0.9)x0.9(4.4)
Subj. 2	T2	3	288(320)x288(320)x28(28)	0.7(0.8)x0.7(0.8)x5.5(5.5)
Subj. 3	T1,T2,FLAIR,DWI,(§)	1,2,1,4,1	256(640)x256(640)x32(150)	0.4(0.9)x0.4(0.9)x0.4(4.4)
Subj. 4	T2, FLAIR, DWI	1,2,6	144(512)x144(512)x20(34)	0.4(1.4)x0.4(1.4)x2.0(4.4)
Subj. 5	T2, FLAIR, DWI	3,1,4	256(640)x256(640)x28(42)	0.4(1.0)x0.4(1.0)x3.3(6.2)

†: "m" indicates the minimum value while "M" the maximum.

a subjective assessment of the images' quality using the classification scheme described below. Class 1 images are of good to high quality, in which case the images may have very minor motion artefacts, but the accurate delineation of the brain's structures, substructures, or lesions (SSIM range between 0.85 and 1.00); class 2 images are of sufficient to good quality, in which case the images may have motion artefacts that prevent correct delineation of the brain structures, substructures or lesions (SSIM: 0.60 - 0.85); and class 3 images are of insufficient quality and necessitate a re-scan (SSIM: 0.00 - 0.60). Also, this dataset featured many contrasts that weren't present during training, like diffusion-weighted pictures (DWI).
When used on clinical data, the MRIQC[2] [141] toolbox has been taken into consideration as a baseline for direct comparison. It is significant to note that MRIQC only derives a number of no-reference image quality measures from functional MRI data and T1w and T2w 3D image volumes. As a result, during the quality assessment, several of the clinical volumes were rejected. Moreover, as MRIQC only functions on acquisitions that have been properly transformed to the BIDS[3] format, it could not be utilised to evaluate images that have been artificially corrupted (i.e. artificially corrupted 2D slices are not suitable for MRIQC). The Contrast-to-Noise Ratio (CNR) [199], Coefficient of Joint Variation (CJV) [200], Entropy Focus Criterion (EFC) [201], and so-called Quality Index (QI) [134] were utilised as metrics for structural images. The CNR is a widely used image metric and a straightforward extension of the SNR computation. It can measure how distinct the tissue distributions of grey matter and white matter are from one another (GM and WM). Better image quality is indicated by higher values. The existence of heavy head motion and large-intensity non-uniformities (INU) can be detected by the second selected metric, CJV, and for this metric, lower values suggest higher image quality. The EFC is one of the earliest proposed metrics that can be found in MRIQC. The degree of ghosting and blurring brought on by head motion can be measured using this metric. It takes advantage of the voxel intensities' Shannon entropy. Image quality is higher in images with lower EFC values. The final quality metric, QI,

2 https://mriqc.readthedocs.io/en/latest/about.html
3 https://bids-specification.readthedocs.io/en/stable/index.html

is a binary indicator that shows whether there are artefacts present or not. When QI is not zero, there are artefacts in the image, whereas 0 QI shows no artefacts. These metrics were chosen over the others because of their focus on quantifying and detecting artefacts. For each selected parameter, the Subjective Image Quality Assessment (SIQA) scores were specifically averaged, normalised, and scaled in order to analyse the agreement with the results. The SIQA scores were per slice, but MRIQC delivers a single value for each metric of every scan, necessitating the averaging step. The SIQA scores were normalised and scaled for the first three measures, CNR, CJV, and EFC, using the first image volume that MRIQC analysed as a reference. In contrast, using the QI measure, the averaged SIQA scores between 1 and 2 were transformed to zero values to denote the absence of motion artefacts; otherwise, 1 was reported to indicate the existence of artefacts.

5.1.1 *Results*

Figure 39 shows a few example outputs of the SSIM prediction for quantitative analysis, while figures 40 and 41 present the outcomes qualitatively. The SSIM values are plotted against the ground truth values in Figure 40. The plot additionally displays the linear fitting carried out for every trained model. Finally, the distributions of the actual values and the predicted values for the SSIM are also displayed. Figure 40 illustrates the qualitative dispersion levels of all trained models. The term dispersion in this context refers to the degree to which the predicted SSIM values differ from the ground truth when $SSIM_{predicted} = SSIM_{groundtruth}$. Nonetheless, each model's results are displayed independently in Figure 40 using scatter plots. Section 5.1 provides an explanation of the relative residual distribution charts. Using the SciPy Python package [202], a statistical normal distribution fitting was done for the residual distributions. Figure 40 displays the derived mean and standard deviation values. The ResNet-18 model trained with contrast augmentation had the smallest standard deviation ($\sigma = 0.0139$) and the mean value that was the closest to zero ($\mu = 0.0009$), according to the statistical analysis, whereas the ResNet-101 model trained without contrast augmentation had the mean value that was the farthest from zero and the largest standard deviation. The results show a noticeable impact of contrast augmentation for both ResNet-18 and ResNet-101 models. This is manifested as a decline in standard deviation values, which is visually correlated with a reduced scatter plot dispersion level.
Figure 42 and table 10 display the classification task results. The logarithmic confusion matrices obtained for the classification task are displayed in Figure 42. It should be observed that every trained model behaved flawlessly and uniformly. Particularly, none of the matrices displays non-zero elements that are distant from the diagonal, only those that are nearby, which is what is typically expected from a classification task. Table 10 is an addition to Figure 42. It displays the precision, recall, and f1-score for all of the trained models on a class-by-class, macro-average, and weighted basis. The accuracy is also shown in this table.
The model with the best performance is ResNet-18 trained with contrast augmen-

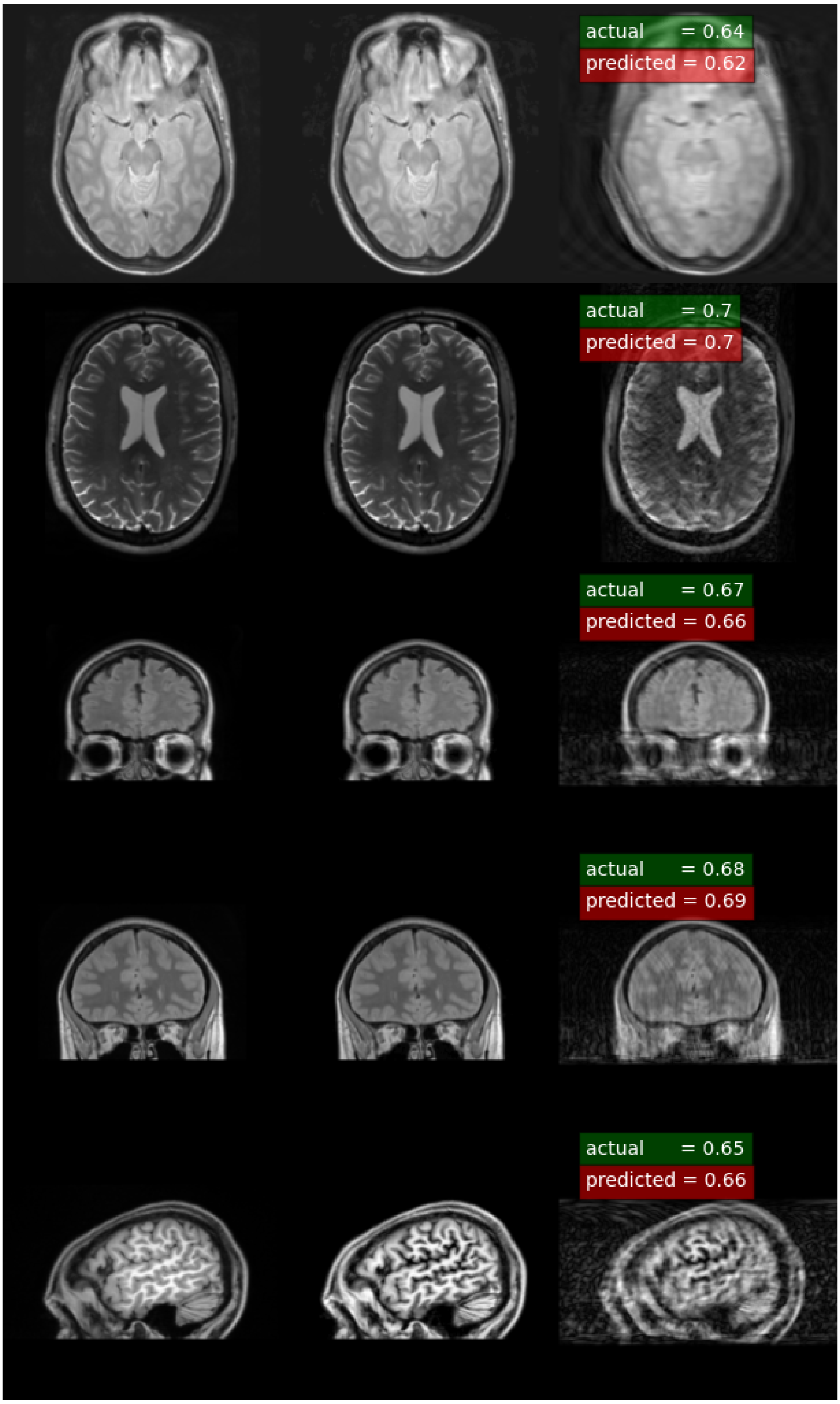

Figure 39: Few examples for qualitative evaluation. Columns from left to right: actual MRI, MRI after contrast augmentation, contrast augmented MRI after motion corruption. The ground truth (SSIM between second and third columns) and predicted SSIMs are mentioned on the motion corrupted images.

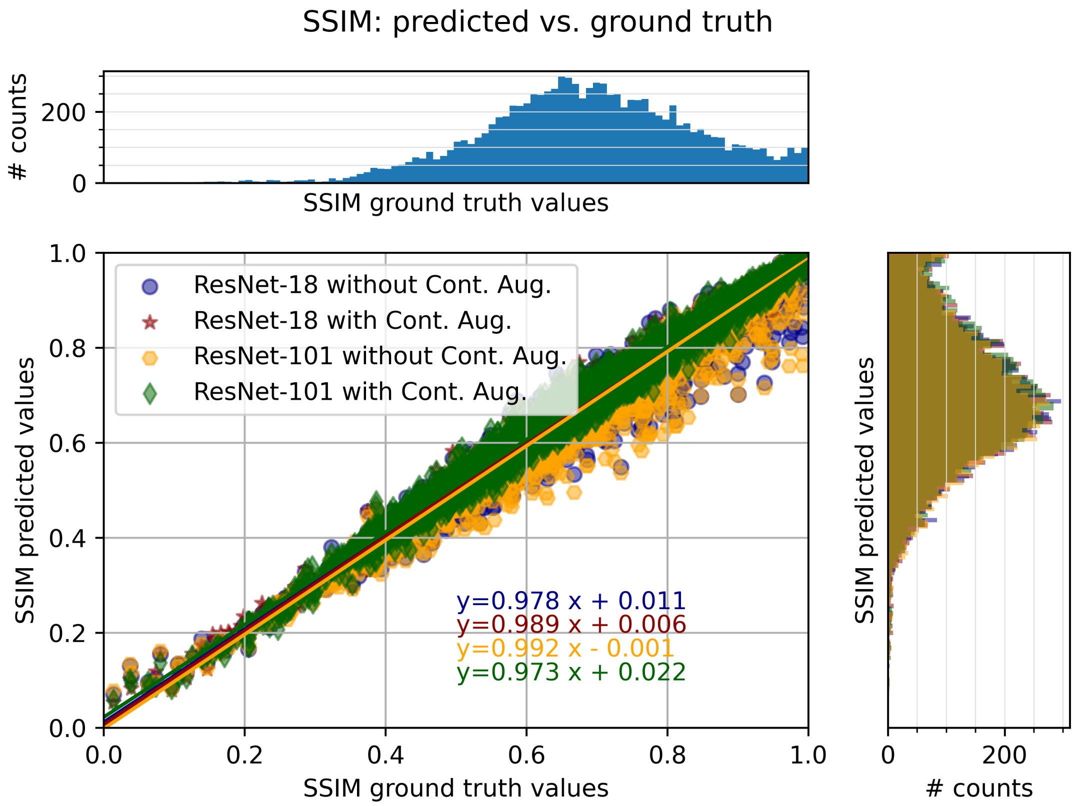

Figure 40: Scatter plot of SSIM prediction. Moreover, the linear fits for each group of data are displayed. Ground truth SSIM values distribution is shown at the top, while predicted SSIM values distributions for each group are shown on the right.

tation for all three scenarios, 3, 5, and 10 classes as shown in section 5.1. For scenarios involving 3, 5, and 10 classes, this model consistently yielded accuracy values of 97, 95, and 89%, respectively. Although the ResNet-18 with contrast enhancement outperformed the other models, there are no obvious changes in the tabular data. But once more, when contrast augmentation is used, it is possible to see a performance enhancement.
Figure 43 displays the outcomes for the clinical data samples. The derived SSIM predictions are illustrated in this instance for each model, overlaid with the subjects' subjective ratings and displayed in a per-slice fashion. As stated in section 5.1, following a comprehensive visual inspection, the clinical data samples' subjective ratings fell into one of three categories: 1, 2, or 3. If the predictions made using the various models fit the categories assigned by the subjective evaluation, there must be agreement between the subjective and objective assessments. When the objective prediction falls outside the expert's designated class, there is a discrepancy between the two evaluations. The mean $\pm$ standard deviation of the percentage of agreement between subjective and objective analysis is $76.6 \pm 0.8\%$, with ResNet-101 achieving a low value of 75.5% without contrast augmentation and a maximum value of 77.7% with contrast augmentation.
Figure 44 displays the results from MRIQC. It is crucial to reiterate that MRIQC is a toolkit that includes many image quality criteria and offers a thorough analysis of the scans. Only 12 of the entire 36 scans were processed, mostly because the clinical scans did not meet the MRIQC's requirements for T1w or T2w acquisitions. For CNR, CJV, EFC, and QI, respectively, the rates of agreement between the selected MRIQC metrics and the SIQA scores were 17%, 17%, 33%, and 75%.

5.1.2 *Discussion*

While tackling the SSIM prediction problem, the trained models performed quite similarly. Yet, when combined with contrast enhancement, both ResNet-18 and ResNet-101 models demonstrated a noticeable improvement. Contrast augmentation, as seen in the residuals distributions of the errors for both models, is what caused the means for ResNet-18 and ResNet-101 to be closer to zero and the standard deviations to drop by $\approx$1.5 and $\approx$1.44 times, respectively.
The scatter plots, where the dispersion level is clearly lower when contrast augmentation is applied, also show a drop in the standard deviations. The first thing to note when looking at the classification task is that the accuracy decreases linearly with the number of classes, from 97 to 95 to 89%. This can be explained by the fact that each model has a harder time classifying an image into the correct predefined range of SSIM values as the number of classes grows. The confusion matrices support this behaviour by showing an increase in the out-of-diagonal values, i.e., when using ResNet-18 without contrast augmentation, the maximum out-of-diagonal value for the classification task with three classes is 0.04 (for class-2 and class-3), and when using ResNet-18 with ten classes, the maximum value is 0.50 (for class-1). This suggests that the ResNet-18 classifies 50% of the examined

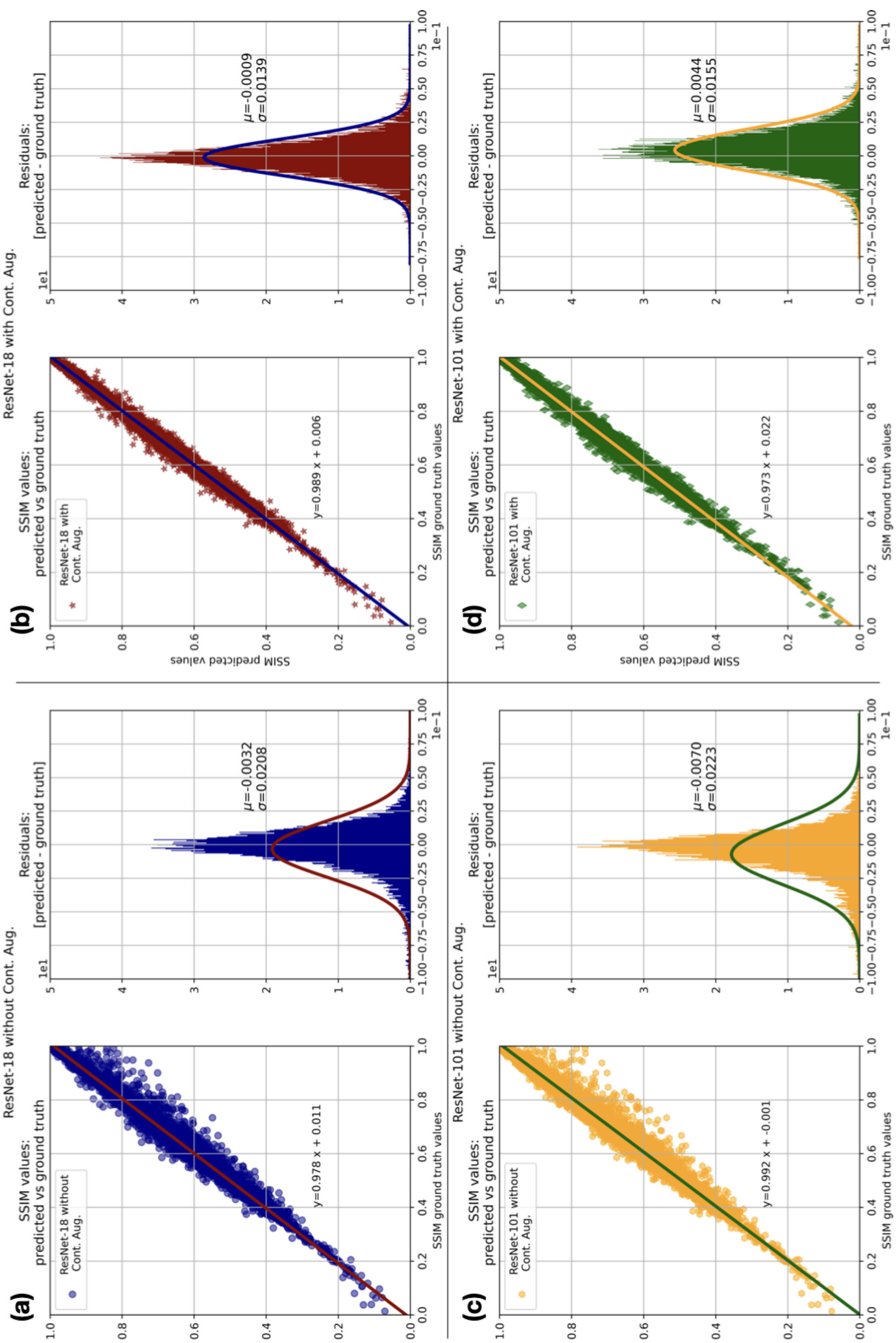

Figure 41: Scatter plot SSIM predicted against ground truth values and Residuals distribution for (a) ResNet-18 without contrast augmentation, (b) ResNet-18 with contrast augmentation, (c) ResNet-101 without contrast augmentation and (d) ResNet-101 with contrast augmentation.

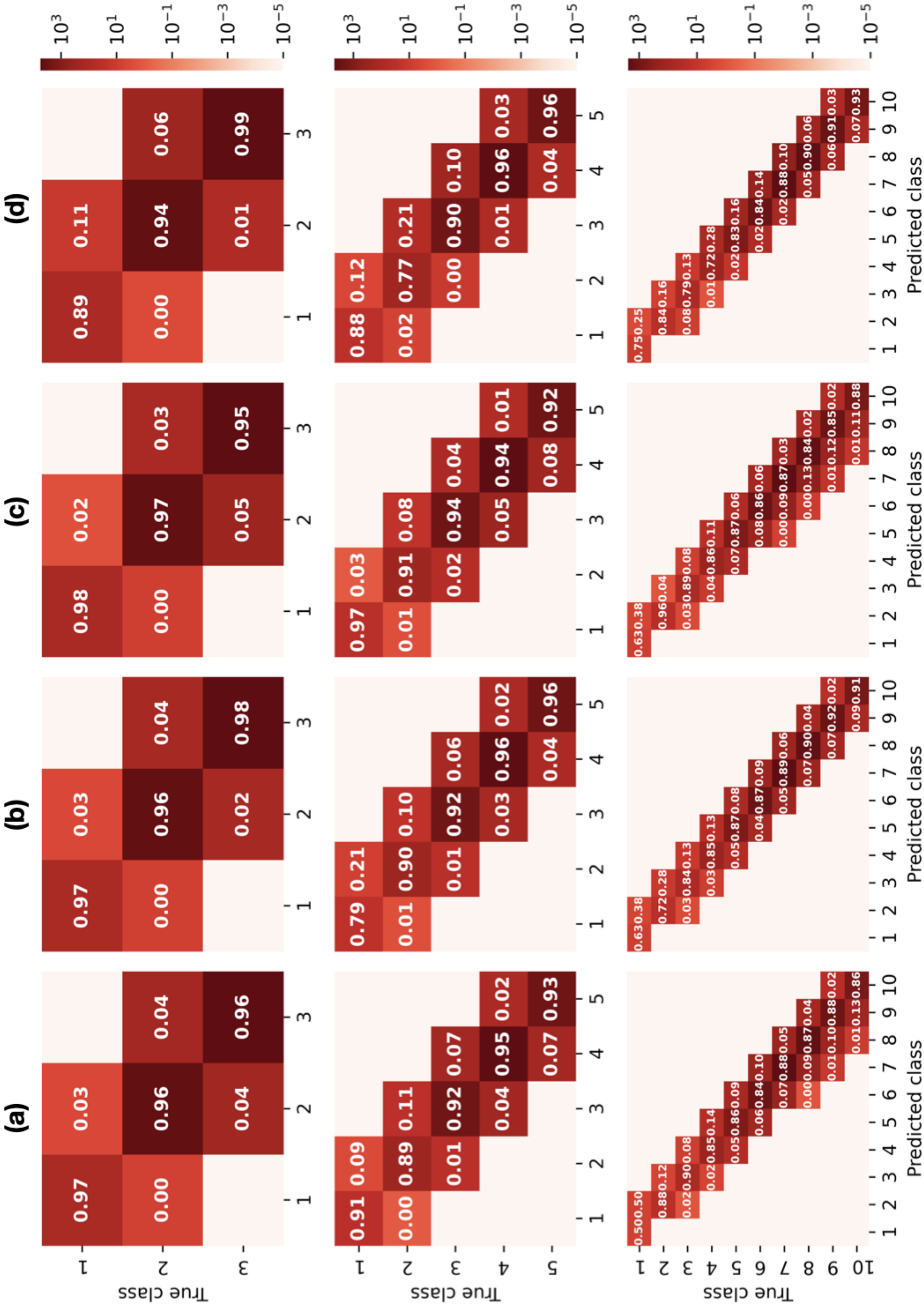

Figure 42: Confusion matrices for the classification task. First row 3 classes case, second row 5 classes and third row 10 classes. The columns are for **(a)** ResNet-18 without contrast augmentation, **(b)** ResNet-18 with contrast augmentation, **(c)** ResNet-101 without contrast augmentation, **(d)** ResNet-101 with contrast augmentation, respectively.

Table 10: Results for the classification task. The classification task has been performed three times, considering 3,5 and 10 classes, respectively. "Prec." is the abbreviation of the term precision, while "macro avg" corresponds to macro average and "weight. avg" to the weighted average calculated using the python package scikit-learn [203]. **(a)** is for ResNet-18 without contrast augmentation, **(a)** is for ResNet-18 with contrast augmentation, **(c)** is for ResNet-101 without contrast augmentation, **(c)** is for ResNet-101 with contrast augmentation.

	(a)			**(b)**			**(c)**			**(d)**			
Class	Prec.	Rec.	f1-sc.	Prec.	Rec.	f1-sc.	Prec.	Rec.	f1-sc.	Prec.	Rec.	f1-sc.	#
1	0.94	0.97	0.95	0.93	0.97	0.95	0.93	0.98	0.96	0.97	0.89	0.93	117
2	0.95	0.96	0.95	0.97	0.96	0.96	0.94	0.97	0.95	0.98	0.94	0.96	4307
3	0.97	0.96	0.97	0.97	0.98	0.97	0.98	0.95	0.96	0.95	0.99	0.97	5576
acc.			0.96			**0.97**			0.96			0.96	10000
m.avg.	0.95	0.95	0.96	0.96	0.97	0.96	0.95	0.97	0.96	0.97	0.94	0.95	10000
w.avg	0.96	0.96	0.96	0.97	0.97	0.97	0.96	0.96	0.96	0.96	0.96	0.96	10000
1	0.97	0.91	0.94	0.93	0.79	0.85	0.94	0.97	0.96	0.85	0.88	0.87	33
2	0.86	0.89	0.88	0.85	0.90	0.87	0.83	0.91	0.87	0.93	0.77	0.84	262
3	0.91	0.92	0.91	0.93	0.92	0.93	0.89	0.94	0.91	0.94	0.90	0.92	2320
4	0.94	0.95	0.94	0.95	0.96	0.96	0.94	0.94	0.94	0.94	0.96	0.95	5021
5	0.96	0.93	0.95	0.96	0.96	0.96	0.97	0.92	0.95	0.95	0.96	0.96	2364
acc.			0.93			**0.95**			0.93			0.94	10000
m.avg.	0.93	0.92	0.92	0.93	0.91	0.91	0.91	0.93	0.92	0.92	0.89	0.91	10000
w.avg	0.93	0.93	0.93	0.95	0.95	0.95	0.93	0.93	0.93	0.94	0.94	0.94	10000
1	1.00	0.50	0.67	1.00	0.62	0.77	1.00	0.62	0.77	1.00	0.75	0.86	8
2	0.81	0.88	0.85	0.78	0.72	0.75	0.83	0.96	0.89	0.75	0.84	0.79	25
3	0.90	0.90	0.90	0.81	0.84	0.83	0.87	0.89	0.88	0.91	0.79	0.84	62
4	0.81	0.84	0.83	0.80	0.85	0.83	0.76	0.85	0.80	0.88	0.71	0.79	200
5	0.82	0.86	0.84	0.86	0.87	0.87	0.79	0.87	0.83	0.86	0.83	0.84	689
6	0.84	0.84	0.84	0.89	0.87	0.88	0.83	0.86	0.84	0.89	0.84	0.86	1631
7	0.86	0.88	0.87	0.89	0.89	0.89	0.85	0.87	0.86	0.88	0.88	0.88	2706
8	0.87	0.87	0.87	0.89	0.90	0.89	0.88	0.84	0.86	0.86	0.90	0.88	2315
9	0.86	0.88	0.87	0.89	0.92	0.90	0.89	0.85	0.87	0.87	0.91	0.89	1456
10	0.97	0.86	0.91	0.97	0.91	0.94	0.96	0.88	0.91	0.95	0.93	0.94	908
acc.			0.87			**0.89**			0.86			0.88	10000
m.avg.	0.88	0.83	0.84	0.88	0.84	0.85	0.86	0.85	0.85	0.88	0.84	0.86	10000
w.avg.	0.87	0.87	0.87	0.89	0.89	0.89	0.86	0.86	0.86	0.88	0.88	0.88	10000

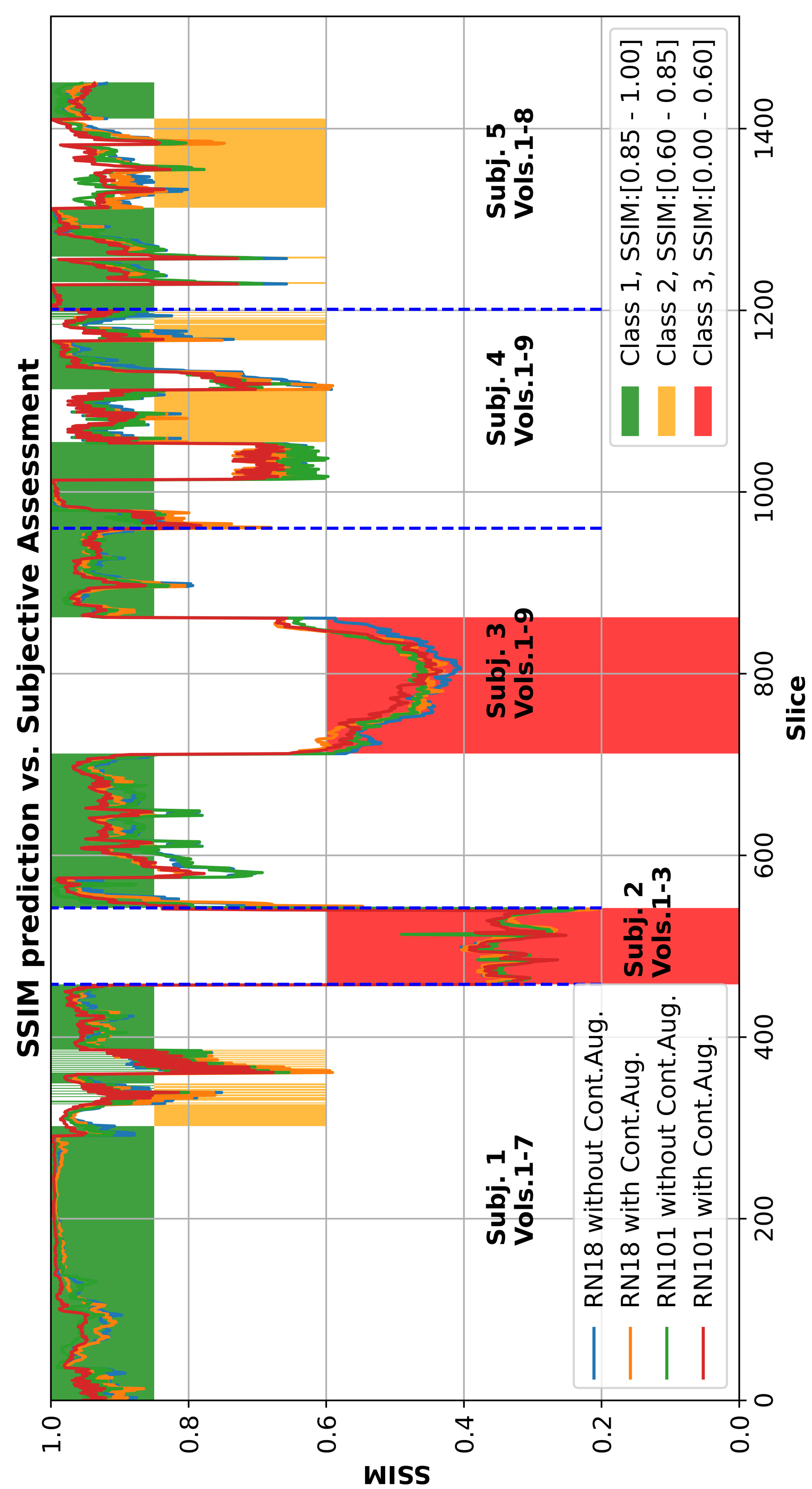

Figure 43: Evaluation for the clinical dataset. The curves represent the SSIM predictions obtained with the different trained models, while the coloured bars show the subjective classification performed by the expert. When the curves are within the coloured bars, there is an agreement between the objective and subjective evaluation, disagreement otherwise. The blue dashed lines indicate the separation between the different subjects. On the x-axis, there is the slice number; all the volumes were stacked consecutively one after another.

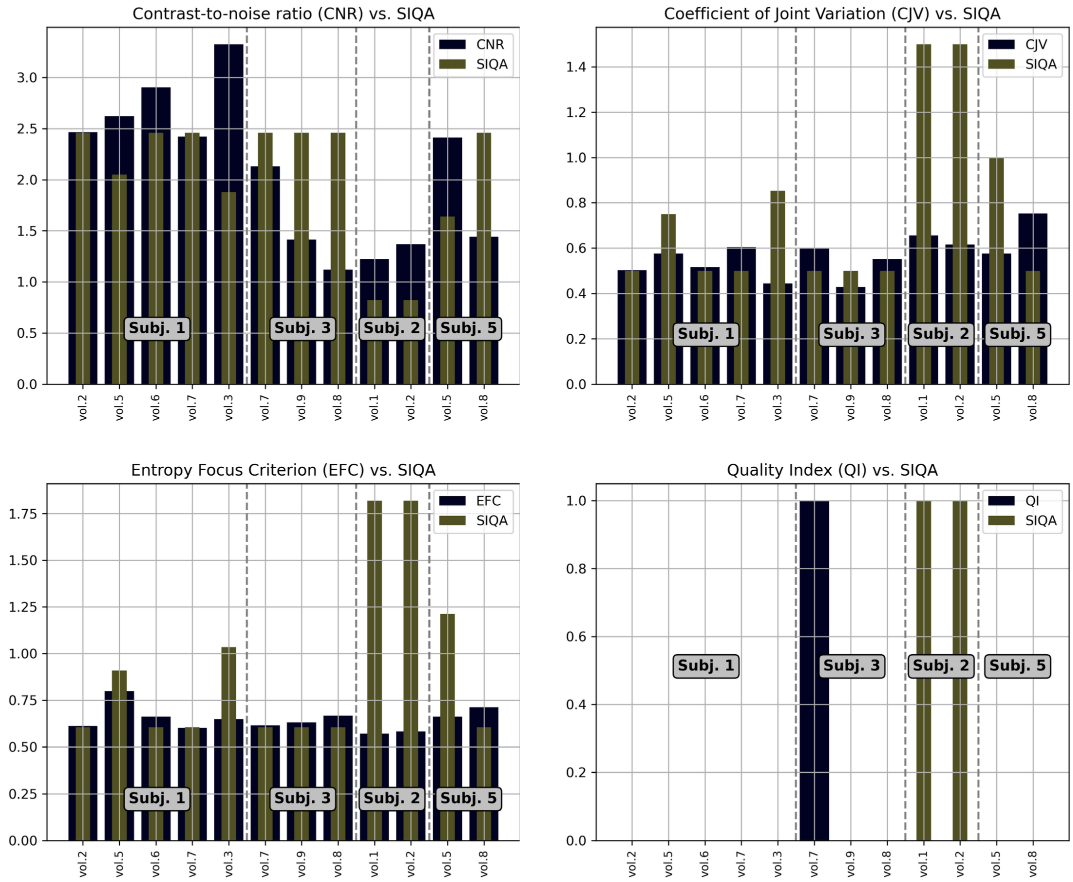

Figure 44: MRIQC results. Top left: CNR; top right: CJV; bottom left: EFC, and bottom right: QI.

images erroneously when conducting the 10-class classification challenge without using contrast enhancement. When contrast augmentation is used, there appears to be a decrease in class-1 images that were incorrectly classified. Figure 42 shows a general trend in this direction, but there are also results that are in conflict with it. For example, when looking at the 5-class classification task for class-1 while always taking ResNet-18 without and with contrast augmentation, there is a net increase in class-1 images that have been incorrectly classified, going from 9 to 21% of the tested images.

A maximum agreement rate of 77.7% between the objective and subjective judgements was achieved in the final application using clinical data, which also produced satisfactory results. Due to the different subjective schemes chosen, it is not possible to directly compare this work to the prior three-class categorisation task (section 5.1). When the trained models are applied to clinical data, there is a noticeable decline in performance, but this can be explained by a number of variables. First of all, the clinical data sample included types of image data—such as diffusion acquisition and derived diffusion maps—that the models had never seen during the training phase. Secondly, the motion artefacts that were artificially generated did not cover all of the potential motion artefacts that might appear in an authentically MR motion-corrupted image. New contrasts, various resolutions, and other orientations can be added to the training set to see whether they produce any improvements. Oblique acquisitions, for instance, weren't taken into account in this work. The artificial corruption techniques utilised in this work can also be enhanced further. For instance, corruption algorithms based on motion log data captured by a tracking device, as is frequently done for PMC [204, 205], could be used. However, this would require the availability of raw MR data, and it must also be considered that de-correcting the images will take longer to compute than the present methods.

The bias that each expert introduces while assessing the image quality is another consideration for the subjective assessment. The expert's opinion of image quality is accurately replicated in this study ($76.6 \pm 0.8\%$), but it cannot be used as a standard reference. There will always be disparities between the experts, such as their years of experience or sensitivity to the presence of motion artefacts in the assessed image, even though the subjective assessment can be repeated with the assistance of other experts. It's also important to remember that the SSIM ranges for the three classes can be modified to fit a new scheme. This permitted an accurate computation of the SSIM values and made it easy to establish ranges that visually correspond with the scheme defined in section 5.1. In the scenario examined in this research, the scheme has been defined by using purposely distorted images and the corresponding ground truth images.

At least for three metrics–CNR, CJV, and EFC–the results of MRIQC appear to be less consistent with the SIQA. However, the rate agreement between the QI measure and SIQA is only 75%, and when just taking into account the scans examined by MRIQC, the rate agreement between the QI measure and our technique is similarly 75%.

Table 11: Comparison table: MRIQC (baseline) and ResNet models. [a]Hardware required for clinical data evaluation. † optional but highly recommended for training a new model. * Docker size. ** MRIQC could not process all the clinical image volumes, only the structural ones, T1w and T2w.

	MRIQC	ResNet models
Data preparation	Mandatory BIDs conversion	Any format can be used: DICOM, Nifti, etc.
RAM/ROM[a] required VRAM (on GPU) CPU[a] GPU[a]	49 GB / ≈ 16 GB* - AMD Ryzen 9 (boost up to 4.7GHz) Not required	4GB / ≈ 1 GB Intel® Core™ i7-8700K NVIDIA GeForce GTX 1080 Ti†
Time required (CPU) Time required (GPU)	15 minutes to assess 12 vol.** Not available	39.79 seconds for 36 vol. 8.84 seconds for 36 vol.
Type of images	only 3D T1w, T2w and fMRI	ALL (2D and 3D)
Dependencies	FSL[b], ANTs[c], AFNI[d], FreeSurfer[e], etc. Docker[g] alternative is available	Python, PyTorch[f]
Image Quality Metrics	Multiple (CNR, CJV, EFC, etc.)	Single

[b] https://fsl.fmrib.ox.ac.uk/fsl/fslwiki/
[c] http://stnava.github.io/ANTs/
[d] https://afni.nimh.nih.gov/
[e] https://surfer.nmr.mgh.harvard.edu/
[f] https://pytorch.org/
[g] https://hub.docker.com/r/poldracklab/mriqc/

5.1.3 *Conclusion*

In order to make ResNet models more robust to variations in image contrast in clinical contexts, this research provides an SSIM-regression-based IQA technique. Without using the ground truth (motion-free) images, the approach was able to accurately estimate the SSIM values from artificially motion-corrupted images (residual SSIMs as low as -0.0009 ± 0.0139).
Also, the motion classes derived from the anticipated SSIMs were extremely accurate, with the ten classes scenario reporting a maximum weighted accuracy of 89% and the three classes scenario reporting a maximum accuracy value of 97%.
The results are really encouraging, especially when taking into account how difficult it is to quantify the degree of image deterioration caused by motion artefacts and how different types of contrast, resolution, etc., might be. Clinical data will undergo additional assessments, including numerous subjective assessments, to determine its clinical usefulness and robustness against changes in real-world sce-

narios.
Also, additional training will be conducted in order to have a greater variety of images, including Time-of-Flight imaging and diffusion-weighted imaging, which are typical clinical acquisitions. It would also be advantageous to include images acquired at lower magnetic fields ($\leqslant$ 1.5 T).
Given the results that ResNet models obtained in this study, it makes sense to assume that future research can also be directed at a different anatomical body area, concentrating, for example, on the stomach or cardiac imaging.
However, the success of deep learning models trained to have a reference-less image quality assessment tool depends significantly on the reproduction of real-looking-like motion artefacts.

5.2 PRIOR-ASSISTED RETROSPECTIVE MOTION CORRECTION

This work entitled "Retrospective Motion Correction of MR Images using Prior-Assisted Deep Learning" [110] was presented at the 34th Conference on Neural Information Processing Systems (NeurIPS 2020), Vancouver, Canada.

Data Preparation

In this work, 100 participants' T_1, T_2, and PD images (for training, testing, and validation, respectively) from the openly accessible IXI Dataset[4] were employed. A modified version of TorchIO's RandomMotion transformation was used to artificially introduce motion corruption into T2-weighted pictures [155](v0.17.45). In the initial stage of the experiments, 10 simulated movements with a rotation ranging from -1.75 to +1.75 degrees without any translation were carried out. This modified version of the RandomMotion function randomly conducted either X- or Y-directional in-plane motion corruption.

Image Priors

Deep learning models may perform better when additional images are provided as prior knowledge in addition to the corrupted image [206, 207]. In this study, experiments were carried out utilising slices from separate subjects that were similar in terms of MRI contrast and slices from the same subject that were different in terms of MRI contrast.

- Similar slices: ten similar (same slice position) slices with the same MRI contrast were randomly selected from among different subjects and provided as previously along with the motion-corrupted image during the motion correction. This kind of prior is motivated by the fact that it makes it simple to access images with the same contrast but different subjects that have not

4 Dataset available at: https://brain-development.org/ixi-dataset/

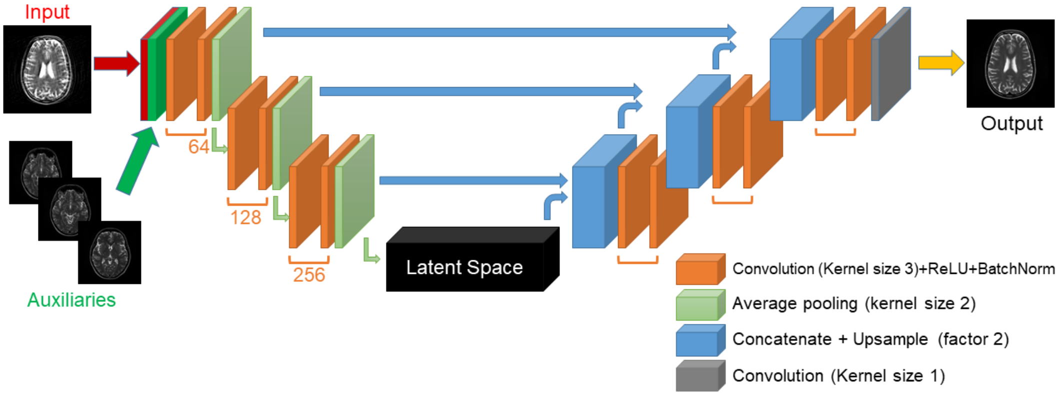

Figure 45: Modified U-Net architecture for supplying priors

been distorted by motion when doing motion correction on a particular image. Only T_2-weighted images from the IXI Dataset were used in these tests.

- Different Contrasts: often, many contrasts of the same individual are collected during regular clinical acquisitions. If one of the different contrasts is distorted by motion, the other contrasts of the same subject can be used to restore the original image. The IXI Dataset's three accessible contrasts were co-registered with the T_2-weighted images. T_1 and PD images were used as priors during the correction process after T_2-weigthed images had been corrupted.

Network Architectures

The baselines for this work were a modified version of the ReconResNet [208] and U-Net [166]. The basic networks have been modified to enable prior reception. Schematics diagram of the modified archiectures are shown in figures 45 and 46, for U-Net and ReconResNet

There were two prior-supply techniques that were tested.

- Multi-Channel Network: concatenated on the channel dimension, each motion-corrupted image and its corresponding priors were then sent to the network as a multi-channel input. In contrast to the multi-channel approach, where the models received $1 + n_{prior}$ channel images as input, the baselines only received one channel image as input.

- Dual-Branch Network: by adding an additional branch to the baselines for the priors, modified versions of the baselines for this technique were made. The motion-corrupted image was sent to the main branch, while the priors were sent to the auxiliary branch. Except for the quantity of input channels, the contraction path and latent space of the auxiliary branch for the U-Net were identical. The network's main branch was the lone source of the skip-connections; the auxiliary branch did not provide any skip-connections.

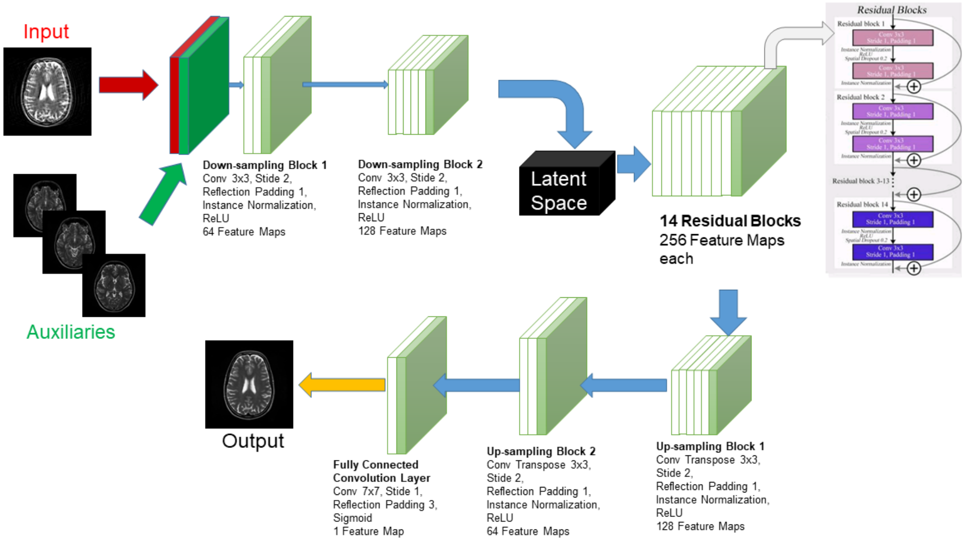

Figure 46: Modified ReconResNet architecture for supplying priors

The ReconResNet's auxiliary branch, up until the residual blocks, was exactly like the ReconResNet's downsampling blocks with the exception of the number of input channels. The main branch and the auxiliary branch produced two distinct latent space representations for both network models. To create the final result, these latent representations were integrated and sent. To create the final combined latent space, two different approaches to merging the latent spaces were taken into consideration: simple addition and concatenation and convolution with a kernel size of one. The U-Net's growth path received this combined latent space. This latent representation was delivered to the residual blocks for additional processing in the case of ReconResNet.

Results and Discussions

Figure 47 displays the effectiveness of the various techniques based on the values from SSIM, and Figure 48 displays a typical example outcome. It was found that providing ten identical slices of the same contrast but of different participants did not improve the motion correction between the two distinct forms of priors. Yet, for the majority of the experiments, providing varied contrasts of the same subject considerably enhanced the motion correction. Both the multi-channel and dual-branch prior supply approaches performed better than ReconResNet. However, only the multi-channel strategy has significantly improved for U-Net.

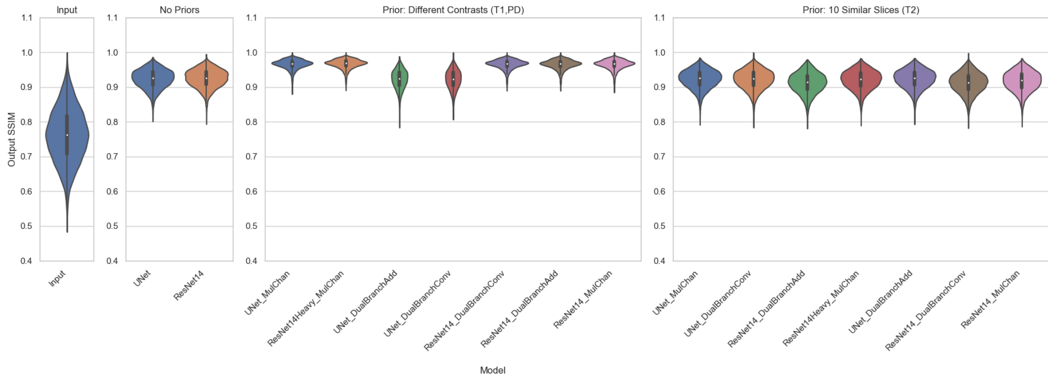

Figure 47: Plots showing the performance of the various methods, based on SSIM

Conclusion

This study explores of the efficacy of using image priors to enhance the performance of deep learning-based motion correction in MRI imaging. The experiments were structured around the introduction of artificial motion corruption into T2-weighted images and the subsequent application of various deep learning strategies to rectify the corruption. Two approaches for supplying image priors to networks were explored here: the multi-channel technique and the dual-branch network. The findings delineate a clear advantage in supplying additional contrast images from the same subject over merely providing similar slices from different subjects. These results demonstrate the potential value of integrating multiple contrasts during clinical imaging acquisitions, as they can be instrumental in rectifying motion distortions in particular contrasts.

From a network architecture perspective, both the multi-channel and dual-branch approaches showed significant improvements for ReconResNet over its baseline. However, in the case of U-Net, only the multi-channel strategy emerged as significantly superior to its baseline. The lack of skip connections from the auxiliary branch may have been the cause of the failure, but the skip connections will make it more akin to the multi-channel technique. This research elucidates the potential advantages of leveraging additional image contrasts for motion correction in MRI imaging.

As future works, a deeper dive into the dual-branch approach can be taken, especially examining the role and impact of skip connections. Additionally, expanding the dataset or introducing different types of motion corruption could provide further insights into the robustness and generalisability of the proposed methods.

5.3 Generalised RMC using deep learning, with the help of contrast augmentation

The earlier presented method (section 5.2) showed significant improvements in terms of image quality. But the method requires image priors - which can be con-

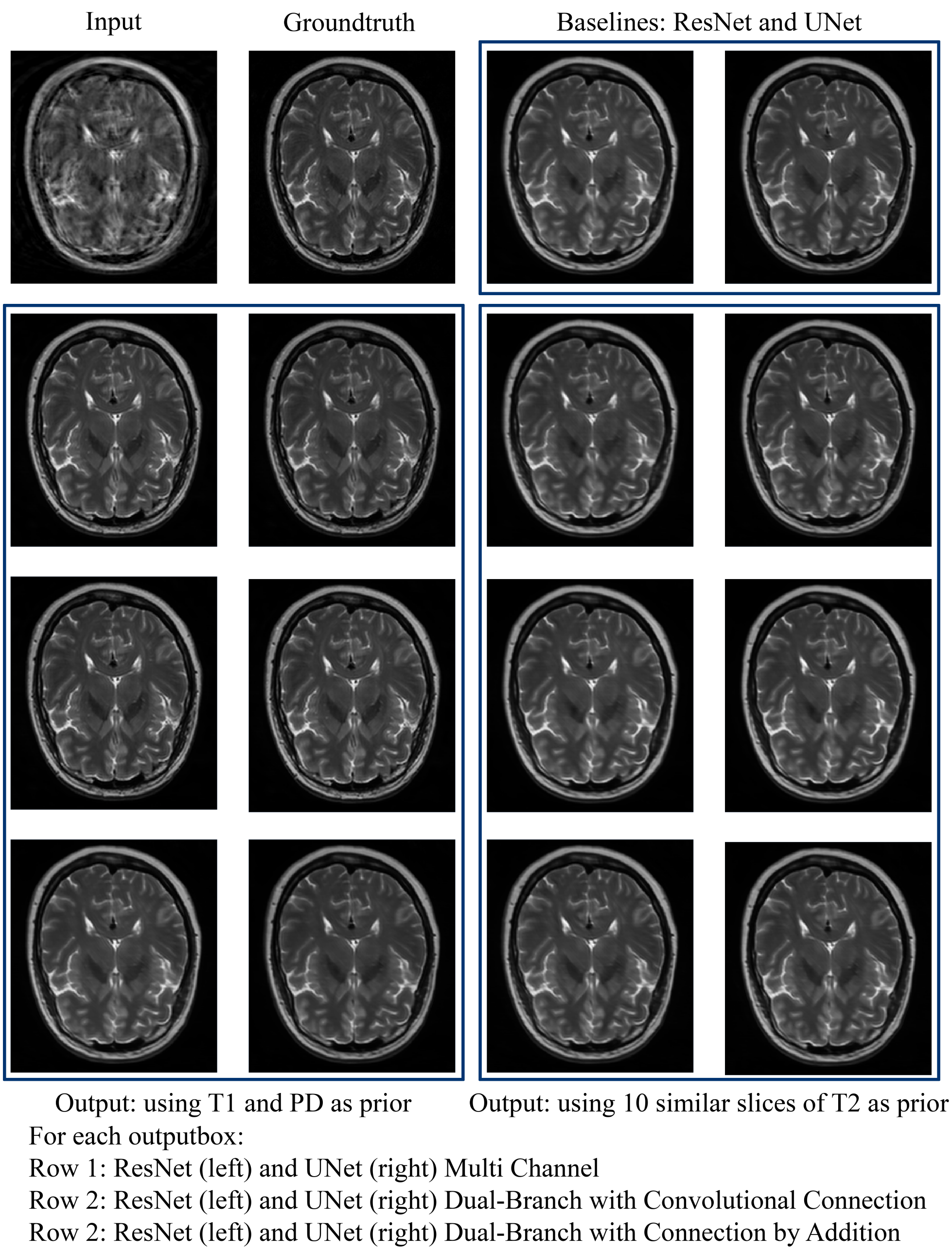

Figure 48: One example slice to show the motion correction performance of the various methods

sidered as a limiting factor as such image priors might not be also available. For the same, it is essential to develop a generalisable method, that can be applied to wide range of MRI contrasts and resolutions. This research introduces a deep learning based method tailored for RMC in MRI - using the ReconResNet [208] model, combined with a novel set of contrast augmentation and artificial motion corruption techniques. This work aims to propose a method that can generalise well to different MRI contrasts and levels of artefacts.

5.3.1 *Methods*

5.3.1.1 *Data*

The data used for this work were collected at 3 and 7 T (see section 4 for 7T) MRI Siemens scanners. More information regarding the data (in terms of MR contrast, matrix size, and image resolution) are provided in Table 12. For training, validation and testing 600, 160 and 158 image volumes were randomly selected, respectively. Further counts of different MR contrasts are provided in Table 13. For each volume only the slices containing brain tissues were taken into consideration.

Data Processing

Given a 3D volume from the dataset, a random slice is chosen during each training, validation, and testing step. Initially, the noise from the image was removed - by removing values smaller than 0.025, and then the slice was re-normalised using Min-Max normalisation. Then the slice was padded and resized to 256x256. Afterwards, contrast augmentation (see section 5.1) was applied with a probability of 75% - randomly choosing one of the methods listed in Table 14. Afterwards, the slice was re-normalised using Min-Max normalisation before feeding it to the artificial motion corruption algorithm.

Motion Corruption

Two different types of artificial motion corruption techniques were used - to help the model generalise better. During each iteration, either one of these techniques was applied to the slice. The first type of motion corruption uses the random ghosting and random motion functions from TorchIO [155], following the parameters listed in Table 15. For each slice during training and inference, these values were randomly chosen.

The second motion corruption method was created in-house (see section 5.1) - to simulate the real-world motion corruption in MRI. This method aims to create the artefacts as close to the real-world corruption as possible. First, the axis of the corruption and a floating-point σ between 0 and 3 for the intensity of the corruption are randomly chosen for each slice from a uniform distribution. Then, for each line along the chosen axis, the input slice rotated with an angle randomly chosen among $-\sigma$, 0, and σ. Then, the rotated slice is brought to the Fourier space

Table 12: Data regarding the Dataset

	Matrix Size			Resolution		
	x	y	z	res. x (mm)	res. y (mm)	slice (mm)
			T_1-weighted			
min	176.00	224.00	100.00	0.90	0.90	0.90
max	496.00	496.00	200.00	1.00	1.00	1.00
std	94.88	92.56	32.86	0.05	0.05	0.05
			T_2-weighted			
min	192.00	224.00	15.00	0.28	0.28	0.70
max	690.00	704.00	150.00	1.00	1.00	1.50
std	131.34	137.55	44.90	0.22	0.22	0.27
			T_2^*-weighted			
min	336.00	448.00	30.00	0.25	0.25	2.10
max	672.00	896.00	30.00	0.50	0.50	2.10
std	139.96	186.62	0.00	0.10	0.10	0.00
			PD-weighted			
min	336.00	448.00	15.00	0.28	0.28	1.20
max	690.00	704.00	95.00	0.50	0.50	1.50
std	167.63	121.23	33.15	0.10	0.10	0.14
			FLAIR			
min	176.00	224.00	120.00	0.70	0.70	0.70
max	320.00	320.00	150.00	0.90	0.90	0.90
std	56.97	35.91	15.05	0.10	0.10	0.10

Table 13: Number of samples of different MR contrasts

	T_1-w	T_2-w	T_2^*-w	PD	FLAIR	Total
Training						
samples	182	176	49	55	138	600
Validation						
samples	46	44	21	17	32	160
Testing						
samples	44	40	28	15	31	158

Table 14: Contrast augmentation parameters

Function	**Parameter**	**Value (Random)**
Gamma Correction	Gamma	Float between 0.75 and 1.75
CLAHE	Kernel	Integer between 25 and 100
	Clip limit	0.01
	Number of bins	512
Sigmoid Correction	Cutoff	Float between 0.01 and 0.75
	Gain	Integer beween 1 and 4
Logarithmic correction	Gain	Float between -0.5 and 0.5

Table 15: TorchIO ghosting and motion parameters (Default values were used for the rest of the parameters)

Function	Parameter	Value (Random)
RandomGhosting	Number of Ghosts	Integer between 3 and 7
	Axis	0 or 1
	Intensity of the ghosts	Float between 0.05 and 1.0
	k-space centre to restore	Float between 0.01 and 1.0
RandomMotion	Degree	Float between 0.01 and 10.0
	Translation	Float between 0.01 and 10.0
	Number of movements	Integer between 2 and 10

or k-space by applying 2D Fourier transform to the rotated image and then taking only the selected line. All the k-space lines were stacked together and undergo an inverse 2D Fourier transform, generating the motion-corrupted image, which is then normalised to confine its values between 0 and 1.

5.3.1.2 *Model and Training*

This research uses a deeper version of the ReconResNet model [208] - starting with 64 feature maps, two downsampling blocks, followed by 56 residual blocks, two upsampling blocks using transposed convolution operations, and finally a 1x1 convolution layer to merge all 64 output feature maps into one, followed by sigmoid as the final activation - to obtain the final output. The network uses PReLU as activation functions and instance normalisation layers within its blocks. Between each pair of residual blocks, a 2D spatial dropout layer with a probability of 20% was added to avoid overfitting. Apart from the number of residual blocks, the architecture is similar to the original ReconResNet model.

The loss between the model's prediction and the ground-truth was calculated using a perceptual loss function, which is commonly used in image generation tasks to ensure that the generated images not only have pixel-wise accuracy but also maintain perceptual quality. A frozen pretrained 2D ResNeXt 101 model, trained for the task of motion corruption classification, was used as the perceptual loss network (PLN) - to extract features from the prediction and ground-truth. The extracted features from different levels of the PLN were compared using L1 loss. The loss was optimised using the Adam optimiser with a learning rate of $3x10^{-4}$ and a batch size of 1, for 2000 epochs with the help of automatic mixed precision. In the end, the model state resulting in the lowest validation loss was chosen as the final model and was used for inference.

5.3.2 *Results and Discussion*

10 random slices from each test volume were artificially corrupted using the above mentioned corruption methods 10 times - to obtain 10 sets of results containing different sets of slices and corruptions. The average SSIM value of the corrupted images across all 10 experiments were 0.688 0.152 and the model managed to improve them to 0.886 0.081, resulting in an average improvement of 0.198 0.131. Moreover, the corrupted images had a minimum SSIM of 0.050 and a maximum of 1.000, while the corrected images had scores between 0.322 and 0.998, and the resulting improvements were between 0.320 and 0.949 while the distribution of the improvements is centred around 0.2. By taking a closer look at the results, one can observe that the variability of improvements within each of the 10 sets is relatively consistent, hovering around a standard deviation of 0.13. Meanwhile, the variability between the average improvements of different sets is quite low (0.0077), indicating that the model's performance is consistent across different experimental runs. Fig. 49 shows a clearer idea about the distribution of the results. Subplot in

top left shows the the distribution of the SSIM values for the corrupted and corrected images, in red and green, respectively, while being compared against the ground-truth (uncorrupted) images. A clear improvement in terms of the image quality can be observed here. The next subplot, on the top right corner, shows the distribution of the improvements in terms of the SSIM values - as mentioned earlier, it's centred around 0.2. The third subplot (centre row) shows the change in SSIM values - from corrupted to corrected and the final subplot (bottom row) shows the difference of SSIM values between the corrupted and corrected images. The length of the bars indicate the range of change, while blue signifies a positive improvement and red signifies negative. It can be observed that in most cases there is an increase of SSIM values. However, in some cases there is a decrease in terms of the SSIMs. This decrease can mainly be observed for input images with already high SSIM values (i.e. less to no corruption). The number of images for which the SSIM values decreased after processing is way less than the number of improved images, while also the amount of decrease is not much (as can be observed from the second subplot). Figure-50 presents qualitative results of this proposed motion correction technique. It can be said that it would be useful to first use some kind of image quality assessment tool (e.g. Reference-less SSIM Regression for Detection and Quantification of Motion Artefacts, see section 5.1) to evaluate the images and only supply them to the neural network model if required. The final subplot (bottom row) shows the difference of SSIM values between the corrupted and corrected images - where blue and red signify positive and negative difference, respectively. All these results discussed here demonstrate a clear improvement in terms of the image quality, as well as a wide-applicability and stability across different amount of corruption and different image contrasts. Finally, examples of

5.3.3 *Conclusion and Future Work*

This study presents a deep learning based retrospective motion correction technique that hinges on the utilisation of the ReconResNet model, enhanced through the integration of custom contrast augmentation and artificial motion corruption techniques. This approach was meticulously crafted to ensure broad generalisation across various MRI contrasts and degrees of artefacts. The results presented here demonstrate a notable enhancement in image quality, evidenced by the improvement in SSIM values from an average of 0.688 to 0.886. Moreover, the consistency in results across different experimental iterations underlines the robustness and reliability of our model, marking a significant stride in the quest to mitigate motion-related distortions in MRI images. Notwithstanding its achievements, the model did exhibit minor declines in SSIM for already high-quality input images - an observation hints at the potential value of incorporating an initial image quality assessment phase to discern and process only those images that truly necessitate correction. The broader implications of this research could pave the way for more reliable and clearer imaging in the realm of MRI, fostering advancements in medical diagnostics and therapeutic interventions. Future works might focus on the

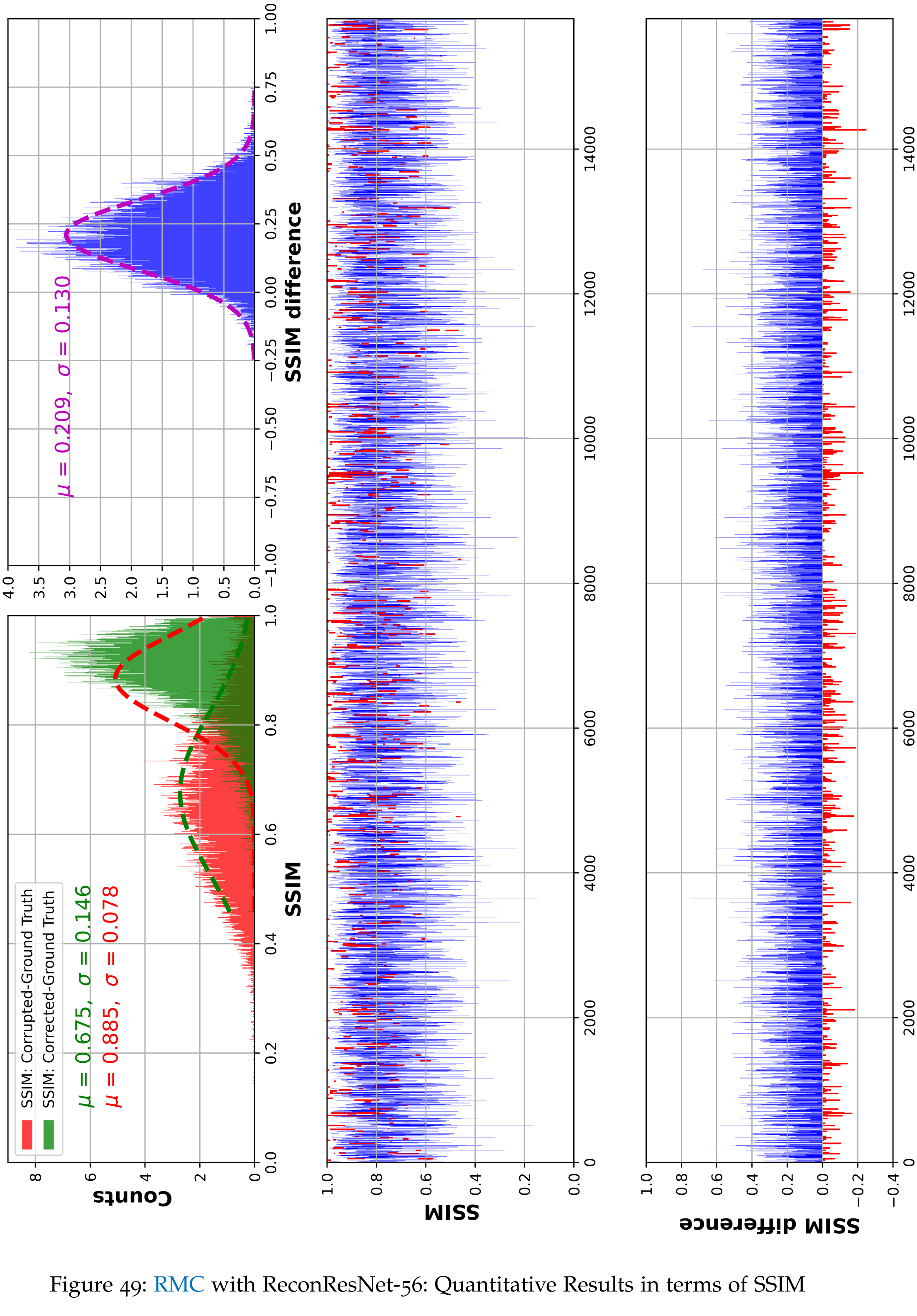

Figure 49: RMC with ReconResNet-56: Quantitative Results in terms of SSIM

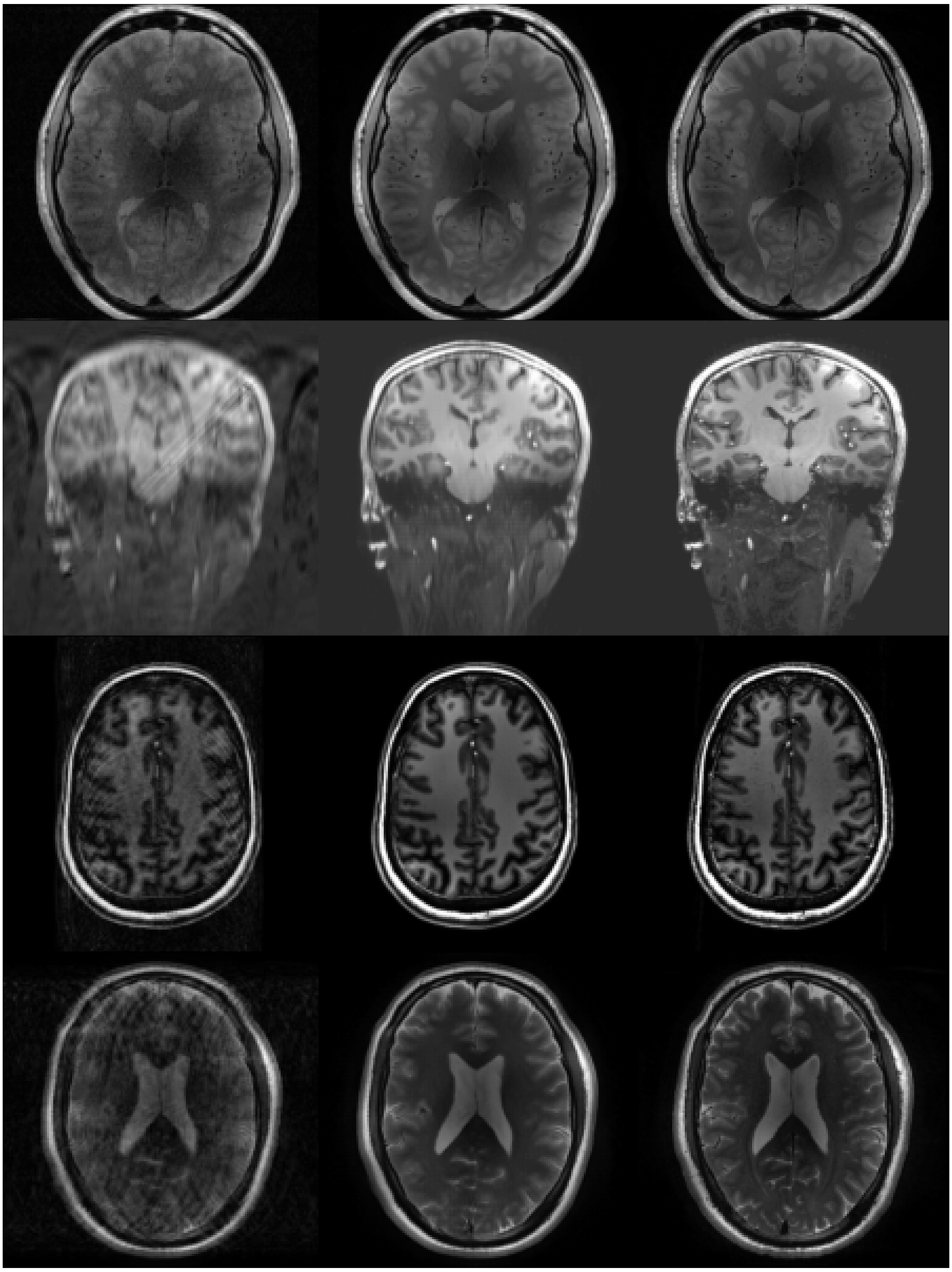

Figure 50: Qualitative Results, four slices resulted in improvements close to the median improvement. From left to right: corrupted, corrected, ground-truth. From top to bottom: PD-w Axial, T_1-w Coronal, T_1-w Axial, T_2-w Axial.

until now unexplored field of combining prospective motion correction and deep learning based retrospective motion correction - by supplying images corrected with PMC that could not reach acceptable image quality with PMC only.

Part V

CONCLUSION

6 CONCLUSION AND OPEN QUESTIONS

6.1 CONCLUDING REMARKS

This thesis presented various ways of combating the challenge of motion artefacts in MRI. The contributions and the findings of this thesis can be categorised into two categories - PMC and RMC.

Chapter 4 presented a large scale study on PMC - to systematically evaluate high-resolution MRIs at 7T in cooperative subjects. A substantial number of the acquired images showed very high or high image quality. With PMC ON, all of the scenarios improved according to subjective evaluation, but only three of them were statistically significant. For five of the six groups, objective measures have demonstrated that the images obtained with PMC were of higher image quality; however, for the sixth group, the metrics did not agree on a clear winner and did not accord with the subjective metric. In this research, only the images with comparable motion patterns for PMC ON and OFF were taken into account. In this study, only images with comparable PMC ON and OFF motion patterns were considered. Therefore, the improvements observed can be credited to PMC. These results lead to the conclusion that "PMC" provides superior image quality for high-resolution images when there is no intentional motion and that it should be considered even when high-resolution scans at 7T are acquired from healthy compliant subjects.

The next set of contributions are in terms of RMC, to be precise, data-driven RMC with the help of deep learning, and they are presented in Chapter 5. This chapter present three methods in this context. The first method, in Sec. 5.1, presents a novel SSIM-regression-based IQA technique. The method successfully estimated the SSIM values from artificially motion-corrupted pictures without using the ground truth (motion-free) MRIs (residual SSIMs as low as -0.0009 ± 0.0139). Additionally, the motion classes derived from the predicted SSIMs had a very high degree of accuracy, with the ten classes scenario reporting a maximum weighted accuracy of 89% and the three classes scenario reporting a maximum accuracy value of 97%. The findings are very encouraging, especially when one considers how challenging it is to determine the exact amount of image degradation brought on by motion artefacts, as well as how various types of contrast, resolution, etc. might be present in any evaluation scenario.

The following section, Sec. 5.2, presents a novel prior-assisted deep learning method to retrospectively correct MRIs corrupted by motion. The effectiveness of employing image priors to improve the efficiency of deep learning-based motion correction in MRI imaging is investigated in this work. The experiments were structured around the introduction of artificial motion corruption into T2-weighted images and the subsequent application of various deep learning strategies to rectify the corruption. Here, the multi-channel technique and the dual-branch network were investigated as two methods for delivering image priors to the network models. The findings delineate a clear advantage in supplying additional contrast images from the same subject over providing only similar slices from different subjects. From a network architecture perspective, both the multi-channel and dual-branch approaches showed significant improvements for ReconResNet over its baseline. However, in the case of U-Net, only the multi-channel strategy emerged as significantly superior to its baseline. The lack of skip connections from the auxiliary branch may have been the cause of the failure, but the skip connections will make it more akin to the multi-channel technique. This research elucidates the potential advantages of leveraging additional image contrasts for motion correction in MRI imaging.

The third and final section of this chapter, Sec. 5.3, presents yet another deep learning based method for motion correction, but this time, without any additional prior image. There might be scenarios when the image priors discussed earlier might not be available. For the same, it is essential to develop a generalisable method, that can be applied to wide range of MRI contrasts and resolutions. This was the exact aim of this work. The ReconResNet model, which is used in this work, is bolstered by the use of specific contrast augmentation and artificial motion corruption approaches. To guarantee broad generality across different MRI contrasts and levels of artefacts, this technique was carefully constructed. The results presented here demonstrate a notable enhancement in image quality, evidenced by the improvement in SSIM values, evidenced by the improvement in SSIM values from an average of 0.688 to 0.886, and results were consistent across several experimental iterations, highlighting the resilience and dependability of the model. Despite its positive outcomes, the model did show small reductions in SSIM for input images that were already of excellent quality. This finding suggests the potential benefit of integrating an initial image quality assessment step to identify the images that require correction and only supply them to this model. This can be achieved using the previously presented SSIM-regression method (Sec. 5.1). The larger ramifications of these results may pave the way for MRI imaging that is better in terms of image quality (e.g. lack of motion artefacts), enabling improvements in medical diagnosis and therapeutic treatments.

6.2 Summary of Contributions

The thesis makes significant contributions in terms of PMC and RMC. Firstly, it demonstrates the efficacy of PMC in improving high-resolution MRIs at 7 Tesla, particularly in "quasi no motion" scenarios (i.e. without intentional or extensive movements), thereby advocating its use in scans of healthy, compliant subjects. Secondly, the research introduces a novel SSIM-based IQA technique using deep learning to quantify the presence of motion artefacts in a given MRI by accurately estimating SSIM values in motion-corrupted MRIs without needing motion-free references. As part of this research, a new set of contrast augmentation techniques was developed - to make deep learning methods more robust against changes in MRI contrast, and also created an in-house motion simulation pipeline - to be able to create larger training datasets with motion artefacts resembling real-world motion in MRI. Finally, this thesis proposes a prior-assisted deep learning method for retrospectively correcting motion-degraded MRIs and proposes a generalisable deep learning-based method for RMC that is applicable across various MRI contrasts and resolutions, demonstrating significant improvements in image quality. In summary, this thesis presents different directions for quantifying and reducing motion artefacts in MRI, consequently improving the diagnostic reliability of the same.

6.3 LIMITATIONS

Even though this thesis presented a PMC and two RMC techniques, they come with certain limitations.

Some challenges or limitations of PMC in MRI are:
PMC requires a reliable and accurate motion tracking system that can measure head motion in six degrees of freedom (6-DOF) and communicate with the MRI scanner in real time [73].
The motion tracking system should also be compatible with MRI scanners, not interfere with image quality, and not cause discomfort or safety issues for the patient [73, 76, 80, 209].
PMC may not be able to correct for non-rigid effects, such as neck deformation or brain deformation, that can occur due to large or fast head movements. These effects can cause misalignment between the brain and skull or between different brain regions, which can affect image quality and data analysis [73].
PMC may introduce additional noise or artefacts into the images due to the rapid update of scan parameters based on head motion measurements. For example, PMC may cause eddy current effects, gradient delays, or radio-frequency interference that can distort image geometry or contrast [73].
PMC may not be compatible with some MRI sequences or protocols that require fixed scan parameters or specific timing conditions. For example, PMC may not work well with DWI, spectroscopy, parallel imaging, or multiband imaging [73, 210].

To summarise, prospective motion correction in MRI faces some challenges or limitations such as requiring a reliable and accurate motion tracking system, not correcting for non-rigid effects, introducing additional noise or artefacts, and not being compatible with some MRI sequences or protocols.

Deep learning is a powerful tool for motion correction in MRI, as it can learn from data and reconstruct realistic images without artefacts. However, deep learning also poses some challenges and limitations, such as the need for large and diverse datasets, the risk of altering or hiding anatomical features, and the lack of interpretability and robustness. Therefore, further research and evaluation are needed to ensure the clinical applicability and reliability of deep learning-based motion correction methods.

6.4 FUTURE RESEARCH DIRECTIONS

6.4.1 *Amalgamation of PMC and RMC with DL*

The amalgamation of PMC and RMC using deep learning is an unexplored research topic that aims to combine two different methods for reducing motion artefacts in MRIs. It might be possible to combine PMC and RMC to provide better motion correction outcomes than either method by itself. As an illustration, RMC can improve minor motion artefacts, whereas PMC can lessen large motion artefacts. Or, to help RMC operate better, PMC can give it motion data. This thesis proposed deep learning models to perform RMC. However, this topic is still under development, and there are many challenges and potentials for further improvement [211]. A possible way to combine both methods is shown in this pipeline:

1. image acquisition with the support of PMC;
2. image quality assessment through the proposed work of SSIM prediction (section 5);
3. image quality is sufficient to perform further analysis (e.g. brain extraction, tissue segmentation and so on), no further steps necessary;
4. image quality is not sufficient, and RMC can be applied to enhance it.

However, there are already other available approaches that combine PMC and non deep learning RMC techniques such as: the motion model approach, the Prospective Acquisition CorrEction (PACE) combined with Slice-to-Volume Registration (SVR) approach and the PMC combined with Iterative Reconstruction with Self-consistent phase correction (IRS) approach.

Motion model approach

This approach is based on the idea that the motion parameters estimated by the PMC system can be used to guide the RMC algorithm. However, the PMC system may not be able to correct for all types of motion, such as fast or unpredictable motion, or motion that occurs between the tracking device and the head. Therefore, some residual motion artefacts may still be present in the acquired data. To correct for these residual artefacts, the RMC algorithm uses the motion parameters from the PMC system as an initial guess and performs an optimisation process to refine them. The optimisation process involves minimising a cost function that measures the similarity between the acquired data and a reference image. The reference image can be either a pre-scan image or a reconstructed image from a subset of the data. By using the motion parameters from the PMC system as an initial guess, the RMC algorithm can reduce the search space and converge faster and more accurately to the optimal solution. This way, the image quality and accuracy are improved compared to using only prospective or retrospective motion correction alone. This approach has been tested on phantom and in vivo data and has shown promising results in reducing motion artefacts and improving image quality.

PACE with SVR

The second approach is based on the idea that different types of motion require different types of correction methods. The PACE and SVR approach uses two complementary methods to correct for motion in MRI: PACE is a technique that corrects for slow and gradual motion by measuring the head position of the subject in real-time and adjusting the imaging parameters accordingly. This way, the motion artefacts are reduced or avoided during the acquisition. Retrospective SVR is a technique that corrects for fast and abrupt motion by aligning the acquired slices to a reference volume after the acquisition. This way, the motion artefacts are corrected or reduced after the acquisition. The PACE and SVR approach combines these two methods in a sequential manner. First, the PACE technique is applied to correct for slow and gradual motion during the acquisition. Then, the SVR technique is applied to correct for fast and abrupt motion after the acquisition. By using this hybrid approach, the motion correction performance is improved compared to using only PACE or SVR alone. The PACE technique reduces the amount of motion that needs to be corrected by SVR, and the SVR technique compensates for the motion that PACE cannot correct. This way, the image quality and accuracy are improved, and the computational complexity and time are reduced. Also, this approach has shown promising results in reducing motion artefacts and improving image quality.

PMC with IRS

The idea behind this approach is that motion-induced phase errors can be corrected by using both prospective and retrospective methods. The PMC and IRS approach uses two complementary methods to correct for phase errors in spectroscopic imaging: PMC is a technique that reduces the phase errors caused by head motion by measuring the head position of the subject in real-time and adjusting the imaging parameters accordingly. This way, the phase errors are reduced or avoided during the acquisition. IRS is a technique that corrects the residual phase errors caused by eddy currents or other sources by using an iterative algorithm that estimates and corrects the phase errors from the acquired data. This way, the phase errors are corrected or reduced after the acquisition. The prospective motion correction and IRS approach combines these two methods in a sequential manner. First, the prospective motion correction technique is applied to reduce the motion-induced phase errors during the acquisition. Then, the IRS technique is applied to correct the residual phase errors after the acquisition. By using this hybrid approach, the phase correction performance is improved compared to using only PMC or IRS alone. The PMC technique reduces the amount of phase errors that need to be corrected by IRS, and the IRS technique compensates for the phase errors that PMC cannot correct. This way, the spectroscopic image quality and accuracy are improved, and the computational complexity and time are reduced. As for the other approaches, also this one has been tested on phantom and in vivo data and has shown promising results in reducing phase errors and improving spectroscopy acquisition.

PMC, then DL-based RMC

Deep Learning has been widely used in several fields these days, motion correction is no different. This thesis also presented two different methods for the same, one with image priors (see section 5.2) and the other one is a generalised approach across different resolutions and contrasts, without any image priors (see section 5.3). However, all these approaches are solely RMC and do not take into consideration PMC. As can be seen in the last three subsections, there have already been methods combining PMC and RMC. But to date, there has not been any research in the direction of combining deep learning based RMC with PMC. This can be achieved by first performing PMC, then evaluating the image using IQA techniques (such as, the technique presented in section 5.1), and then those PMC-corrected images that are not of usable quality can be supplied to deep learning based RMC method (such as, the methods presented in sections 5.2 and 5.3). Moreover, another interesting research direction might be an end-to-end approach - using the IQA and deep learning based RMC to aid the PMC and vice-versa. One possible option would be to acquire the motion patterns using PMC and use them to perform the artificial motion corruption (presented in sections 5.1 and 5.3) - making it more real-world oriented. These motion patterns can also be used to guide the deep learning based correction algorithm - by using the motion patterns as prior knowledge.

Part VI

APPENDIX

7 APPENDIX

7.1 IMAGE-BASED MOTION ARTEFACTS SIMULATION

The developed in-house algorithm (section 5.1) for motion artefacts simulation is shown in algorithm 1. With this algorithm it has been possible to obtain a more realistic motion artefacts for structural MR images. However, it is important to remark that even though this algorithm provides real looking like motion artefacts, it is not based on real motion patterns that could be for example acquired using an optical tracking system.

7.2 RESNETS PARAMETERS

In this section there are listed the parameters of the artificial neural networks utilised in section 5.

Listing 1: ResNet-18 Parameters

```
----------------------------------------------------------------
        Layer (type)               Output Shape         Param #
================================================================
            Conv2d-1        [-1, 64, 128, 128]           3,136
       BatchNorm2d-2        [-1, 64, 128, 128]             128
              ReLU-3        [-1, 64, 128, 128]               0
         MaxPool2d-4          [-1, 64, 64, 64]               0
            Conv2d-5          [-1, 64, 64, 64]          36,864
       BatchNorm2d-6          [-1, 64, 64, 64]             128
              ReLU-7          [-1, 64, 64, 64]               0
            Conv2d-8          [-1, 64, 64, 64]          36,864
       BatchNorm2d-9          [-1, 64, 64, 64]             128
             ReLU-10          [-1, 64, 64, 64]               0
       BasicBlock-11          [-1, 64, 64, 64]               0
           Conv2d-12          [-1, 64, 64, 64]          36,864
             ....               ...........               ....
           Conv2d-60           [-1, 512, 8, 8]       2,359,296
      BatchNorm2d-61           [-1, 512, 8, 8]           1,024
             ReLU-62           [-1, 512, 8, 8]               0
           Conv2d-63           [-1, 512, 8, 8]       2,359,296
      BatchNorm2d-64           [-1, 512, 8, 8]           1,024
             ReLU-65           [-1, 512, 8, 8]               0
       BasicBlock-66           [-1, 512, 8, 8]               0
AdaptiveAvgPool2d-67               [-1, 512, 1, 1]               0
           Linear-68                   [-1, 1]             513
          Sigmoid-69                   [-1, 1]               0
```

Algorithm 1 Two-dimensional Motion Corruption Simulation

Require:

img: 2D array, input image to be corrupted
sigma_range: tuple, range of values for the amount of corruption to apply
restore_original: float, restoration parameter
n_threads: int, number of threads to use for multiprocessing

Ensure:

cor: 2D array, corrupted image

```
function Motion2D(img, sigma_range, restore_original, n_threads)
    Define a class Motion2D with the following properties:
        sigma_range: tuple, range of values for the amount of corruption to apply
        restore_original: float, restoration parameter
        n_threads: int, number of threads to use for multiprocessing
        perform_singlePE method with idx argument:
            a. Rotate the image by a random angle
            b. Compute the 2D Fourier transform of the rotated image
            c. Add the transformed portion of the rotated image to the appropriate portion of the complex-valued array aux
        call method:
            a. Store the input image img
            b. Initialise the complex-valued array aux to zeros with the same shape as img
            c. Randomly select a horizontal or vertical axis
            d. Determine the size of the subarrays to be used for corrupting
            e. Randomly select a portion of the subarrays to be used for corrupting
            f. Randomly select a corruption amount sigma from sigma_range
            g. Generate an array of random angles to use for corruptin
            h. If n_threads > 1, use multiprocessing to apply the perform_singlePE method to each portion in parallel
            i. Otherwise, apply the perform_singlePE method to each portion sequentially
            j. Compute the inverse Fourier transform of the final transformed array
            k. Normalise the result by dividing by its maximum value plus a small constant
            l. Return the normalised inverse Fourier transform as cor
    Initialise a Motion2D object with the input parameters
    Apply the Motion2D object to the input image img
    Return the corrupted image cor
end function
```

```
================================================================
Total params: 11,170,753
Trainable params: 11,170,753
Non-trainable params: 0
----------------------------------------------------------------
Input size (MB): 0.25
Forward/backward pass size (MB): 82.00
Params size (MB): 42.61
Estimated Total Size (MB): 124.87
----------------------------------------------------------------
```

Listing 2: ResNet-101 Parameters

```
----------------------------------------------------------------
    Layer (type)               Output Shape         Param #
================================================================
        Conv2d-1        [-1, 64, 128, 128]           3,136
   BatchNorm2d-2        [-1, 64, 128, 128]             128
          ReLU-3        [-1, 64, 128, 128]               0
     MaxPool2d-4          [-1, 64, 64, 64]               0
        Conv2d-5          [-1, 64, 64, 64]           4,096
   BatchNorm2d-6          [-1, 64, 64, 64]             128
          ReLU-7          [-1, 64, 64, 64]               0
        Conv2d-8          [-1, 64, 64, 64]          36,864
   BatchNorm2d-9          [-1, 64, 64, 64]             128
         ReLU-10          [-1, 64, 64, 64]               0
       Conv2d-11         [-1, 256, 64, 64]          16,384
       ......          .............             ....
      Conv2d-336          [-1, 512, 8, 8]       2,359,296
 BatchNorm2d-337          [-1, 512, 8, 8]           1,024
        ReLU-338          [-1, 512, 8, 8]               0
      Conv2d-339         [-1, 2048, 8, 8]       1,048,576
 BatchNorm2d-340         [-1, 2048, 8, 8]           4,096
        ReLU-341         [-1, 2048, 8, 8]               0
  Bottleneck-342         [-1, 2048, 8, 8]               0
AdaptiveAvgPool2d-343         [-1, 2048, 1, 1]               0
      Linear-344                 [-1, 1]           2,049
     Sigmoid-345                 [-1, 1]               0
================================================================
Total params: 42,495,937
Trainable params: 42,495,937
Non-trainable params: 0
----------------------------------------------------------------
Input size (MB): 0.25
Forward/backward pass size (MB): 561.27
Params size (MB): 162.11
Estimated Total Size (MB): 723.62
----------------------------------------------------------------
```

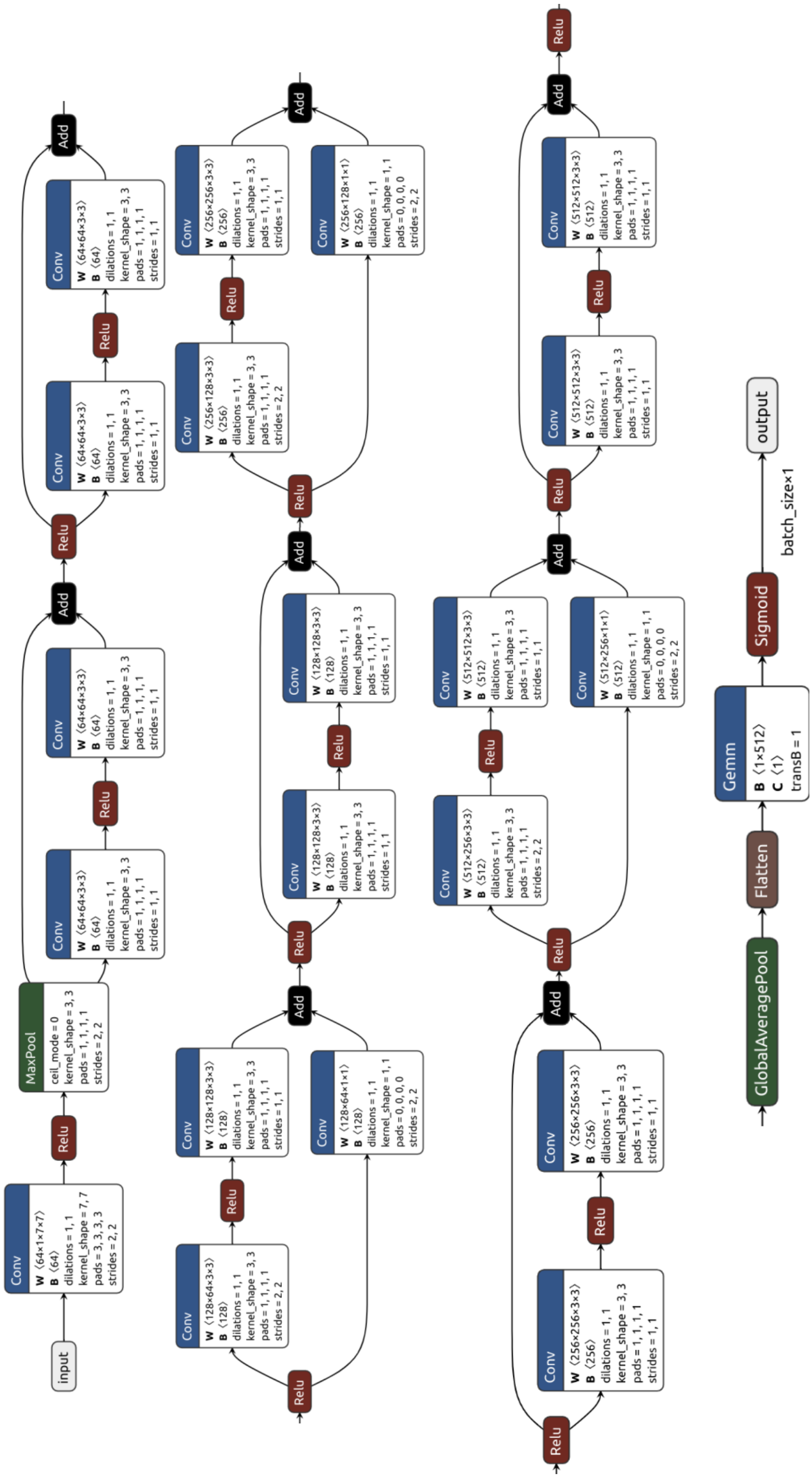

Figure 51: ResNet-18 Diagram.

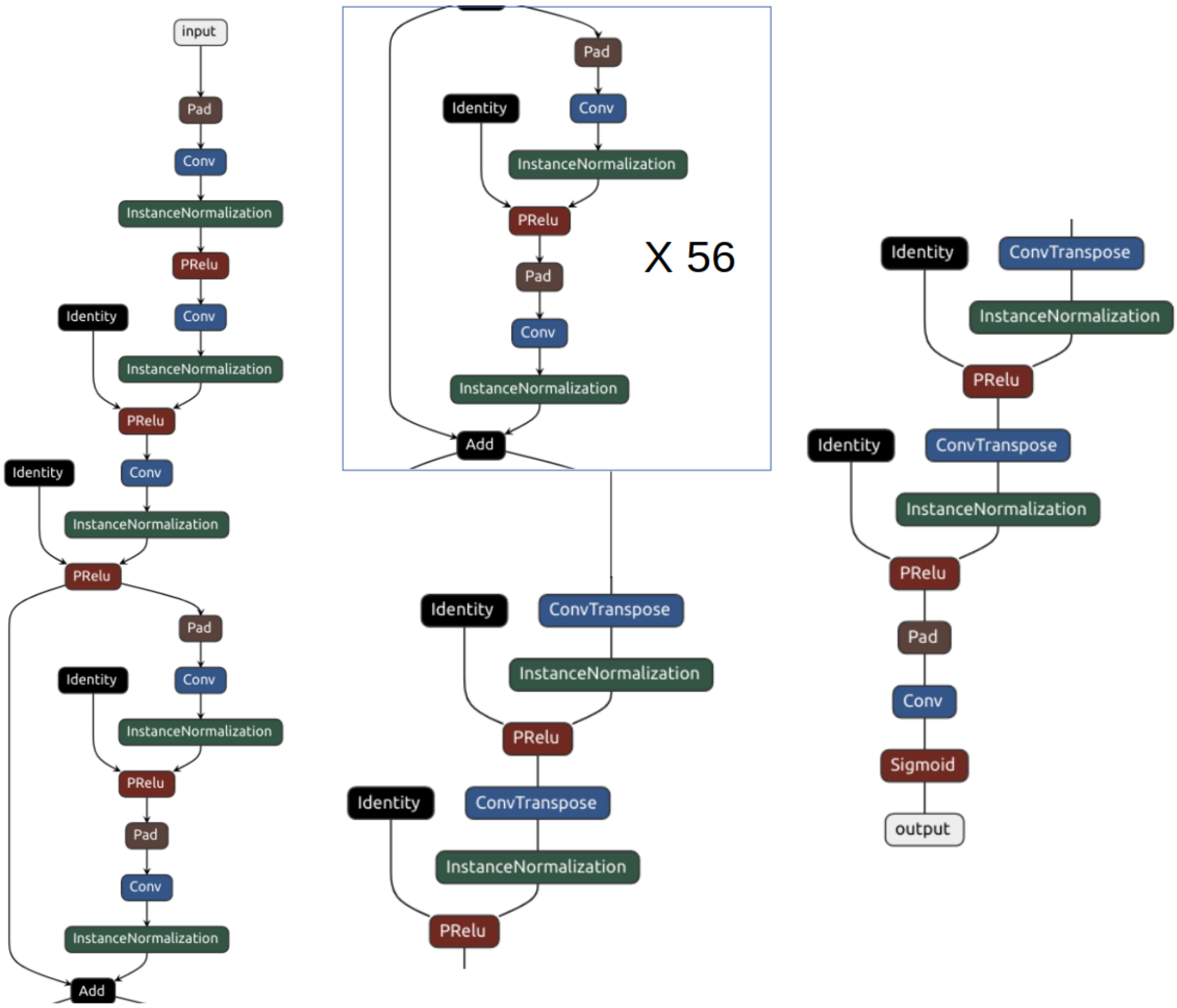

Figure 52: ReconResNet-56 Diagram.

7.3 RECONRESNET PARAMETERS

Hereafter there are shown the model diagram and parameters used in section 5.3.

Listing 3: ReconResNet-56 2D Parameters

```
----------------------------------------------------------------
  Layer (type)               Output Shape         Param #
================================================================
ReflectionPad2d-1          [-1, 1, 262, 262]               0
         Conv2d-2         [-1, 64, 256, 256]           3,200
 InstanceNorm2d-3         [-1, 64, 256, 256]               0
          PReLU-4         [-1, 64, 256, 256]               1
         Conv2d-5        [-1, 128, 128, 128]          73,856
```

```
 InstanceNorm2d-6        [-1, 128, 128, 128]               0
          PReLU-7        [-1, 128, 128, 128]               1
DownsamplingBlock-8        [-1, 128, 128, 128]               0
         Conv2d-9          [-1, 256, 64, 64]         295,168
InstanceNorm2d-10          [-1, 256, 64, 64]               0
         PReLU-11          [-1, 256, 64, 64]               1
DownsamplingBlock-12          [-1, 256, 64, 64]               0
ReflectionPad2d-13          [-1, 256, 66, 66]               0
         Conv2d-14          [-1, 256, 64, 64]         590,080
 InstanceNorm2d-15          [-1, 256, 64, 64]               0
          PReLU-16          [-1, 256, 64, 64]               1
      Dropout2d-17          [-1, 256, 64, 64]               0
ReflectionPad2d-18          [-1, 256, 66, 66]               0
         Conv2d-19          [-1, 256, 64, 64]         590,080
 InstanceNorm2d-20          [-1, 256, 64, 64]               0
  ResidualBlock-21          [-1, 256, 64, 64]               0
          ......                ...........           ......
ReflectionPad2d-513          [-1, 256, 66, 66]               0
         Conv2d-514          [-1, 256, 64, 64]         590,080
 InstanceNorm2d-515          [-1, 256, 64, 64]               0
  ResidualBlock-516          [-1, 256, 64, 64]               0
ConvTranspose2d-517        [-1, 128, 128, 128]         295,040
 InstanceNorm2d-518        [-1, 128, 128, 128]               0
          PReLU-519        [-1, 128, 128, 128]               1
UpsamplingBlock-520        [-1, 128, 128, 128]               0
ConvTranspose2d-521         [-1, 64, 256, 256]          73,792
 InstanceNorm2d-522         [-1, 64, 256, 256]               0
          PReLU-523         [-1, 64, 256, 256]               1
UpsamplingBlock-524         [-1, 64, 256, 256]               0
ReflectionPad2d-525         [-1, 64, 262, 262]               0
         Conv2d-526          [-1, 1, 256, 256]           3,137
        Sigmoid-527          [-1, 1, 256, 256]               0
================================================================
Total params: 66,833,214
Trainable params: 66,833,214
Non-trainable params: 0
----------------------------------------------------------------
Input size (MB): 0.25
Forward/backward pass size (MB): 4507.92
Params size (MB): 254.95
Estimated Total Size (MB): 4763.11
----------------------------------------------------------------
```

BIBLIOGRAPHY

[1] I. I. Rabi. "Space Quantization in a Gyrating Magnetic Field." In: *Phys. Rev.* 51 (8 1937), pp. 652–654. DOI: 10.1103/PhysRev.51.652. URL: https://link.aps.org/doi/10.1103/PhysRev.51.652.

[2] I. I. Rabi, J. R. Zacharias, S. Millman, and P. Kusch. "A New Method of Measuring Nuclear Magnetic Moment." In: *Phys. Rev.* 53 (4 1938), pp. 318–318. DOI: 10.1103/PhysRev.53.318. URL: https://link.aps.org/doi/10.1103/PhysRev.53.318.

[3] F. Bloch, W. W. Hansen, and M. Packard. "The Nuclear Induction Experiment." In: *Phys. Rev.* 70 (7-8 1946), pp. 474–485. DOI: 10.1103/PhysRev.70.474. URL: https://link.aps.org/doi/10.1103/PhysRev.70.474.

[4] N. Bloembergen, E. M. Purcell, and R. V. Pound. "Relaxation Effects in Nuclear Magnetic Resonance Absorption." In: *Phys. Rev.* 73 (7 1948), pp. 679–712. DOI: 10.1103/PhysRev.73.679. URL: https://link.aps.org/doi/10.1103/PhysRev.73.679.

[5] P. C. LAUTERBUR. "Image Formation by Induced Local Interactions: Examples Employing Nuclear Magnetic Resonance." In: *Nature* 242.5394 (Mar. 1973), pp. 190–191. ISSN: 1476-4687. URL: https://doi.org/10.1038/242190a0.

[6] C. Lauterbur P. *Magnetic resonance zeugmatography*. 1974. URL: https://www.degruyter.com/view/j/pac.1974.40.issue-1-2/pac197440010149/pac197440010149.xml.

[7] Anil Kumar, Dieter Welti, and Richard R Ernst. "NMR Fourier zeugmatography." In: *Journal of Magnetic Resonance (1969)* 18.1 (1975), pp. 69 –83. ISSN: 0022-2364. DOI: https://doi.org/10.1016/0022-2364(75)90224-3. URL: http://www.sciencedirect.com/science/article/pii/0022236475902243.

[8] W. P. Aue, E. Bartholdi, and R. R. Ernst. "Two?dimensional spectroscopy. Application to nuclear magnetic resonance." In: *The Journal of Chemical Physics* 64.5 (1976), pp. 2229–2246. DOI: 10.1063/1.432450. eprint: https://doi.org/10.1063/1.432450. URL: https://doi.org/10.1063/1.432450.

[9] Raymond Damadian. *Apparatus and method for detecting cancer in tissue*. US Patent 3,789,832. 1974.

[10] Raymond Damadian. "Nuclear Magnetic Resonance: A Noninvasive Approach to Cancer." In: *Hospital Practice* 12.7 (1977), pp. 63–70. DOI: 10.1080/21548331.1977.11707164. eprint: https://doi.org/10.1080/21548331.1977.11707164. URL: https://doi.org/10.1080/21548331.1977.11707164.

[11] Allen N Garroway, Peter K Grannell, and Peter Mansfield. “Image formation in NMR by a selective irradiative process.” In: *Journal of Physics C: Solid State Physics* 7.24 (1974), p. L457.

[12] Peter Mansfield. “Multi-planar image formation using NMR spin echoes.” In: *Journal of Physics C: Solid State Physics* 10.3 (1977), p. L55.

[13] Peter Mansfield and Andrew A Maudsley. “Medical imaging by NMR.” In: *The British journal of radiology* 50.591 (1977), pp. 188–194.

[14] Peter Mansfield. *Nmr imaging in biomedicine: Supplement 2 advances in magnetic resonance*. Vol. 2. Elsevier, 1982.

[15] Richard S Likes. *Moving gradient zeugmatography*. US Patent 4,307,343. 1981.

[16] Donald B. Twieg. “The k-trajectory formulation of the NMR imaging process with applications in analysis and synthesis of imaging methods.” In: *Medical Physics* 10.5 (1983), pp. 610–621. DOI: 10.1118/1.595331. eprint: https://aapm.onlinelibrary.wiley.com/doi/pdf/10.1118/1.595331. URL: https://aapm.onlinelibrary.wiley.com/doi/abs/10.1118/1.595331.

[17] Stig Ljunggren. “A simple graphical representation of fourier-based imaging methods.” In: *Journal of Magnetic Resonance (1969)* 54.2 (1983), pp. 338–343. ISSN: 0022-2364. DOI: https://doi.org/10.1016/0022-2364(83)90060-4. URL: http://www.sciencedirect.com/science/article/pii/0022236483900604.

[18] D Le Bihan, E Breton, D Lallemand, P Grenier, E Cabanis, and M Laval-Jeantet. “MR imaging of intravoxel incoherent motions: application to diffusion and perfusion in neurologic disorders.” In: *Radiology* 161.2 (1986). PMID: 3763909, pp. 401–407. DOI: 10.1148/radiology.161.2.3763909. eprint: https://doi.org/10.1148/radiology.161.2.3763909. URL: https://doi.org/10.1148/radiology.161.2.3763909.

[19] B. Chapman, R. Turner, R. J. Ordidge, M. Doyle, M. Cawley, R. Coxon, P. Glover, and P. Mansfield. “Real-time movie imaging from a single cardiac cycle by NMR.” In: *Magnetic Resonance in Medicine* 5.3 (1987), pp. 246–254. DOI: 10.1002/mrm.1910050305. eprint: https://onlinelibrary.wiley.com/doi/pdf/10.1002/mrm.1910050305. URL: https://onlinelibrary.wiley.com/doi/abs/10.1002/mrm.1910050305.

[20] M. Hedley, H. Yan, and D. Rosenfeld. “Motion artifact correction in MRI using generalized projections.” In: *IEEE Transactions on Medical Imaging* 10.1 (1991), pp. 40–46. DOI: 10.1109/42.75609.

[21] Joel P. Felmlee, Richard L. Ehman, Stephen J. Riederer, and Hope W. Korin. “Adaptive motion compensation in MRI: Accuracy of motion measurement.” In: *Magnetic Resonance in Medicine* 18.1 (1991), pp. 207–213. DOI: 10.1002/mrm.1910180121. eprint: https://onlinelibrary.wiley.com/doi/pdf/10.1002/mrm.1910180121. URL: https://onlinelibrary.wiley.com/doi/abs/10.1002/mrm.1910180121.

[22] G. H. Glover and J. M. Pauly. "Projection Reconstruction Techniques for Reduction of Motion Effects in MRI." In: *Magnetic Resonance in Medicine* 28.2 (1992), pp. 275–289. DOI: 10.1002/mrm.1910280209. eprint: https://onlinelibrary.wiley.com/doi/pdf/10.1002/mrm.1910280209. URL: https://onlinelibrary.wiley.com/doi/abs/10.1002/mrm.1910280209.

[23] M. Hedley, H. Yan, and D. Rosenfeld. "A modified Gerchberg-Saxton algorithm for one-dimensional motion artifact correction in MRI." In: *IEEE Transactions on Signal Processing* 39.6 (June), pp. 1428–1433.

[24] M. Medley, H. Yan, and D. Rosenfeld. "An improved algorithm for 2-D translational motion artifact correction." In: *IEEE Transactions on Medical Imaging* 10.4 (Dec.), pp. 548–553.

[25] M. Louis Lauzon and Brian K. Rutt. "Generalized K-space analysis and correction of motion effects in MR imaging." In: *Magnetic Resonance in Medicine* 30.4 (1993), pp. 438–446. DOI: 10.1002/mrm.1910300406. eprint: https://onlinelibrary.wiley.com/doi/pdf/10.1002/mrm.1910300406. URL: https://onlinelibrary.wiley.com/doi/abs/10.1002/mrm.1910300406.

[26] A Connelly, G D Jackson, R S Frackowiak, J W Belliveau, F Vargha-Khadem, and D G Gadian. "Functional mapping of activated human primary cortex with a clinical MR imaging system." In: *Radiology* 188.1 (1993). PMID: 8511285, pp. 125–130. DOI: 10.1148/radiology.188.1.8511285. eprint: https://doi.org/10.1148/radiology.188.1.8511285. URL: https://doi.org/10.1148/radiology.188.1.8511285.

[27] R.T. Constable, G. McCarthy, T. Allison, A.W. Anderson, and J.C. Gore. "Functional brain imaging at 1.5 T using conventional gradient echo MR imaging techniques." In: *Magnetic Resonance Imaging* 11.4 (1993), pp. 451 – 459. ISSN: 0730-725X. DOI: https://doi.org/10.1016/0730-725X(93)90463-N. URL: http://www.sciencedirect.com/science/article/pii/0730725X9390463N.

[28] Raffaella Aversa, Relly Victoria Petrescu, Antonio Apicella, and Florian Ion Petrescu. "The basic elements of life's." In: *American Journal of Engineering and Applied Sciences* 9.4 (2016), pp. 1189–1197.

[29] LM Sehgal. "Angular momentum composition of the proton in the quark-parton model." In: *Physical Review D* 10.5 (1974), p. 1663.

[30] Brian Harold Bransden and Charles Jean Joachain. *Physics of atoms and molecules*. Pearson Education India, 2003.

[31] William G McMillan Jr and Joseph E Mayer. "The statistical thermodynamics of multicomponent systems." In: *The Journal of Chemical Physics* 13.7 (1945), pp. 276–305.

[32] Robert W Brown, Y-C Norman Cheng, E Mark Haacke, Michael R Thompson, and Ramesh Venkatesan. *Magnetic resonance imaging: physical principles and sequence design*. John Wiley & Sons, 2014.

[33] LI Schiff and H Snyder. "Theory of the quadratic Zeeman effect." In: *Physical Review* 55.1 (1939), p. 59.

[34] Chrit TW Moonen, Peter CM Van Zijl, Joseph A Frank, Denis Le Bihan, and Edwin D Becker. "Functional magnetic resonance imaging in medicine and physiology." In: *Science* 250.4977 (1990), pp. 53–61.

[35] Seiji Ogawa, Tso-Ming Lee, Alan R Kay, and David W Tank. "Brain magnetic resonance imaging with contrast dependent on blood oxygenation." In: *proceedings of the National Academy of Sciences* 87.24 (1990), pp. 9868–9872.

[36] Roger J Ordidge, Jay M Gorell, Jean C Deniau, Robert A Knight, and Joseph A Helpern. "Assessment of relative brain iron concentrations using T2-weighted and T2*-weighted MRI at 3 Tesla." In: *Magnetic resonance in medicine* 32.3 (1994), pp. 335–341.

[37] Josef Vymazal, Rodney A Brooks, Nicholas Patronas, Milan Hajek, Jeff WM Bulte, and Giovanni Di Chiro. "Magnetic resonance imaging of brain iron in health and disease." In: *Journal of the neurological sciences* 134 (1995), pp. 19–26.

[38] John F Schenck. "Magnetic resonance imaging of brain iron." In: *Journal of the neurological sciences* 207.1 (2003), pp. 99–102.

[39] E Mark Haacke, Norman YC Cheng, Michael J House, Qiang Liu, Jaladhar Neelavalli, Robert J Ogg, Asadullah Khan, Muhammad Ayaz, Wolff Kirsch, and Andre Obenaus. "Imaging iron stores in the brain using magnetic resonance imaging." In: *Magnetic resonance imaging* 23.1 (2005), pp. 1–25.

[40] Malcolm H Levitt. *Spin dynamics: basics of nuclear magnetic resonance*. John Wiley & Sons, 2013.

[41] Donald W McRobbie, Elizabeth A Moore, Martin J Graves, and Martin R Prince. *MRI from Picture to Proton*. Cambridge university press, 2017.

[42] Dwight George Nishimura. *Principles of magnetic resonance imaging*. Stanford University, 1996.

[43] Erwin L Hahn. "Spin echoes." In: *Physical review* 80.4 (1950), p. 580.

[44] Jens Frahm, Klaus-Dietmar Merboldt, Wolfgang Hänicke, and Axel Haase. "Stimulated echo imaging." In: *Journal of Magnetic Resonance (1969)* 64.1 (1985), pp. 81–93.

[45] Michael Markl and Jochen Leupold. "Gradient echo imaging." In: *Journal of Magnetic Resonance Imaging* 35.6 (2012), pp. 1274–1289.

[46] Reuben Mezrich. "A perspective on K-space." In: *Radiology* 195.2 (1995), pp. 297–315.

[47] Valerij G Kiselev, Klaus R Hahn, and Dorothee P Auer. "Is the brain cortex a fractal?" In: *Neuroimage* 20.3 (2003), pp. 1765–1774.

[48] L Axel, RM Summers, HY Kressel, and C Charles. "Respiratory effects in two-dimensional Fourier transform MR imaging." In: *Radiology* 160.3 (1986), pp. 795–801.

[49] Pippa Storey, Qun Chen, Wei Li, Robert R Edelman, and Pottumarthi V Prasad. "Band artifacts due to bulk motion." In: *Magnetic Resonance in Medicine: An Official Journal of the International Society for Magnetic Resonance in Medicine* 48.6 (2002), pp. 1028–1036.

[50] Michael L Wood and R Mark Henkelman. "MR image artifacts from periodic motion." In: *Medical physics* 12.2 (1985), pp. 143–151.

[51] Joel P Felmlee, Richard L Ehman, Stephen J Riederer, and Hope W Korin. "Adaptive motion compensation in MRI: accuracy of motion measurement." In: *Magnetic resonance in medicine* 18.1 (1991), pp. 207–213.

[52] Rasmus M Birn, Peter A Bandettini, Robert W Cox, Andrzej Jesmanowicz, and Reza Shaker. "Magnetic field changes in the human brain due to swallowing or speaking." In: *Magnetic Resonance in Medicine* 40.1 (1998), pp. 55–60.

[53] Pierre-François Van de Moortele, Josef Pfeuffer, Gary H Glover, Kamil Ugurbil, and Xiaoping Hu. "Respiration-induced B0 fluctuations and their spatial distribution in the human brain at 7 Tesla." In: *Magnetic Resonance in Medicine: An Official Journal of the International Society for Magnetic Resonance in Medicine* 47.5 (2002), pp. 888–895.

[54] Frank Godenschweger, Urte Kägebein, Daniel Stucht, Uten Yarach, Alessandro Sciarra, Renat Yakupov, Falk Lüsebrink, Peter Schulze, and Oliver Speck. "Motion correction in MRI of the brain." In: *Physics in medicine & biology* 61.5 (2016), R32.

[55] David Atkinson, Derek LG Hill, Peter NR Stoyle, Paul E Summers, Stuart Clare, Richard Bowtell, and Stephen F Keevil. "Automatic compensation of motion artifacts in MRI." In: *Magnetic Resonance in Medicine: An Official Journal of the International Society for Magnetic Resonance in Medicine* 41.1 (1999), pp. 163–170.

[56] PG Batchelor, D Atkinson, P Irarrazaval, DLG Hill, J Hajnal, and D Larkman. "Matrix description of general motion correction applied to multishot images." In: *Magnetic Resonance in Medicine: An Official Journal of the International Society for Magnetic Resonance in Medicine* 54.5 (2005), pp. 1273–1280.

[57] Gunnar Krüger and Gary H Glover. "Physiological noise in oxygenation-sensitive magnetic resonance imaging." In: *Magnetic Resonance in Medicine: An Official Journal of the International Society for Magnetic Resonance in Medicine* 46.4 (2001), pp. 631–637.

[58] Maxim Zaitsev, Julian Maclaren, and Michael Herbst. "Motion artifacts in MRI: A complex problem with many partial solutions." In: *Journal of Magnetic Resonance Imaging* 42.4 (2015), pp. 887–901. DOI: 10.1002/jmri.24850. eprint: https://onlinelibrary.wiley.com/doi/pdf/10.1002/jmri.24850. URL: https://onlinelibrary.wiley.com/doi/abs/10.1002/jmri.24850.

[59] Patricia M Johnson and Maria Drangova. “Motion correction in MRI using deep learning.” In: *Proceedings of the ISMRM Scientific Meeting & Exhibition, Paris*. Vol. 4098. 2018, pp. 1–4.

[60] Gastao Cruz, David Atkinson, Markus Henningsson, Rene M Botnar, and Claudia Prieto. “Highly efficient nonrigid motion-corrected 3D whole-heart coronary vessel wall imaging.” In: *Magnetic resonance in medicine* 77.5 (2017), pp. 1894–1908.

[61] E. Mark Haacke and John L. Patrick. “Reducing motion artifacts in two-dimensional Fourier transform imaging.” In: *Magnetic Resonance Imaging* 4.4 (1986), pp. 359–376. DOI: 10.1016/0730-725X(86)91046-5. URL: http://dx.doi.org/10.1016/0730-725X(86)91046-5.

[62] J.T. Vaughan and J.R. Griffiths. *RF Coils for MRI*. eMagRes Books. Wiley, 2012. ISBN: 9781118590454. URL: https://books.google.de/books?id=RHGX79V2jVgC.

[63] J. Jin. *Electromagnetic Analysis and Design in Magnetic Resonance Imaging*. CRC Press, 2018. ISBN: 9781351453400. URL: https://books.google.de/books?id=9vlKDwAAQBAJ.

[64] R. Perez. *Design of Medical Electronic Devices*. Biomedical engineering: Electronic engineering. Elsevier Science, 2002. ISBN: 9780125507110. URL: https://books.google.de/books?id=A29AZ5IVB-kC.

[65] P.M. Robitaille and L. Berliner. *Ultra High Field Magnetic Resonance Imaging*. Biological Magnetic Resonance. Springer US, 2007. ISBN: 9780387496481. URL: https://books.google.de/books?id=dmji1Cjmv7sC.

[66] J. Hennig and O. Speck. *High-Field MR Imaging*. Medical Radiology. Springer Berlin Heidelberg, 2011. ISBN: 9783540850908. URL: https://books.google.de/books?id=YffR0csTVYcC.

[67] Christine C. Lee, Clifford R. Jack, Roger C. Grimm, Phillip J. Rossman, Joel P. Felmlee, Richard L. Ehman, and Stephen J. Riederer. “Real-time adaptive motion correction in functional MRI.” In: *Magnetic Resonance in Medicine* 36.3 (1996), pp. 436–444. ISSN: 1522-2594. DOI: 10.1002/mrm.1910360316. URL: http://dx.doi.org/10.1002/mrm.1910360316.

[68] Christine C Lee, Roger C Grimm, Armando Manduca, Joel P Felmlee, Richard L Ehman, Stephen J Riederer, and Clifford R Jack Jr. “A prospective approach to correct for inter-image head rotation in fMRI.” In: *Magnetic resonance in medicine* 39.2 (1998), pp. 234–243.

[69] Guy Shechter and Elliot R McVeigh. “MR motion correction of 3D affine deformations.” In: *Proceedings Int Soc Mag Reson Med*. Citeseer. 2003.

[70] Dirk Manke, Kay Nehrke, and Peter Börnert. “Novel prospective respiratory motion correction approach for free-breathing coronary MR angiography using a patient-adapted affine motion model.” In: *Magnetic Resonance in Medicine: An Official Journal of the International Society for Magnetic Resonance in Medicine* 50.1 (2003), pp. 122–131.

[71] Guy Shechter. *Respiratory motion of the heart: implications for magnetic resonance coronary angiography*. The Johns Hopkins University, 2004.

[72] Kay Nehrke and Peter Börnert. "Prospective correction of affine motion for arbitrary MR sequences on a clinical scanner." In: *Magnetic Resonance in Medicine: An Official Journal of the International Society for Magnetic Resonance in Medicine* 54.5 (2005), pp. 1130–1138.

[73] Julian Maclaren, Michael Herbst, Oliver Speck, and Maxim Zaitsev. "Prospective motion correction in brain imaging: A review." In: *Magnetic Resonance in Medicine* 69.3 (2013), pp. 621–636. ISSN: 1522-2594. DOI: 10.1002/mrm.24314. URL: http://dx.doi.org/10.1002/mrm.24314.

[74] F Godenschweger, U Kägebein, D Stucht, U Yarach, A Sciarra, R Yakupov, F Lüsebrink, P Schulze, and O Speck. "Motion correction in MRI of the brain." In: *Physics in Medicine & Biology* 61.5 (2016), R32. URL: http://stacks.iop.org/0031-9155/61/i=5/a=R32.

[75] Maxim Zaitsev, Christian Dold, Georgios Sakas, Jürgen Hennig, and Oliver Speck. "Magnetic resonance imaging of freely moving objects: prospective real-time motion correction using an external optical motion tracking system." In: *Neuroimage* 31.3 (2006), pp. 1038–1050.

[76] Julian Maclaren, Oliver Speck, Daniel Stucht, Peter Schulze, Jürgen Hennig, and Maxim Zaitsev. "Navigator Accuracy Requirements for Prospective Motion Correction." In: *Magnetic resonance in medicine : official journal of the Society of Magnetic Resonance in Medicine / Society of Magnetic Resonance in Medicine* 63.1 (Jan. 2010), pp. 162–170. DOI: 10.1002/mrm.22191. URL: http://www.ncbi.nlm.nih.gov/pmc/articles/PMC2933924/.

[77] Maxim Zaitsev, Julian Maclaren, and Michael Herbst. "Motion Artefacts in MRI: a Complex Problem with Many Partial Solutions." In: *Journal of magnetic resonance imaging : JMRI* 42.4 (Oct. 2015), pp. 887–901. DOI: 10.1002/jmri.24850. URL: http://www.ncbi.nlm.nih.gov/pmc/articles/PMC4517972/.

[78] Aditya Singh, Benjamin Zahneisen, Brian Keating, Michael Herbst, Linda Chang, Maxim Zaitsev, and Thomas Ernst. "Optical Tracking With Two Markers for Robust Prospective Motion Correction for Brain Imaging." In: *Magma (New York, N.Y.)* 28.6 (Dec. 2015), pp. 523–534. DOI: 10.1007/s10334-015-0493-4. URL: http://www.ncbi.nlm.nih.gov/pmc/articles/PMC5259555/.

[79] Daniel Stucht, K. Appu Danishad, Peter Schulze, Frank Godenschweger, Maxim Zaitsev, and Oliver Speck. "Highest Resolution In Vivo Human Brain MRI Using Prospective Motion Correction." In: *PLOS ONE* 10.7 (July 2015), e0133921–. URL: https://doi.org/10.1371/journal.pone.0133921.

[80] Julian Maclaren et al. "Measurement and Correction of Microscopic Head Motion during Magnetic Resonance Imaging of the Brain." In: *PLoS ONE* 7.11 (2012). Ed. by Christopher P Hess, e48088. DOI: 10.1371/journal.pone.0048088. URL: http://www.ncbi.nlm.nih.gov/pmc/articles/PMC3492340/.

[81] Maxim Zaitsev, Christian Dold, Jürgen Hennig, and Oliver Speck. "Integration of an External Motion Tracking System with the MR Scanner for Highly Accurate Real-Time Prospective Motion Correction." In: *Proc. Intl. Soc. Mag. Reson. Med*. Vol. 14. 2006, p. 1355.

[82] Ilja Kadashevich, D Appu, and Oliver Speck. "Automatic motion selection in one step cross-calibration for prospective MR motion correction." In: *MAGMA* 24.Supplement 1 (2011), pp. 266–267.

[83] Marleine Tremblay, Fred Tam, and Simon J Graham. "Retrospective coregistration of functional magnetic resonance imaging data using external monitoring." In: *Magnetic Resonance in Medicine: An Official Journal of the International Society for Magnetic Resonance in Medicine* 53.1 (2005), pp. 141–149.

[84] Edward F Jackson, Lawrence E Ginsberg, Don F Schomer, and Norman E Leeds. "A review of MRI pulse sequences and techniques in neuroimaging." In: *Surgical Neurology* 47.2 (1997), pp. 185–199.

[85] John P Mugler III. "Overview of MR imaging pulse sequences." In: *Magnetic resonance imaging clinics of North America* 7.4 (1999), pp. 661–697.

[86] Matt A Bernstein, Kevin F King, and Xiaohong Joe Zhou. *Handbook of MRI pulse sequences*. Elsevier, 2004.

[87] Richard R Ernst, Geoffrey Bodenhausen, and Alexander Wokaun. *Principles of nuclear magnetic resonance in one and two dimensions*. BOOK. 1987.

[88] A Haase, J Frahm, D Matthaei, W Hanicke, and K. D Merboldt. "FLASH imaging. Rapid NMR imaging using low flip-angle pulses." In: *Journal of Magnetic Resonance (1969)* 67.2 (1986), pp. 258–266. DOI: https://doi.org/10.1016/0022-2364(86)90433-6. URL: http://www.sciencedirect.com/science/article/pii/0022236486904336.

[89] John P. Mugler and James R. Brookeman. "Rapid three-dimensional T1-weighted MR imaging with the MP-RAGE sequence." In: *Journal of Magnetic Resonance Imaging* 1.5 (1991), pp. 561–567. ISSN: 1522-2586. DOI: 10.1002/jmri.1880010509. URL: http://dx.doi.org/10.1002/jmri.1880010509.

[90] Val M. Runge, John E. Kirsch, Gregory S. Thomas, and John P. Mugler. "Clinical comparison of three-dimensional MP-RAGE and FLASH techniques for MR imaging of the head." In: *Journal of Magnetic Resonance Imaging* 1.4 (1991), pp. 493–500. ISSN: 1522-2586. DOI: 10.1002/jmri.1880010417. URL: http://dx.doi.org/10.1002/jmri.1880010417.

[91] John P. Mugler, Thomas A. Spraggins, and James R. Brookeman. "T2-weighted three-dimensional MP-RAGE MR imaging." In: *Journal of Magnetic Resonance Imaging* 1.6 (1991), pp. 731–737. ISSN: 1522-2586. DOI: 10.1002/jmri.1880010621. URL: http://dx.doi.org/10.1002/jmri.1880010621.

[92] EM Haacke and JA Tkach. "Fast MR imaging: techniques and clinical applications." In: *AJR. American journal of roentgenology* 155.5 (1990), pp. 951–964.

[93] Charles G Peterfy. "MR imaging." In: *Baillière's clinical rheumatology* 10.4 (1996), pp. 635–678.

[94] A.D. Elster and J.H. Burdette. *Questions & Answers in Magnetic Resonance Imaging*. Mosby, 2001. ISBN: 9780323011846. URL: https://books.google.it/books?id=QY5jQgAACAAJ.

[95] I. Goodfellow, Y. Bengio, and A. Courville. *Deep Learning*. Adaptive Computation and Machine Learning series. MIT Press, 2016. ISBN: 9780262035613. URL: https://books.google.it/books?id=Np9SDQAAQBAJ.

[96] Pariwat Ongsulee. "Artificial intelligence, machine learning and deep learning." In: *2017 15th international conference on ICT and knowledge engineering (ICT&KE)*. IEEE. 2017, pp. 1–6.

[97] Arthur L Samuel. "Some studies in machine learning using the game of checkers." In: *IBM Journal of research and development* 3.3 (1959), pp. 210–229.

[98] Yann LeCun, Yoshua Bengio, and Geoffrey Hinton. "Deep learning." In: *nature* 521.7553 (2015), pp. 436–444.

[99] Mohamed Farouk Abdel Hady and Friedhelm Schwenker. "Semi-supervised learning." In: *Handbook on Neural Information Processing* (2013), pp. 215–239.

[100] Zoubin Ghahramani. "Unsupervised learning." In: *Advanced Lectures on Machine Learning: ML Summer Schools 2003, Canberra, Australia, February 2-14, 2003, Tübingen, Germany, August 4-16, 2003, Revised Lectures* (2004), pp. 72–112.

[101] M Emre Celebi and Kemal Aydin. *Unsupervised learning algorithms*. Vol. 9. Springer, 2016.

[102] Leslie Pack Kaelbling, Michael L Littman, and Andrew W Moore. "Reinforcement learning: A survey." In: *Journal of artificial intelligence research* 4 (1996), pp. 237–285.

[103] Marco A Wiering and Martijn Van Otterlo. "Reinforcement learning." In: *Adaptation, learning, and optimization* 12.3 (2012), p. 729.

[104] Florian Knoll, Kerstin Hammernik, Chi Zhang, Steen Moeller, Thomas Pock, Daniel K Sodickson, and Mehmet Akcakaya. "Deep-learningJohnson PM, Drangova M. methods for parallel magnetic resonance imaging reconstruction: A survey of the current approaches, trends, and issues." In: *IEEE signal processing magazine* 37.1 (2020), pp. 128–140.

[105] Chee-Peng Lim, Ashlesha Vaidya, Yen-Wei Chen, Tejasvi Jain, and Lakhmi C Jain. *Artificial Intelligence and Machine Learning for Healthcare: Vol. 1: Image and Data Analytics*. Vol. 228. Springer Nature, 2022.

[106] Soumick Chatterjee, Alessandro Sciarra, Max Dünnwald, Anitha Bhat Talagini Ashoka, Mayura Gurjar Cheepinahalli Vasudeva, Shudarsan Saravanan, Venkatesh Thirugnana Sambandham, Steffen Oeltze-Jafra, Oliver Speck, and Andreas Nürnberger. "Uncertainty quantification for ground-truth free evaluation of deep learning reconstructions." In: ().

[107] Fang Liu, Richard Kijowski, Georges El Fakhri, and Li Feng. "Magnetic resonance parameter mapping using model-guided self-supervised deep learning." In: *Magnetic resonance in medicine* 85.6 (2021), pp. 3211–3226.

[108] Li Feng, Dan Ma, and Fang Liu. "Rapid MR relaxometry using deep learning: An overview of current techniques and emerging trends." In: *NMR in Biomedicine* 35.4 (2022), e4416.

[109] Thomas Küstner, Karim Armanious, Jiahuan Yang, Bin Yang, Fritz Schick, and Sergios Gatidis. "Retrospective correction of motion-affected MR images using deep learning frameworks." In: *Magnetic resonance in medicine* 82.4 (2019), pp. 1527–1540.

[110] Soumick Chatterjee, Alessandro Sciarra, Max Dünnwald, Steffen Oeltze-Jafra, Andreas Nürnberger, and Oliver Speck. "Retrospective Motion Correction of MR Images using Prior-Assisted Deep Learning." In: *Medical Imaging meets NeurIPS 2020*. Dec. 2020.

[111] Alessandro Sciarra, Soumick Chatterjee, Max Dünnwald, Giuseppe Placidi, Andreas Nürnberger, Oliver Speck, and Steffen Oeltze-Jafra. "Reference-less SSIM Regression for Detection and Quantification of Motion Artefacts in Brain MRIs." In: *Medical Imaging with Deep Learning*. 2022. URL: https://2022.midl.io/papers/e_s_9.

[112] Can Zhao, Muhan Shao, Aaron Carass, Hao Li, Blake E Dewey, Lotta M Ellingsen, Jonghye Woo, Michael A Guttman, Ari M Blitz, Maureen Stone, et al. "Applications of a deep learning method for anti-aliasing and super-resolution in MRI." In: *Magnetic resonance imaging* 64 (2019), pp. 132–141.

[113] Alessandro Sciarra, Max Dünnwald, Hendrik Mattern, Oliver Speck, and Steffen Oeltze-Jafra. "Super-Resolution with Conditional-GAN for MR Brain Images." In: ().

[114] Xingyu Gao, Feng Shi, Dinggang Shen, and Manhua Liu. "Task-induced pyramid and attention GAN for multimodal brain image imputation and classification in alzheimer's disease." In: *IEEE journal of biomedical and health informatics* 26.1 (2021), pp. 36–43.

[115] Ragheb Raad, Dhruv Patel, Chiao-Chih Hsu, Vijay Kothapalli, Deep Ray, Bino Varghese, Darryl Hwang, Inderbir Gill, Vinay Duddalwar, and Assad A Oberai. "Probabilistic medical image imputation via deep adversarial learning." In: *Engineering with Computers* 38.5 (2022), pp. 3975–3986.

[116] Natan Andrade, Fabio Augusto Faria, and Fábio Augusto Menocci Cappabianco. "A practical review on medical image registration: From rigid to deep learning based approaches." In: *2018 31st SIBGRAPI Conference on Graphics, Patterns and Images (SIBGRAPI)*. IEEE. 2018, pp. 463–470.

[117] Jin Liu, Yi Pan, Min Li, Ziyue Chen, Lu Tang, Chengqian Lu, and Jianxin Wang. "Applications of deep learning to MRI images: A survey." In: *Big Data Mining and Analytics* 1.1 (2018), pp. 1–18.

[118] Ali Işın, Cem Direkoğlu, and Melike Şah. "Review of MRI-based brain tumor image segmentation using deep learning methods." In: *Procedia Computer Science* 102 (2016), pp. 317–324.

[119] Guotai Wang, Wenqi Li, Maria A Zuluaga, Rosalind Pratt, Premal A Patel, Michael Aertsen, Tom Doel, Anna L David, Jan Deprest, Sébastien Ourselin, et al. "Interactive medical image segmentation using deep learning with image-specific fine tuning." In: *IEEE transactions on medical imaging* 37.7 (2018), pp. 1562–1573.

[120] Esther E Bron, Stefan Klein, Janne M Papma, Lize C Jiskoot, Vikram Venkataghavan, Jara Linders, Pauline Aalten, Peter Paul De Deyn, Geert Jan Biessels, Jurgen AHR Claassen, et al. "Cross-cohort generalizability of deep and conventional machine learning for MRI-based diagnosis and prediction of Alzheimer's disease." In: *NeuroImage: Clinical* 31 (2021), p. 102712.

[121] Ali Haidar Syaifullah, Akihiko Shiino, Hitoshi Kitahara, Ryuta Ito, Manabu Ishida, and Kenji Tanigaki. "Machine learning for diagnosis of AD and prediction of MCI progression from brain MRI using brain anatomical analysis using diffeomorphic deformation." In: *Frontiers in Neurology* 11 (2021), p. 576029.

[122] Warren S. McCulloch and Walter Pitts. "A logical calculus of the ideas immanent in nervous activity." In: *The Bulletin of Mathematical Biophysics* 5.4 (Dec. 1943), pp. 115–133. DOI: 10.1007/bf02478259. URL: https://doi.org/10.1007/bf02478259.

[123] F Rosenblatt. "Th eperceptron: A perceiving and recognizing automaton." In: *Cornell University, Ithaca, NY, Project PARA, Cornell Aeronaunt Laboratory, Rep* (1957), pp. 85–460.

[124] Mikel Olazaran. "A Sociological Study of the Official History of the Perceptrons Controversy." In: *Social Studies of Science* 26.3 (Aug. 1996), pp. 611–659. DOI: 10.1177/030631296026003005. URL: https://doi.org/10.1177/030631296026003005.

[125] Christopher M Bishop and Nasser M Nasrabadi. *Pattern recognition and machine learning*. Vol. 4. 4. Springer, 2006.

[126] T.J. Sejnowski. *The Deep Learning Revolution*. MIT Press, 2018. ISBN: 9780262038034. URL: https://books.google.it/books?id=9xZxDwAAQBAJ.

[127] Samer Y Khamaiseh, Derek Bagagem, Abdullah Al-Alaj, Mathew Mancino, and Hakam W Alomari. “Adversarial deep learning: A survey on adversarial attacks and defense mechanisms on image classification.” In: *IEEE Access* (2022).

[128] SIMON HAYKIN. “Neural Networks: A Guided Tour.” In: *Soft Computing and Intelligent Systems*. Elsevier, 2000, pp. 71–80. DOI: 10.1016/b978-012646490-0/50007-x. URL: https://doi.org/10.1016/b978-012646490-0/50007-x.

[129] Shun-ichi Amari. “Backpropagation and stochastic gradient descent method.” In: *Neurocomputing* 5.4-5 (1993), pp. 185–196.

[130] Alex Kirzhevsky, Ilya Sutskever, and Geoffrey E Hinton. “Imagenet classification with deep convolutional neural networks.” In: *Advances in neural information processing systems* 25 (2012), pp. 1097–1105.

[131] C Sidney Burrus and T Parks. “Convolution algorithms.” In: *Citeseer: New York, NY, USA* 6 (1985).

[132] Mahdi Khosravy, Nilesh Patel, Neeraj Gupta, and Ishwar K Sethi. “Image quality assessment: A review to full reference indexes.” In: *Recent trends in communication, computing, and electronics* (2019), pp. 279–288.

[133] Li Sze Chow and Raveendran Paramesran. “Review of medical image quality assessment.” In: *Biomedical signal processing and control* 27 (2016), pp. 145–154.

[134] Bénédicte Mortamet, Matt A Bernstein, Clifford R Jack Jr, Jeffrey L Gunter, Chadwick Ward, Paula J Britson, Reto Meuli, Jean-Philippe Thiran, and Gunnar Krueger. “Automatic quality assessment in structural brain magnetic resonance imaging.” In: *Magnetic Resonance in Medicine: An Official Journal of the International Society for Magnetic Resonance in Medicine* 62.2 (2009), pp. 365–372.

[135] Alessandro Sciarra, Max Duennwald, Soumick Chatterjee, Oliver Speck, and Steffen Oeltze-jafra. “Classification of motion corrupted brain MR images using deep learning techniques.” In: *Magnetic Resonance Materials in Physics, Biology and Medicine* 33.1 (2020), pp. 13–45. ISSN: 1352-8661. DOI: 10.1007/s10334-020-00874-0. URL: https://doi.org/10.1007/s10334-020-00874-0.

[136] Philippe Bourel, David Gibon, Eric Coste, Vincent Daanen, and Jean Rousseau. “Automatic quality assessment protocol for MRI equipment.” In: *Medical physics* 26.12 (1999), pp. 2693–2700.

[137] Peter Jezzard. “The physical basis of spatial distortions in magnetic resonance images.” In: (2009).

[138] Jeffrey J Ma, Ukash Nakarmi, Cedric Yue Sik Kin, Christopher M Sandino, Joseph Y Cheng, Ali B Syed, Peter Wei, John M Pauly, and Shreyas S Vasanawala. "Diagnostic image quality assessment and classification in medical imaging: Opportunities and challenges." In: *2020 IEEE 17th International Symposium on Biomedical Imaging (ISBI)*. IEEE. 2020, pp. 337–340.

[139] Li Sze Chow and Heshalini Rajagopal. "Modified-BRISQUE as no reference image quality assessment for structural MR images." In: *Magnetic resonance imaging* 43 (2017), pp. 74–87.

[140] Sheeba J Sujit, Refaat E Gabr, Ivan Coronado, Melvin Robinson, Sushmita Datta, and Ponnada A Narayana. "Automated image quality evaluation of structural brain magnetic resonance images using deep convolutional neural networks." In: *2018 9th Cairo International Biomedical Engineering Conference (CIBEC)*. IEEE. 2018, pp. 33–36.

[141] Oscar Esteban, Daniel Birman, Marie Schaer, Oluwasanmi O Koyejo, Russell A Poldrack, and Krzysztof J Gorgolewski. "MRIQC: Advancing the automatic prediction of image quality in MRI from unseen sites." In: *PloS one* 12.9 (2017), e0184661.

[142] Thomas Küstner, Annika Liebgott, Lukas Mauch, Petros Martirosian, Fabian Bamberg, Konstantin Nikolaou, Bin Yang, Fritz Schick, and Sergios Gatidis. "Automated reference-free detection of motion artifacts in magnetic resonance images." In: *Magnetic Resonance Materials in Physics, Biology and Medicine* 31.2 (2018), pp. 243–256.

[143] Thomas Küstner, Sergios Gatidis, Annika Liebgott, Martin Schwartz, Lukas Mauch, Petros Martirosian, Holger Schmidt, Nina F Schwenzer, Konstantin Nikolaou, Fabian Bamberg, et al. "A machine-learning framework for automatic reference-free quality assessment in MRI." In: *Magnetic Resonance Imaging* 53 (2018), pp. 134–147.

[144] Irene Fantini, Leticia Rittner, Clarissa Yasuda, and Roberto Lotufo. "Automatic detection of motion artifacts on MRI using Deep CNN." In: *2018 International Workshop on Pattern Recognition in Neuroimaging (PRNI)*. IEEE. 2018, pp. 1–4.

[145] Irene Fantini, Clarissa Yasuda, Mariana Bento, Leticia Rittner, Fernando Cendes, and Roberto Lotufo. "Automatic MR image quality evaluation using a Deep CNN: A reference-free method to rate motion artifacts in neuroimaging." In: *Computerized Medical Imaging and Graphics* 90 (2021), p. 101897.

[146] Lea L Backhausen, Megan M Herting, Judith Buse, Veit Roessner, Michael N Smolka, and Nora C Vetter. "Quality control of structural MRI images applied using FreeSurfer—a hands-on workflow to rate motion artifacts." In: *Frontiers in neuroscience* 10 (2016), p. 558.

[147] Aurélien Géron. *Hands-on machine learning with Scikit-Learn, Keras, and TensorFlow: Concepts, tools, and techniques to build intelligent systems*. " O'Reilly Media, Inc.", 2019.

[148] Tarek Amr. *Hands-On Machine Learning with scikit-learn and Scientific Python Toolkits: A practical guide to implementing supervised and unsupervised machine learning algorithms in Python*. Packt Publishing Ltd, 2020.

[149] Waseem Rawat and Zenghui Wang. "Deep convolutional neural networks for image classification: A comprehensive review." In: *Neural computation* 29.9 (2017), pp. 2352–2449.

[150] Yinglong Li. "Research and Application of Deep Learning in Image Recognition." In: *2022 IEEE 2nd International Conference on Power, Electronics and Computer Applications (ICPECA)*. IEEE. 2022, pp. 994–999.

[151] Victor E Staartjes and Julius M Kernbach. "Foundations of Machine Learning-Based Clinical Prediction Modeling: Part V—A Practical Approach to Regression Problems." In: *Machine Learning in Clinical Neuroscience*. Springer, 2022, pp. 43–50.

[152] Pat Langley et al. "The changing science of machine learning." In: *Machine learning* 82.3 (2011), pp. 275–279.

[153] Zhou Wang, Alan C Bovik, Hamid R Sheikh, and Eero P Simoncelli. "Image quality assessment: from error visibility to structural similarity." In: *IEEE transactions on image processing* 13.4 (2004), pp. 600–612.

[154] Richard Shaw, Carole Sudre, Sebastien Ourselin, and M Jorge Cardoso. "MRI k-space motion artefact augmentation: model robustness and task-specific uncertainty." In: *International Conference on Medical Imaging with Deep Learning–Full Paper Track*. 2018.

[155] Fernando Pérez-García, Rachel Sparks, and Sebastien Ourselin. "TorchIO: a Python library for efficient loading, preprocessing, augmentation and patch-based sampling of medical images in deep learning." In: *Computer Methods and Programs in Biomedicine* 208 (2021), p. 106236.

[156] Ajantha S Atukorale and Tom Downs. "Using labeled and unlabeled data for training." In: (2001).

[157] Kaiming He, Xiangyu Zhang, Shaoqing Ren, and Jian Sun. "Deep Residual Learning for Image Recognition." In: *2016 IEEE Conference on Computer Vision and Pattern Recognition (CVPR)*. 2016, pp. 770–778. DOI: 10.1109/CVPR.2016.90.

[158] Sepp Hochreiter. "Untersuchungen zu dynamischen neuronalen Netzen." In: *Diploma, Technische Universität München* 91.1 (1991).

[159] Sepp Hochreiter. "The vanishing gradient problem during learning recurrent neural nets and problem solutions." In: *International Journal of Uncertainty, Fuzziness and Knowledge-Based Systems* 6.02 (1998), pp. 107–116.

[160] Hong Hui Tan and King Hann Lim. "Vanishing gradient mitigation with deep learning neural network optimization." In: *2019 7th international conference on smart computing & communications (ICSCC)*. IEEE. 2019, pp. 1–4.

[161] Kaiming He, Xiangyu Zhang, Shaoqing Ren, and Jian Sun. "Identity mappings in deep residual networks." In: *Computer Vision–ECCV 2016: 14th European Conference, Amsterdam, The Netherlands, October 11–14, 2016, Proceedings, Part IV 14*. Springer. 2016, pp. 630–645.

[162] Sepp Hochreiter and Jürgen Schmidhuber. "LSTM can solve hard long time lag problems." In: *Advances in neural information processing systems* 9 (1996).

[163] Karim Armanious, Sergios Gatidis, Konstantin Nikolaou, Bin Yang, and Thomas Kustner. "Retrospective correction of rigid and non-rigid mr motion artifacts using gans." In: *2019 IEEE 16th International Symposium on Biomedical Imaging (ISBI 2019)*. IEEE. 2019, pp. 1550–1554.

[164] Kamlesh Pawar, Zhaolin Chen, N Jon Shah, and Gary F Egan. "Suppressing motion artefacts in MRI using an Inception-ResNet network with motion simulation augmentation." In: *NMR in Biomedicine* 35.4 (2022), e4225.

[165] Karim Armanious, Chenming Jiang, Marc Fischer, Thomas Küstner, Tobias Hepp, Konstantin Nikolaou, Sergios Gatidis, and Bin Yang. "MedGAN: Medical image translation using GANs." In: *Computerized medical imaging and graphics* 79 (2020), p. 101684.

[166] Olaf Ronneberger, Philipp Fischer, and Thomas Brox. "U-net: Convolutional networks for biomedical image segmentation." In: *Medical Image Computing and Computer-Assisted Intervention–MICCAI 2015: 18th International Conference, Munich, Germany, October 5-9, 2015, Proceedings, Part III 18*. Springer. 2015, pp. 234–241.

[167] Hongpyo Lee, Kanghyun Ryu, Yoonho Nam, Jaeho Lee, and Dong-Hyun Kim. "Reduction of respiratory motion artifact in c-spine imaging using deep learning: Is substitution of navigator possible." In: *Proceedings of the ISMRM Scientific Meeting & Exhibition, Paris*. Vol. 2660. 2018.

[168] Daiki Tamada, Marie-Luise Kromrey, Hiroshi Onishi, and Utaroh Motosugi. "Method for motion artifact reduction using a convolutional neural network for dynamic contrast enhanced MRI of the liver." In: *arXiv preprint arXiv:1807.06956* (2018).

[169] M-L Kromrey, D Tamada, H Johno, S Funayama, N Nagata, S Ichikawa, J-P Kühn, H Onishi, and U Motosugi. "Reduction of respiratory motion artifacts in gadoxetate-enhanced MR with a deep learning–based filter using convolutional neural network." In: *European radiology* 30 (2020), pp. 5923–5932.

[170] Kamlesh Pawar, Zhaolin Chen, N Jon Shah, and Gary F Egan. "Motion correction in MRI using deep convolutional neural network." In: *Proceedings of the ISMRM Scientific Meeting & Exhibition, Paris*. Vol. 1174. 2018.

[171] Kamlesh Pawar, Zhaolin Chen, N Jon Shah, and Gary F Egan. "MoCoNet: Motion correction in 3D MPRAGE images using a convolutional neural network approach." In: *arXiv preprint arXiv:1807.10831* (2018).

[172] Karsten Sommer, Tom Brosch, Rafael Wiemker, Tim Harder, Axel Saalbach, Christopher S Hall, and Jalal B Andre. "Correction of motion artifacts using a multi-resolution fully convolutional neural network." In: *Proceedings of the 26th Annual Meeting of ISMRM, Paris, France Abstract*. Vol. 1175. 2018.

[173] Ben A Duffy, Lu Zhao, Arthur Toga, and Hosung Kim. "Deep learning based motion artifact correction improves the quality of cortical reconstructions." In: *ISMRM Scientific Meeting & Exhibition*. Vol. 4426. 2019.

[174] Ben A Duffy, Wenlu Zhang, Haoteng Tang, Lu Zhao, Meng Law, Arthur W Toga, and Hosung Kim. "Retrospective correction of motion artifact affected structural MRI images using deep learning of simulated motion." In: *Medical Imaging with Deep Learning*. 2018.

[175] Muhammad Usman, Siddique Latif, Muhammad Asim, Byoung-Dai Lee, and Junaid Qadir. "Retrospective motion correction in multishot MRI using generative adversarial network." In: *Scientific reports* 10.1 (2020), p. 4786.

[176] Quan Dou, Xue Feng, Zhixing Wang, Daniel Weller, and Craig Meyer. "Deep learning motion compensation for Cartesian and spiral trajectories." In: *ISMRM Scientific Meeting & Exhibition*. Vol. 4447. 2019.

[177] Chengyan Wang, Yucheng Liang, Yuan Wu, Siwei Zhao, and Yiping P Du. "Correction of out-of-FOV motion artifacts using convolutional neural network." In: *Magnetic Resonance Imaging* 71 (2020), pp. 93–102.

[178] Mark Bydder, Vahid K Ghodrati, Fadil A Ali, and Peng Hu. "Deep CNN for outlier detection: a complementary tool to low-rank based methods for reducing motion artefacts." In: *ISMRM Scientific Meeting & Exhibition*. Vol. 934. 2019.

[179] Richard Shaw, Carole Sudre, Sebastien Ourselin, and M. Jorge Cardoso. "MRI k-Space Motion Artefact Augmentation: Model Robustness and Task-Specific Uncertainty." In: *Proceedings of The 2nd International Conference on Medical Imaging with Deep Learning*. Ed. by M. Jorge Cardoso, Aasa Feragen, Ben Glocker, Ender Konukoglu, Ipek Oguz, Gozde Unal, and Tom Vercauteren. Vol. 102. Proceedings of Machine Learning Research. PMLR, 2019, pp. 427–436. URL: https://proceedings.mlr.press/v102/shaw19a.html.

[180] Alessandro Sciarra, Hendrik Mattern, Renat Yakupov, Soumick Chatterjee, Daniel Stucht, Steffen Oeltze-Jafra, Frank Godenschweger, and Oliver Speck. "Quantitative evaluation of prospective motion correction in healthy subjects at 7T MRI." In: *Magnetic resonance in medicine* 87.2 (2022), pp. 646–657.

[181] Daniel Stucht, K Appu Danishad, Peter Schulze, Frank Godenschweger, Maxim Zaitsev, and Oliver Speck. "Highest resolution in vivo human brain MRI using prospective motion correction." In: *PloS one* 10.7 (2015), e0133921.

[182] Henry B Mann and Donald R Whitney. "On a test of whether one of two random variables is stochastically larger than the other." In: *The annals of mathematical statistics* (1947), pp. 50–60.

[183] Raphael Vallat. “Pingouin: statistics in Python.” In: *The Journal of Open Source Software* 3.31 (Nov. 2018), p. 1026.

[184] John J Bartko. “The intraclass correlation coefficient as a measure of reliability.” In: *Psychological reports* 19.1 (1966), pp. 3–11.

[185] Patrick E Shrout and Joseph L Fleiss. “Intraclass correlations: uses in assessing rater reliability.” In: *Psychological bulletin* 86.2 (1979), p. 420.

[186] Nicolas A. Pannetier, Theano Stavrinos, Peter Ng, Michael Herbst, Maxim Zaitsev, Karl Young, Gerald Matson, and Norbert Schuff. “Quantitative framework for prospective motion correction evaluation.” In: *Magnetic Resonance in Medicine* 75.2 (2016), pp. 810–816. ISSN: 1522-2594. DOI: 10.1002/mrm.25580. URL: http://dx.doi.org/10.1002/mrm.25580.

[187] Kiaran P. McGee, Armando Manduca, Joel P. Felmlee, Stephen J. Riederer, and Richard L. Ehman. “Image metric-based correction (Autocorrection) of motion effects: Analysis of image metrics.” In: *Journal of Magnetic Resonance Imaging* 11.2 (2000), pp. 174–181. DOI: 10.1002/(SICI)1522-2586(200002)11:2<174::AID-JMRI15>3.0.CO;2-3. eprint: https://onlinelibrary.wiley.com/doi/pdf/10.1002/%28SICI%291522-2586%28200002%2911%3A2%3C174%3A%3AAID-JMRI15%3E3.0.CO%3B2-3. URL: https://onlinelibrary.wiley.com/doi/abs/10.1002/%28SICI%291522-2586%28200002%2911%3A2%3C174%3A%3AAID-JMRI15%3E3.0.CO%3B2-3.

[188] Jeffrey P. Woodard and Monica P. Carley-Spencer. “No-Reference image quality metrics for structural MRI.” In: *Neuroinformatics* 4.3 (2006), pp. 243–262. ISSN: 1559-0089. URL: https://doi.org/10.1385/NI:4:3:243.

[189] Pierre-Louis Bazin, Hannah E. Nijsse, Wietske van der Zwaag, Daniel Gallichan, Anneke Alkemade, Frans M. Vos, Birte U. Forstmann, and Matthan W.A. Caan. “Sharpness in motion corrected quantitative imaging at 7T.” In: *NeuroImage* 222 (2020), p. 117227. ISSN: 1053-8119. DOI: https://doi.org/10.1016/j.neuroimage.2020.117227. URL: https://www.sciencedirect.com/science/article/pii/S1053811920307138.

[190] Hendrik Mattern, Alessandro Sciarra, Falk Lüsebrink, Julio Acosta-Cabronero, and Oliver Speck. “Prospective motion correction improves high-resolution quantitative susceptibility mapping at 7T.” In: *Magnetic Resonance in Medicine* 81.3 (2019), pp. 1605–1619. DOI: 10.1002/mrm.27509. eprint: https://onlinelibrary.wiley.com/doi/pdf/10.1002/mrm.27509. URL: https://onlinelibrary.wiley.com/doi/abs/10.1002/mrm.27509.

[191] Zuzana Krbcova and Jaromir Kukal. “Relationship between entropy and SNR changes in image enhancement.” In: *EURASIP Journal on Image and Video Processing* 2017.1 (2017), p. 83.

[192] Adam Paszke et al. “PyTorch: An Imperative Style, High-Performance Deep Learning Library.” In: *Advances in Neural Information Processing Systems 32*. Curran Associates, Inc., 2019, pp. 8024–8035. URL: http://papers.neurips.

cc/paper/9015-pytorch-an-imperative-style-high-performance-deep-learning-library.pdf.

[193] Wilfried Kubinger, Markus Vincze, and Minu Ayromlou. "The role of gamma correction in colour image processing." In: *9th European Signal Processing Conference (EUSIPCO 1998)*. IEEE. 1998, pp. 1–4.

[194] R Jain, R Kasturi, and BG Schunck. "Machine Vision McGRAW-HILL International Editions." In: *New York* (1995).

[195] Gustav J Braun and Mark D Fairchild. "Image lightness rescaling using sigmoidal contrast enhancement functions." In: *Journal of Electronic Imaging* 8.4 (1999), pp. 380–393.

[196] Stephen M Pizer, E Philip Amburn, John D Austin, Robert Cromartie, Ari Geselowitz, Trey Greer, Bart ter Haar Romeny, John B Zimmerman, and Karel Zuiderveld. "Adaptive histogram equalization and its variations." In: *Computer vision, graphics, and image processing* 39.3 (1987), pp. 355–368.

[197] David M Allen. "Mean square error of prediction as a criterion for selecting variables." In: *Technometrics* 13.3 (1971), pp. 469–475.

[198] Diederik P Kingma and Jimmy Ba. "Adam: A method for stochastic optimization." In: *arXiv preprint arXiv:1412.6980* (2014).

[199] Vincent A Magnotta, Lee Friedman, and FIRST BIRN. "Measurement of signal-to-noise and contrast-to-noise in the fBIRN multicenter imaging study." In: *Journal of digital imaging* 19 (2006), pp. 140–147.

[200] Marco Ganzetti, Nicole Wenderoth, and Dante Mantini. "Intensity inhomogeneity correction of structural MR images: a data-driven approach to define input algorithm parameters." In: *Frontiers in neuroinformatics* 10 (2016), p. 10.

[201] David Atkinson, Derek LG Hill, Peter NR Stoyle, Paul E Summers, and Steven F. Keevil. "Automatic correction of motion artifacts in magnetic resonance images using an entropy focus criterion." In: *IEEE Transactions on Medical imaging* 16.6 (1997), pp. 903–910.

[202] Pauli Virtanen et al. "SciPy 1.0: Fundamental Algorithms for Scientific Computing in Python." In: *Nature Methods* 17 (2020), pp. 261–272. DOI: 10.1038/s41592-019-0686-2.

[203] F. Pedregosa et al. "Scikit-learn: Machine Learning in Python." In: *Journal of Machine Learning Research* 12 (2011), pp. 2825–2830.

[204] Michael Herbst, Julian Maclaren, Cris Lovell-Smith, Rebecca Sostheim, Karl Egger, Andreas Harloff, Jan Korvink, Juergen Hennig, and Maxim Zaitsev. "Reproduction of motion artifacts for performance analysis of prospective motion correction in MRI." In: *Magnetic Resonance in Medicine* 71.1 (2014), pp. 182–190.

[205] Benjamin Zahneisen, Brian Keating, Aditya Singh, Michael Herbst, and Thomas Ernst. “Reverse retrospective motion correction.” In: *Magnetic resonance in medicine* 75.6 (2016), pp. 2341–2349.

[206] Yudong Liang, Jinjun Wang, Sanping Zhou, Yihong Gong, and Nanning Zheng. “Incorporating image priors with deep convolutional neural networks for image super-resolution.” In: *Neurocomputing* 194 (2016), pp. 340–347.

[207] Roberto Souza, Youssef Beauferris, Wallace Loos, Robert Marc Lebel, and Richard Frayne. “Enhanced deep-learning-based magnetic resonance image reconstruction by leveraging prior subject-specific brain imaging: Proof-of-concept using a cohort of presumed normal subjects.” In: *IEEE Journal of Selected Topics in Signal Processing* 14.6 (2020), pp. 1126–1136.

[208] Soumick Chatterjee, Mario Breitkopf, Chompunuch Sarasaen, Hadya Yassin, Georg Rose, Andreas Nürnberger, and Oliver Speck. “Reconresnet: Regularised residual learning for mr image reconstruction of undersampled cartesian and radial data.” In: *Computers in biology and medicine* 143 (2022), p. 105321.

[209] Julian Maclaren, Murat Aksoy, Melvyn Ooi, and Roland Bammer. *Optical motion tracking to improve image quality in MRI of the brain*. Vol. 8500. Oct. 2012, pp. 02–. DOI: 10.1117/12.953612.

[210] Michael Herbst, Benjamin Zahneisen, Benjamin Knowles, Maxim Zaitsev, and Thomas Ernst. “Prospective motion correction of segmented diffusion weighted EPI.” eng. In: *Magnetic resonance in medicine* 74 (6 2015), pp. 1675–81.

[211] Veronika Spieker, Hannah Eichhorn, Kerstin Hammernik, Daniel Rueckert, Christine Preibisch, Dimitrios C Karampinos, and Julia A Schnabel. “Deep Learning for Retrospective Motion Correction in MRI: A Comprehensive Review.” In: *arXiv preprint arXiv:2305.06739* (2023).

DECLARATION OF HONOUR

"I hereby declare that I prepared this thesis without impermissible help of third parties and that none other than the indicated tools have been used; all sources of information are clearly marked, including my own publications.
In particular I have not consciously:

- Fabricated data or rejected undesired results
- Misused statistical methods with the aim of drawing other conclusions than those warranted by the available data
- Plagiarised external data or publications
- Presented the results of other researchers in a distorted way

I am aware that violations of copyright may lead to injunction and damage claims of the author and also to prosecution by the law enforcement authorities.
I hereby agree that the thesis may be reviewed for plagiarism by mean of electronic data processing.
This work has not yet been submitted as a doctoral thesis in the same or a similar form in Germany or in any other country. It has not yet been published as a whole."

Arrone (Italy), 2024